Marcin Nowak

Development of numerical model for modeling artificial heart valves for performing virtual therapies

PhD thesis

Supervisor:
Wojciech Adamczyk, PhD, DSc, Assoc. Prof.
Co-supervisor:
Eduardo Divo, PhD, Prof.

Silesian University of Technology

Gliwice, 2022

Author
Marcin Nowak
Silesian University of Technology
Faculty of Energy and Environmental Engineering
Department of Thermal Technology
ul. Konarskiego 22
44-100 Gliwice
Poland
e-mail: marcin.nowak@polsl.pl; marcin9.nowak3@gmail.com

System LaTeX2$_\varepsilon$

Table of Contents

Acknowledgements

I express my sincere gratitude to the supervisor of the Thesis, Professor Wojciech Adamczyk from the Department of Thermal Technology at Silesian University of Technology, for his invaluable guidance, support, patience, encouragment and realizing the ideas. Special thanks also go to my second supervisor, prof. Eduardo Divo from the Mechanical Engineering Department at Embry-Riddle Aeronautical University, Orlando, Florida.

I would like to thank the research team, special thanks go to Prof. Ryszard Białecki, Prof. Wojciech Adamczyk, MSc Agata Widuch, Dr Bartłomiej Melka, Dr Maria Gracka. I express my gratitude to Dr Marek Rojczyk for the cooperation and work during the laboratory test rig setup and measurement. Sincere thanks to my colleagues and co-workers from my Department for the collaboration during my Ph.D. journey.

Special gratitude go to my Parents for their support, patience and understanding.

Marcin Nowak

The research was supported by 2017/27/B/ST8/01046 and 2018/31/B/ST8/02201 research funds from *National Science Centre* (Poland), the research was also supported by the Silesian University of Technology within 08/060/RGJ18/0154 fund. Research was supported by the National Centre for Research and Development under contract POIR.01.01.01-00-1253/19-00.

Acronyms and Symbols

Medical acronyms and abbreviations

BMHV	Bileaflet Mechanical Heart Valve
CoA	Coarctation of Aorta
CT	Computed Tomography
CVD	Cardiovascular Disease
GOA	Geometric Orifice Area
MRI	Magnetic Resonance Imaging
NPT	Negative Pressure Transient
RBCs	Red Blood Cells
STJ	Sinotubular Junction
TPG	Transvalvular Pressure Gradient
WHO	World Health Organization

Acronyms and abbreviations

AI	Artificial Intelligence
BC	Boundary Condition
CFD	Computational Fluid Dynamics
CAD	Computer Aided Design
CURVIB-FSI	Curvilinear Immersed-Boundary FSI
DEM	Discrete Element Method
DNS	Direct Numerical Simulation
EOA	Effective Orifice Area
FEM	Finite Element Method
FSI	Fluid-Structure Interaction
FVM	Finite Volume Method
IBM	Immerse Boundary Method
LBM	Lattice Boltzmann Method
LPM	Lumped Parameter Model
max	maximum

min	minimum
ML	Machine Learning
NCV	Negative Cell Volume
NPT	Negative Pressure Transient
ODE	Ordinary Differential Equation
OpenCV	Open Source Computer Vision
UDF	User-Defined Function
P	Pressure
PIV	Particle Image Velocimetry
RANS	Reynolds-averaged Navier–Stokes
RMS	Root Mean Square
STL	triangulated surface format
THR	Threshold
TKE	Turbulent Kinetic Energy
WSS	Wall Shear Stress
2D	Two-Dimensional
3D	Three-Dimensional
6DOF	Six Degrees of Freedom

Roman letters

a	acceleration, m/s^2
A	surface, m^2
C	compliance (Windkessel model constant), $m^4 \cdot s^2 \cdot kg^{-1}$
$C_{1\varepsilon}$, C_2, η	k-ε equations model constant
d	diameter, m
d_e	equivalent diameter, characteristic dimension, m
D_ω	cross-difusion term
E	Young modulus, Pa
F	force, N
G_b	buoyancy TKE generation
G_k	mean velocity gradients TKE generation

h	Runge-Kutta stepsize
I	momentum of inertia, $\mathrm{kg} \cdot \mathrm{m}^2$
$\mathbf{k}$	vector normal to cell face
k, ε, ω	turbulence models constants
$\mathbf{L}$	momentum of momentum, $\mathrm{kg} \cdot \mathrm{m}^2/\mathrm{s}$
Δl	strain, m
m	mass, kg
M	force momentum, $\mathrm{N} \cdot \mathrm{m}$
u	velocity, m/s
$\mathrm{P_k}$	production of TKE
P_ω	production of the specific dissipation rate
Re	Reynolds number, $-$
R_1	proximal resistance (Windkessel model constant), $\mathrm{kg} \cdot \mathrm{m}^{-4} \cdot \mathrm{s}^{-1}$
R_2	peripheral resistance (Windkessel model constant), $\mathrm{kg} \cdot \mathrm{m}^{-4} \cdot \mathrm{s}^{-1}$
$\mathrm{Y_k}$	TKE dissipation rate
Y_ω	dissipation rate of specific dissipation rate
Q	volumetric flow rate, m^3/s
V	body volume, m^3
$\mathbf{y}$	mesh displacement, m

Greek letters

$\dot{\gamma}$	shear rate, $1/\mathrm{s}$
$\Delta\tau$	time step size, s
ε	relative strain, m/m
η	dynamic viscosity, $\mathrm{Pa} \cdot \mathrm{s}$
θ	pitch angle, radians
λ	Lame's first parameter, $\mathrm{N}/\mathrm{m}^2 = \mathrm{Pa}$
ν	Poisson's ratio, $-$
μ_t	turbulent viscosity
ρ	density, kg/m^3
σ	stress, $\mathrm{N}/\mathrm{m}^2 = \mathrm{Pa}$

σ_k, σ_ε	turbulent Prandtl numbers
τ	shear stress, $N/m^2 = Pa$
τ	time, s
ϕ	roll angle, radians
ψ	yaw angle, radians
ω	angular velocity, radians/s

Chapter 1

Introduction

Aortic valve stenosis is one of the most common cardiovascular diseases (CVD). Nowadays, CVD is the leading cause of death in the modern world [1, 2]. According to the World Health Organization (WHO), CVD was responsible for 31% deaths in 2015, and in Europe 45% of all diseases are the consequence of CVD [1]. Every year, CVD causes 3.9 million deaths in Europe. According to statistical data, more than 85 million people in Europe live with CVD. In general, CVD is estimated to cost the EU economy 210 billion Euro annually. Around 53% (111 billion Euro) of the total cost of CVDs in the EU are due to health care costs, 26% (54 billion Euro) to productivity losses, and 21% (45 billion Euro) to the care of people with CVD. Clearly, CVD represents a large problem to both the healthcare system and health outcomes in the population. Due to the drawbacks of the available diagnostic techniques, there is still plenty of room for new technology to enhance cardiac diagnostic capabilities. There is a great potential in the development of a hybrid approach that combines fast echocardiography with an advanced numerical model, developed in the framework of Computational Fluid Dynamics (CFD). Computational modeling is a powerful tool that allows the quantification of the severity of the disease or the simulation of therapeutic results. As a relatively new technology, cardiovascular computational modeling offers great potential for high-quality and cost-effective medical treatment.

Aortic valves diseases and prostheses design

Cardiovascular pathological changes lead to common diseases, such as atherosclerosis, aneurysm, stroke, heart attack, and valvular diseases. The last group can be divided into congenital defects, such as the biscupid aortic valve [3] or they appear as a disease with aging [4] where the aortic valve is presented in Figure 1.1. The most common valvular disease is calcified aortic valve disease, reaching 13% in the general population over 65 years; without proper treatment, 80% of patients suffer heart failure or mortality five years after diagnosis [5,6]. This disease involves an inflammatory response, lipoprotein deposition, and formation of calcific nodules, and no drug can delay or prevent progression [7]. Recent research [7] shown potential genetic pathways related to the inflammatory response, leading to the development of valvular disease. Furthermore, a particular generic mutation can be a high risk factor for heart failure [8].

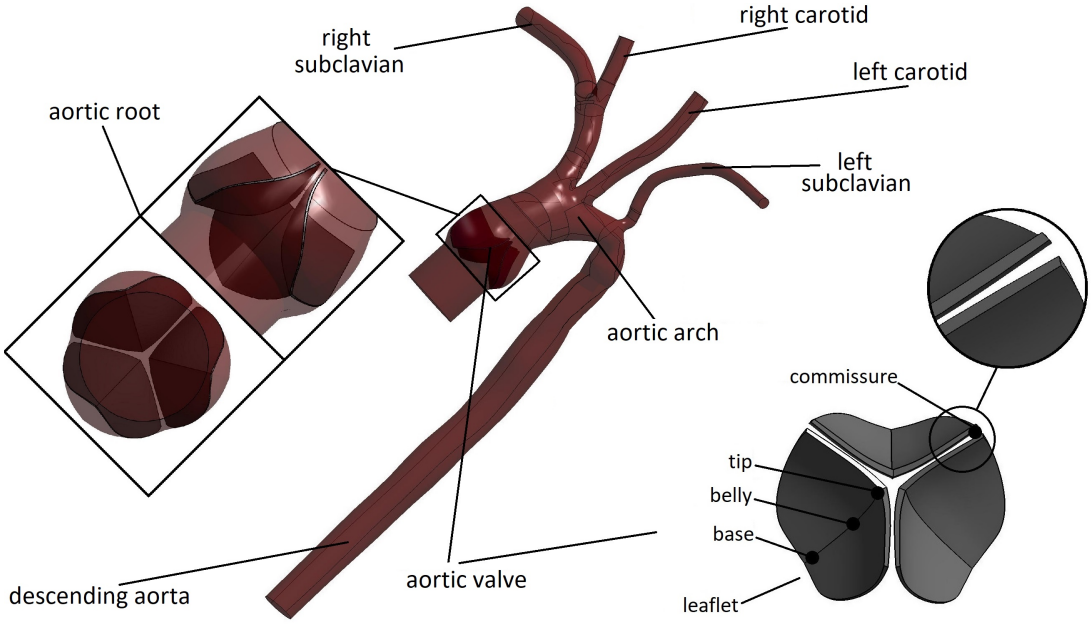

Figure 1.1: Human aortic valve, its build and location in vasculature

For patients with severe aortic valve stenosis, implantation of artificial aortic valve is the only option; however, this can lead to medical complications. Mechanical valves commonly used, increase the risk of thrombosis and require constant anticoagulation therapy, and bioprosthetic valves (artificial or animal) are prone to deterioration and

have limited durability [9]. The preferred material most often used for the manufacture of synthetic valves is pyrolytic carbon [10, 11]. The synthetic valve is represented by different configurations, such as Bileaflet Mechanical Heart Valve (BMHV), tilting disc, trileaflet, monoleaflet, and caged-ball valves, which are some of the models that are used routinely for implantation. Some of the commonly used artificial valve types are presented in Figure 1.2. Infection, paravalvular abscess, or perivalvular leakage are possible risks and complications of synthetic heart valve implantation. Mechanical valves shown in Figure 1.2A,D) carry a higher risk of thrombus (blood clot), thrombosis and stroke, and destruction of blood cells by hemolysis [12]. Thrombosis occurs when the formed thrombus obstructs blood flow, it can also break free and travel to another place in the circulatory system (i.e., embolism). which may cause further consequences, such as stroke or myocardial infarction. Anticoagulation therapy is usually prescribed to reduce the risk of these consequences; however, it can lead to bleeding complications in some patients. Research [9] describes the experience and conclusions based on ten years of valve replacement performed over two decades before. This confirmed the durability and efficiency of replacement, noting that the rate of freedom from valve-related complications was between 77.4% and 100%, depending on the group of patients. Some patients had complications from thromboembolism, anticoagulant-related hemorrhage, endocarditis, or the need for reoperation. However, despite the continued improvement in surgical and imaging techniques [13], knowledge and progress in terms of patient treatment, the development of techniques that can help limit complications remains an ongoing challenge.

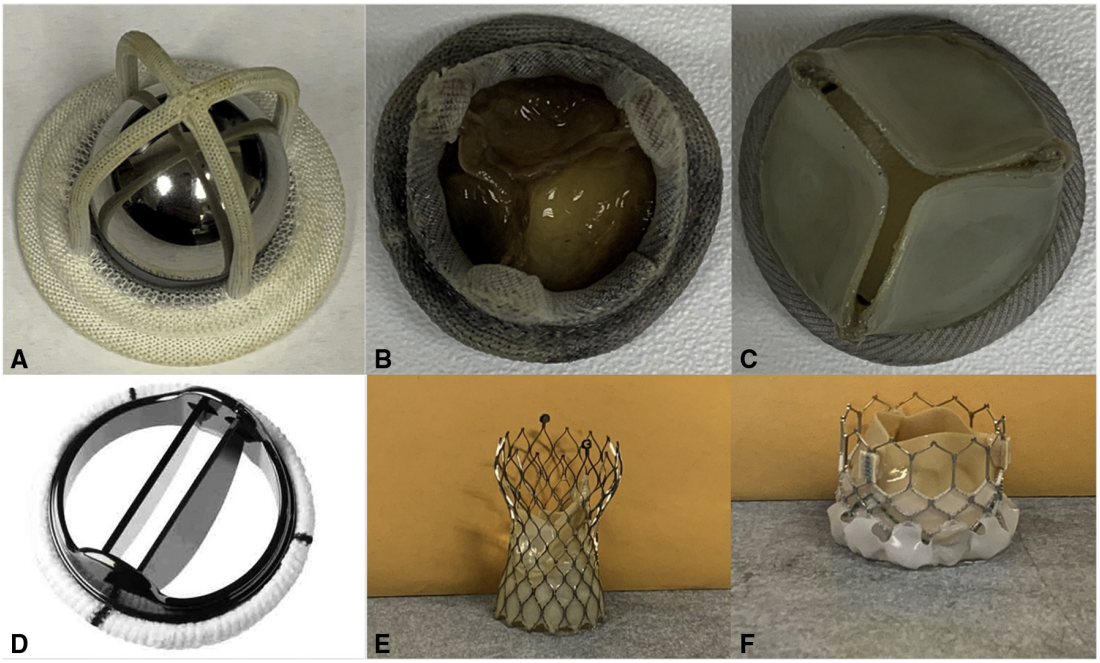

Figure 1.2: Artificial aortic valves of different types: **A** - Starr Edwards Ball and Cage, **B** - Medtronic Hancock II, **C** - St Jude Trifecta, **D** - Masters Series St Jude Mechanical Valve, **E** - Medtronic Evolut, **F** -Edwards SAPIEN 3. *Reproduced from reference [14] under the Creative Commons CC-BY-NC-ND license*

Computer modeling in cardiovascular system

CFD to model blood flow has had various applications [15, 16]. Generally, CFD models in cardiovascular applications can be classified into two main categories: cardiac and vascular. The cardiac models are much more complicated than the vascular models. They are numerically complex, mainly because of the physics that needs to be captured. Because of that, the computational time is much longer. CFD modeling can be applied in many scenarios involving human diseases and disorders, including the aortic valve. It may be used in terms of patient examination, treatment planning, finding cardiovascular zones susceptible to disease, predicting surgery results, and designing medical devices [17]. Additionally, it can support physicians in choosing the best prosthesis type for patient-specific vascular, flow, and pressure conditions.

1.1 Motivation and background

An important task in medicine and engineering is to reduce mortality and improve society life. However, achieving this goal is challenging, due to a common CVD, especially in developed countries with an aging population. Ensuring the proper treatment protocols [18] and prostheses that are used, is crucial for all patients; now it is also possible to forecast future potential pathologies in patient vascular diseases, with the use of digital CFD models and by application, for example, Artificial Intelligence (AI). However, it is important to use robust, reliable, error-proof and validated computational models in a clinician practice. The model validation can be performed with the use of the laboratory test rig measurement data and also using the patient-specific data coming from their medical examination, where in this Ph.D. thesis both pathways were utilized, where the medical data were accessed from the available literature. The method developed in the presented dissertation can be seen as an initial step toward a developing medical procedure that can make the learning curve for young cardiologist more flatten and eliminates dozens of possible complications that can occur during patient treatment.

To understand the physics of the motion and operation of the anatomical and prosthetic aortic valve a computational modeling techniques can be used. For instance, the CFD combined with Fluid-Structure Interaction (FSI) to simulate the movable elements of artificial heart valves, and also examination of different valve implantation techniques is recognized as appropriate solution. Currently, different methods are available for non-invasive diagnostics in cardiology, such as: echocardiography 3D/4D, computed tomography (CT), and cardiac magnetic resonance imaging (MRI). They are using different techniques to gain the images, such as ultrasound waves, X-rays, and magnetic field resonance, respectively. Unfortunately, each technique suffers from imperfections, which may be susceptibility to patient factors, high cost (MRI), use of contrast agents, exposure of the body to radiation (CT) [19–22]. Thus, there is still room for improvement of diagnostic procedures, for example, through the use of the hybrid approach that combines diagnostics with numerical methods, prepared in terms of CFD. Progress being made in computational hardware and software leads to

fast and cheap computations, which are important factors in the application of numerical methods to patient treatment and examination.

The candidate experience with cardiovascular system modeling started with the published article, as the result of the master thesis work: *M. Nowak el al., The protocol for using elastic wall model in modeling blood flow within human artery, European Journal of Mechanics - B/Fluids (77) 2019 [23].* In the research mentioned, the real geometry and the inflow profile of the 8-year-old female patient with moderate thoracic Coarctation of Aorta (CoA) (65% area reduction) was used. The applied numerical model allowed one to determine the blood wall transient deformations, pressure and wall shear stress fields, and also location of the vortices. Furthermore, the process of geometry preparation, based on the raw unstructured triangulated surface format (STL), was described. The geometry of the blood wall with changing thickness was created from the geometry of the fluid, using Geomagic Design X software (3D Systems Corporation) [24]. During Ph.D. studies, in addition to work related to the main Ph.D. topic, the author contributed to research: *B. Melka, M.Nowak et al., Flow in a Myocardial Bridge Region of a Coronary Artery - Experimental Rig and Numerical Model. Information Technology in Biomedicine (1186) 2020* [25]. This work considered a numerical model and its validation of the myocardial bridge, which is a congenital coronary artery condition, where the coronary artery is located under the muscle bridge. Therefore, the coronary artery is squeezed during systole. The numerical domain and its change in shape in time was based on the reconstructed patient vessel, with implemented time functions changing its shape due to squeezing. Also, as a co-author of the work: *B. Melka et al., Numerical investigation of multiphase blood flow coupled with lumped parameter model of outflow. International Journal of Numerical Methods for Heat Fluid Flow (30) 2020* [26], the multiphase character of the blood using the Euler-Euler approach was considered and analyzed in the large blood vessel. The multiphase flow in the Discrete Element Method (DEM) approach, laboratory work, and also computer vision procedures, used for the Ph.D. work purpose, can be found in the coauthored works of the thesis author [27, 28].

The goal of the Ph.D. dissertation is to gain knowledge of the current state of research in terms of anatomical and artificial valve modeling, along with the mechanisms

related to human valve calcification and artificial valve operation, and to develop and validate the numerical models which will fill the knowledge gaps. The focus is laid on the time-efficiency and stability of the models simulating the operation of the elastic and non-deformable rotary valves. The literature review shown, that further work is still demanded for modeling and validation of the aortic numerical models. Also, the effect of the calcification onto the anatomical and mechanical valve is not yet fully understood, therefore an effort was made to discover how stenosis impact the aortic valves.

As the numerical models are computationally expensive, the time-efficient model is needed to provide the software for the everyday use among medical professionals, to perform virtual patient therapies. Thus, a numerical model capable to accurately simulate blood flow along with movable and deformable parts of the artificial valves needs to be created. Here, a new model based on dynamic timestepping was developed for such a purpose. Furthermore, the developed model was validated against the experimental data collected at the in-house laboratory in vitro test rig, located at the Department of Thermal Technology. Several data sets corresponding to different flow conditions were used for validation purposes. The model of the elastic valve was prepared in terms of two-way coupling between the fluid and structural mechanics, and its operation was tested both in two-dimensional (2D) and three-dimensional (3D) coordinates.

An important question in the modeling of moving or deformable bodies is the proper application of moving numerical mesh protocols. In the thesis, several different moving mesh techniques were applied and tested, as: overset mesh [29], dynamic mesh (several smoothing models) [30], coupled overset and dynamic mesh [31, 32]. It was important to ensure proper mesh motion, both to obtain the converged and reliable model results and also to avoid solver errors, simultaneously solving the model in a reasonable time frame. As the FSI models are very error-prone, the protocols and recommendations were made, both for the rigid and elastic aortic valve, to make it possible to implement models for the clinician practice and also perform wide series of simulations.

Although artificial valves have been used for many years, there is still an open ques-

tion about reducing the risk of valve implantation, to avoid some consequences such as blood cell lysis, cavitation, high pressure drops, or valve deterioration [9]. Therefore, in this thesis a comparative analysis was also studied between healthy and calcified bileaflet valves and anatomical valves. Different scenarios of artificial valve deterioration caused by plaque deposition of arteriolosclerosis were simulated, using the FSI and Six Degrees of Freedom (6DOF) approach. Comparison of the natural calcification process of anatomical and artificial valves was made, which had not previously been investigated in the literature. In spite of this, to the analyses limited to the aortic valve itself and the region close to the valve, the author attempted to analyze the operation of the cardiovascular system in the large blood vessel of the patient, after valve implantation.

1.2 Objectives

The measurement of different variables, as pressure, velocity, shear stresses or deformations, may be invasive, expensive, or even not possible in the specific locations. Moreover, performing multivariant analysis via building prototypes or patients examination may be too cost and time inefficient. Therefore, the role of computer modeling and its validation have its potential. Solving of the Navier-Stokes [33] partial differential equations (and other, related e.g. to the turbulence, hemolysis or cavitation) using CFD software, enables the determination of the flow conditions. In order to solve numerical problem, the unambiguity conditions need to be known, i.e., geometry, physical properties, initial conditions and boundary conditions.

The geometry of the fluid or solid domain, gained by patient examination (e.g. magnetic resonance imaging [23]) or created using computer aided design software [3] is discretized, and the numerical method is applied to solve equations within the domain.

Blood, which is a mixture of plasma and blood cells, that is, red blood cells (RBC), white blood cells, and platelets, can be treated as a single non-Newtonian fluid, which means the non-linear dependence between shear stress and shear rate [34, 35]. The Carreau [36] viscosity model was implemented in the solution procedure. Therefore, the dynamic viscosity is calculated locally on the basis of the shear rate. The density

depends on the amount of each component and mostly depends on the hematocrit, i.e. the share of RBCs. In this study, the blood density was averaged to 1051 kg/m^3.

In cardiovascular modeling, when the elastic structures are considered, the solid properties, i.e. of the blood tissue, reflect how the solid body deforms as a result of the applied force. The stress-strain relationship also must be considered together with the material constants. The aorta walls, as well as aortic valve leaflets, are multi-layer structures, anisotropic, viscoelastic and also hyperelastic. Constitutive material models express the strain energy density function from the deformation tensor, and the commonly used for the aortic valve are the Ogden model [37] and Mooney-Rivlin models [38, 39]. However, employing all these characteristics greatly increases the computational time and model non-linearities. Thus, some assumptions and simplifications must be made in order to limit solving time and increase solver reliability, especially when multivariate analyzes are performed. Figure 1.3 [40, 41] presents the viscosity characteristics of the blood, as a relationship between the shear stress and the shear rate, and the stiffness of the blood tissue presented in the stress-strain graph. The Young modulus of blood tissue is on the level of 0.1 MPa to 12.5 MPa [42–44], which means that the solid body is highly elastic and deforms due to relatively small forces that act in the cardiovascular system due to the flow of blood and the movement of the human body.

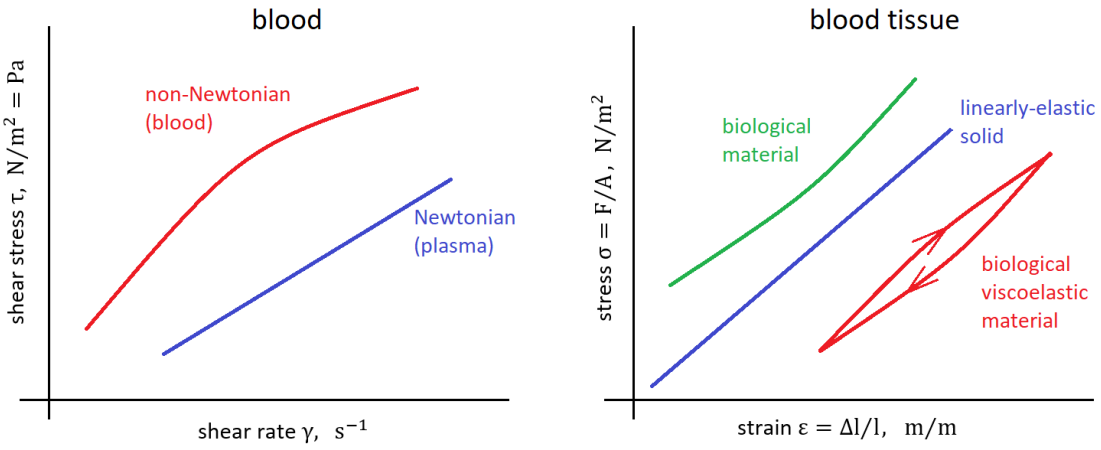

Figure 1.3: Material properties of the blood and blood tissue, for the idealized (Newtonian fluid, linearly-elastic solid) and realistic models

The initial conditions relate to initialization of the transient solution (e.g. pressure values) and the initial state in considered system, as the leaflet shape or angular position at the beginning of computation. The first aspect influence the number of solver iterations needed to achieve the proper convergence characteristics. The latter aspect may result from the registered geometry at the specific moment of heart cycle from which calculations begin, however, oftentimes solving of the several heart cycles is needed to ensure the repeatability of the results within the subsequent heart cycles.

The Boundary Conditions (BCs) refers to the values at the geometry boundaries that are known, and several types can be distinguished, based on the location and variable type. The commonly used BC for the inlet is based on the velocity time profile, where during the heart cycle the velocity changes due to the heart work. For the outlets, the pressure time profile may be imposed, or when this information is not known, the Windkessel model can be used, which use the information of the whole cardiovascular system by several Windkessel constants. On the geometry walls, the information of the wall roughness can be used for BC, however the no-slip shear boundary condition is commonly set at the fluid and solid interface. This condition causes the fluid to stick to the wall and move with the same velocity as the wall [45]. In this thesis, commercial numerical software, Ansys®, was used with necessary solver extensions, implemented by User-Defined Function (UDF) protocols. The Fluent Finite Volume Method (FVM) solver was used for the fluid problem, and Mechanical Finite Element Method (FEM) solver for the solid problem.

Fluid-Structure Interaction technique

FSI is used when the solid body interacts with the fluid and this occurs when elastic walls or for instance, the aortic valve are considered [23]. Many different approaches to model FSI are present, as the rigid body solver [30] (as implemented in this thesis for artificial valve), partitioned with two separate solvers (for fluid and solid) [46] and monolithic [47], where both the fluid and solid equations are solved in single monolithic matrix. The comparison of different FSI modeling approaches and software can be found in [48]. Furthermore, the comparison of the FVM and FEM for FSI, to the results of the computational model can be found in [49] and in [50].

The partitioned approach can be utilized as one-way or two-way coupling [51]. The first is valid when the influence of solid deformation on the flow field is negligible, so the deformations are low. Therefore, the coupling procedure is realized only once, i.e. the results from steady-fluid solver are transferred as the boundary condition to the structural solver. In the second approach, i.e. two-way coupling, the transient flexible body motion is captured, and multiple coupling procedures are performed during every timestep, till both solvers and transferred values (force and displacement) are converged. This approach was used in this investigation to model the anatomical aortic valve. In the investigation [52] the influence of considering the elasticity of the vessel on the results was compared with the rigid vessel approach. Different values of Young modulus were used, imposing several levels of deformation. The rigid wall approach overestimated the values of the wall velocity and shear stress profiles. Monolithic solvers are more stable; however, the drawbacks are the ill-conditioned problem and the long computational time [47, 53]. An example description and application of the more novel FSI methods, that is, IBM and the Lattice Boltzmann Method (LBM), can be found in [54–58].

Presented Ph.D. thesis deal with different FSI approaches. Firstly, the in-house 6DOF solver with dynamic timestepping was developed for the purpose of modeling rigid artificial valve. This model was calibrated and validated using the in-house test rig and data collected during in vitro experiments. The single FVM was sufficient to model the rigid body motion. For the elastic anatomical valve, the coupling of the commercial fluid FVM solver, Ansys® Fluent, and the mechanical FEM solver Ansys® Mechanical, was used. An additional module was applied, to exchange and transfer data between the solvers, namely the Ansys® System Coupling. Here, the numerical results were thoroughly validated against data from the literature, considering echocardiography (3D Echo), Particle Image Velocimetry (PIV), flow, and pressure measurements. The simulations carried out have shown good model reliability, in contrast to the data in the literature. For the elastic valve, the solid geometry deforms and moves the element's nodes (controlled by the solid solver) due to forces that come from the fluid solver. To improve the stability of the solution process, the idea of usage of the midside nodes [59] was introduced. This approach allows that the element edges

can form parabolic shapes, instead of the linear shapes, which increase stability and accuracy of the solver.

1.3 Current status of the research

Numerous applications of the modeling are found for the anatomical and artificial valves, e.g., for the assessment of the disease severity, investigation of the calcification process, diseases formation and prevention, and also for prostheses design. However, there is still room for improvement in the design of prostheses and also in the modeling approach itself, which could improve the applicability of modeling for medical practice and may contribute to the progress of therapeutic outcomes.

Generally, three different approaches can be distinguished in the numerical modeling of natural and artificial valves. The first approach is to model a fluid flow with stationary inflow, to reproduce the character of the flow during one specific moment of the blood cycle (e.g., during the maximum or minimum inflow) [60]. The remaining two approaches allow to reproduce a full leaflet motion mechanics and can be divided into FSI and 6DOF approaches [2, 61].

Different approaches can be found for FSI, and the choice depends on the level of fluid-solid coupling, geometry complexity, deformations, and computer resources. For example, the partitioned approach includes two separate solvers (fluid solver and mechanical solver) and a module that couples each other. Such an example usage can be found in [46], where a computational model was applied to predict the impact of the calcification process on the hemodynamics of the aortic valve, including pressure drops and flow patterns. The impact of the valve calcification process on coronary blood flow, hemodynamics, and development of coronary artery disease was investigated in [62] and [63]. Furthermore, in [62] the impact of the sinuses geometry (dilated aorta space above the aortic valve) and the location of the coronary ostia (leaflet attachment to the aortic root) was investigated. The numerical results show that the proximal type of coronary ostia location presents the highest pressure gradients during progressive calcification. A decrease in maximum speed was observed in the coronary arteries, from 1 m/s for the healthy valve to 0.45 m/s for the severely calcified case. Additionally,

the decrease in wall shear stress on the coronary artery wall caused by valve calcification has shown that it is a consequence of coronary atherosclerosis. In [64] the FEM was used to predict the spatial progression of calcification, based on the strain-based model, where high-strain leaflet regions are more prone to calcification.

Research [65] presents a semi-automated numerical modeling process that considers the aortic valve, left ventricle, and coronary ostia. 3D-TEE image sequences (Transesophageal Echocardiography) were used for automatic CAD geometry and mesh preparation. The COMSOL® Multiphysics [66] was used to solve the FSI phenomenon, using *monolithic approach*, suitable for large deformations, where the solid and fluid governing equations are solved in one matrix. The limitation was that the process was not fully automated and manual steps were required.

Research [57] investigated the impact of combined aortic and mitral valve pathology on aorta coarctation. The prepared computational framework was based on the LBM computational method and Doppler-based lumped parameter modeling. The procedure using a strongly coupled 3D FSI model for transcatheter aortic valve replacement, interacting with complex valvular, ventricular, and vascular disease, was presented in [67]. In [68] different severity of coronary artery stenosis was applied within the CFD Discrete Particle Model, to investigate its impact on spatio-temporal flow hemodynamics. In conclusion, for 50% stenosis, the disease was promoted for lower Reynolds numbers (up to 500) and suppressed for higher Reynolds numbers (500 to 800). In [69] the partitioned FSI approach was applied for the idealized multilayer coronary artery, with different levels of stenosis. The curvature radius of the stenosis was found to be more sensitive parameter affecting the hemodynamic characteristics than the detailed geometry of the stenosis. Research [70] presented a novel FSI protocol dedicated to cataract surgery. In [71], algorithm was prepared to simulate calcification, growth, valve stiffening, and aging for a person between 35 to 85 years old. Based on clinical data, the stiffness of the aortic wall increased linearly so that after 50 years its value was 2.68 times greater than the baseline. The thickening of the valve leaflets due to the calcification process was also investigated, where calcification was more likely to occur on the aortic side. Work [72] shows application of the FSI approach to investigate the impact of the highest circumferencial deformations

on baroreceptors. Research [39] used the mechanical model of the valve omitting the flow field, with the pressure boundary condition, to prepare the data set for machine learning (ML) algorithms. The ML model applied to the geometric orifice and coaptation areas of the polymeric heart valves. The structural-only approach was also used in [73], where during the 50 milions heart cycles, the change of the shape and properties of the bioprosthetic heart valve was accounted. The computational framework dedicated to the other common CVD, in addition to valvular disease, namely aortic aneurysm, is presented in [74]. The patient-specific CFD simulation along with the MRI was coupled with the finite element analysis. This was done to determine the progression of the aneurysm for four patients.

An example of fully coupled FSI usage for a mechanical valve can be found in [75], where Comsol® Multiphysics software was used with MUMPS (MUltifrontal Massively Parallel Sparse direct solver), to study the influence of hematocrit on the hemodynamics of the artificial heart valve.

In [76] the vorticity dynamics of the BMHV was studied using a numerical model involving Direct Numerical Simulation (DNS) of turbulence and leaflet motion prescribed using data from the test rig measurements. The complex flow field was described, including repeatable laminar and vorticity-like stages. The results presented highly three-dimensional flow characteristics. [77] describe the feasibility of the 4D magnetic resonance imaging method for measuring pressure drop and blood flow patterns in different types of artificial valves. This method proved to be proper for many types of valves; however, for the Medtronic CoreValve Evolut R type the results were not accurate, due to the large strut and the corresponding signal void.

The analysis of bileaflet 27 mm inner diameter valve of the bileaflet was carried out by [17], using the ALE approach and experimental measurements. The test rig was equipped with piston-in-cylinder pumps and a system that mimicked the left ventricle. The predicted closing times and transvalvular pressure drops agreed with the validation data, falling in a range of twice the standard deviation. Research [78] used the FSI-6DOF approach to analyze the kinematics of the leaflets with different aortic root geometry applied. The results revealed that flow dynamics is more dominated by the valve configuration than by the aortic root shape, cause the valve forces the

three-jets behavior and the vortex shedding. The geometry of the aortic root and the operation of the resulting bileaflet valve was also investigated by [79], where Curvilinear Immersed-Boundary FSI (CURVIB-FSI) was used along with the measurements. The results show that the leaflets in the anatomic aorta open much faster and undergo greater rebound during closing than the same valve in the straight axisymmetric aorta

When the blood flow within deformable arteries is modeled, the question arises of whether the wall can be treated as a rigid boundary or the FSI approach should be used. The assumption of rigid walls overestimates the wall shear stress (WSS), sometimes by 50%, and causes some qualitative and quantitative differences compared to the more accurate flexible wall approach [80]. In [42] a numerical analysis of blood flow was performed in a flexible abdominal real aorta. The calculated pressure in the FSI model was 15% lower compared to the rigid model. However, this is most apparent in younger patients, as the blood vessels of children are more flexible than those of adults, whose additional stiffness comes from arteriosclerosis. As valvular diseases are prevalent in older patients, the common assumption of a rigid blood wall is made, when the valve FSI is modeled.

All the mentioned approaches have one common feature, namely, the computational cost is quite large, and as was mentioned, the stability of the coupling procedure in terms of usage of the FSI approach is very problematic. Some perspective to replace lengthy computational analysis is found in the usage of machine learning tools [81]. Also, computational time and stability is considered more advantageous when the 6DOF model is used. Here, the model applicability is found in rigid structures, such as one-, two-, or three-leaflet artificial valves, where the forces exerted by the fluid are retrieved from the fluid solver and then this solver calculates the leaflets' rotational velocity, using equations including the leaflet inertial model. It is necessary to implement some approach for the moving mesh, such as a dynamic or overset mesh, to absorb the motion in a domain.

In the case of implanted artificial bileaflet aortic valve, the risk of valve calcification process is still present. The calcification process in the human vasculature is highly prevalent and increase with age, causing arterial stiffness [71, 82]. Approximately, each year 280,000 patient worldwide receive a prosthetic heart valve [83]. These cases

involve a risk of consequences such as prostheric valve endocarditis (inflammation of the inner vasculature layer in the valve region due to the foreign surface), hemolysis and thromboembolism, which can lead to the local plaque deposition in the valve region [83, 84]. The ESC/EACTS Guidelines [18] describe the criteria for assessment of the valve calcification severity, based on different characteristics, as the valve opening area or reversed flow area. Patients with a prosthetic heart valve should be seen annually by a cardiologist, undergo echocardiogram examination every 1-5 years, and prevent of the potential consequences, e.g. use an anticuagulation agent [84]. The risk of the plaque deposition and in the valve region, and valve leaflet motion restriction, is increased by number of prosthetic-related reasons, such as thrombogenicity (tendency of a material in contact with the blood to produce a thrombus), flow separation and stagnation, blood cell damage, and other factors, as atrial fibrillation and left ventricular systolic dysfunction [84]. In [85] and [86], case reports are described for 70-year-old male and 60-year-old female patients. The diagnosis of calcified implanted valve, was 16 years after implantation. Typical sympthoms of severe aortic stenosis were present and reoperation was required. Prosthetic valve thrombosis is a rather rare phenomenon, as it is present at a rate of 0.03% per patient-year [85]. However, the process of deterioration of the prosthesis valve in terms of its progressive calcification, along with changes in aortic root and coronary flow, is not well examined in the literature. A single experimental study [83], in which blood flow patterns, turbulence and pressure drop were examined in the normal and stenotic prosthetic heart valve, using 4D Flow MRI, was found for a level of calcification.

1.4 Outline of the thesis

The Ph.D. study was divided into seven chapters and three appendices containing source codes used in the Fluent journals and UDFs, as well as the Python source codes used for the image processing programs.

Introduction chapter includes information on the necessity of biomedical engineering development, in terms of the high clinical demand for computer algorithms. The diseases of the aortic valves and prostheses used for human valve replacement are

described. The basic concepts regarding computational modeling methods for fluid, structural and FSI solvers are explained. The literature review shows the current stage of knowledge in terms of computational modeling and laboratory measurement, applied for vascular CFD and FSI, especially for valve modeling. The author's experience with cardiovascular modeling and laboratory test-rig measurement was outlined.

Mathematical model describe the physics in terms of the fluid, structural, and FSI coupling equations, built-in the commercial Ansys® software. In addition, the mathematical approach for internal algorithms is described here. The solution workflow is presented graphically in the flowcharts. The material model for the non-Newtonian Carreau viscosity is presented. The applicability of the models used is described. The basic indicators on human and artificial valve performance, used in the following chapters, are described here.

Artificial valve modeling is described in Chapter 3. The artificial bileaflet valve was virtually implanted within the geometry of the real patient, containing the aortic root, the ascending and descending aorta, and the main arterial branches. The different Reynolds-averaged Navier–Stokes (RANS) turbulence models were applied to assess their validity and applicability for valve modeling. The valve motion was imposed using the measured angular profiles found in the literature. The lumped-parameter model for the outlets was applied here and the results were compared with the simpler 0 Pa gauge pressure boundary condition. The impact of limited usage of the geometry scope on the results was assessed.

Extension of the FSI approach for the mechanical valve with validation is described in Chapter 4. The laboratory test setup and equipment is presented for the validation of the models. The in-house 6DOF model is presented to be time-efficient for the rigid rotating structures. The novel approach to dynamic time-step sizing is implemented in the solution procedure, which considerably improved moving mesh operation, solver convergence, and computational efficiency. The model was validated using an in-house test rig managed by the Labview application, equipped with the pulsatile blood pump, fast camera, mass flow meter, pressure transducers, and valve holder designed for the measurements. A data set was used for the model calibration, i.e. the moment of inertia constant, and four validation datasets confirmed the excellent model validity, based on

the valve leaflet angle courses and pressure values. The in-house Open Source Computer Vision (OpenCV) algorithm was developed to process the fast camera images into leaflet angle values.

Modeling anatomical and artificial aortic valve stenosis is described in Chapter 5. The application of the novel, advanced moving mesh model, which consists of the coupling of the dynamic mesh smoothing and the overset mesh technique, to speed up the FSI computation and improve the convergence and stability was shown. Real 2D and 3D vasculature and valve geometries were created based on the echocardiography images available in the literature. The calculations of anatomical and artificial valve models were performed for the various severity of the atherosclerosis, not previously published for the mechanical valve. The impact of the calcification process on natural and artificial aortic valves was assessed and compared.

Discussion and Conclusions chapter summarizes the conclusions derived based on the research carried out and indicates the topics that researchers should consider in the future in terms of vascular CFD and measurement.

Chapter 2

Mathematical model

The complex problem of blood flow through rigid rotary or flexible structures requires the usage of complicated mathematical models. They include the solving of the physics present on the fluid and on the solid (structural) side and also their mutual interaction. The fluid equations include the partial differential Navier-Stokes equations, the mathematical description of the turbulence model, and the model for boundary conditions, such as the Windkessel model for outflows, created based on the electrical analogy. Also, the non-Newtonian viscosity model has to be implemented into the solution procedure if the blood viscosity has to be taken into account. On the solid side, the structural governing equations are applied, which allow to calculate the deformation field resulting from the forces and body constraints, i.e. the solid body shape is changing in time. If two solid bodies are moving close to each other, there is a possibility, that these bodies will intersect each other; such situation is recognized as penetration. Depending on the volume of intersection (penetration area) and the pressure and velocity fields in such area, this may or may not influence considerably onto results. Nevertheless, in the fluid solver, such situation will cause a fluid domain collapse, which can cause a solver error. To avoid a body penetration, the contact modeling can be applied [87], to model interaction between two solid bodies, and remain an offset between them, i.e. minimum allowable distance between the bodies.

In the case where the solid body does not deform but moves, i.e., rotates or transforms in space, this change in location can be calculated inside the fluid solver standalone. This limit the model complexity, as the outside structural solver is not nec-

essary. This rigid body model was implemented and described for the purpose of modeling the angular motion of valve leaflets.

The solid and fluid geometry is discretized for the purpose of its usage in the solvers. The discretized geometry form is called as *numerical mesh* and the discretization process is presented in Figure 2.1. Different mesh elements can be used for such purpose, as hexahedras, tetrahedras, polyhedras, wedges (for 3D) or quadrilaterals, triangles, polygons (for 2D). When the geometry shape changes during solving, i.e. the solid body deforms or changes its location, this change has to be taken into account both inside the solid and fluid solver. The structural solver automatically adjust the solid body numerical mesh using build-in algorithms, which change the location on mesh nodes in space. However, the fluid solver demands the proper selection and application of the *moving mesh module*, such as the *dynamic mesh, Fig. 2.1* or *overset mesh, Fig. 2.2*, which will cause the discretized fluid domain to adjust. The overset mesh method is based on the separate creation of the background and component mesh (or meshes), and then coupling them together in the solver; such process is presented in Figure 2.2. The mathematical models for fluid moving mesh and their utility description is included in this chapter.

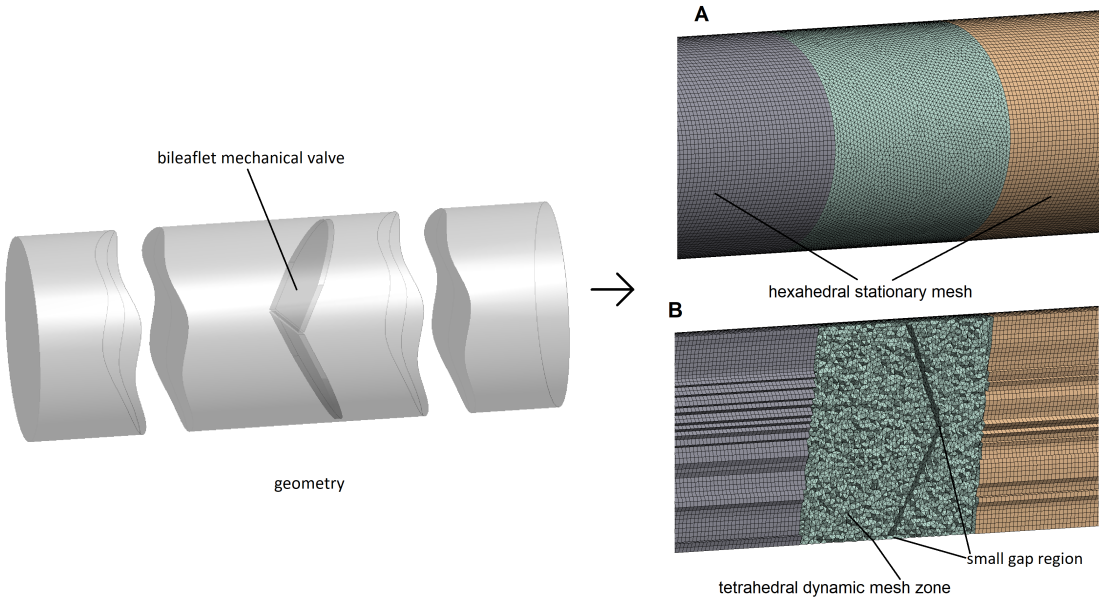

Figure 2.1: Geometry discretization presented on the example of the artificial mechanical valve, where the dynamic moving mesh module is applied: **A** - outer mesh, **B** - cross-section through domain

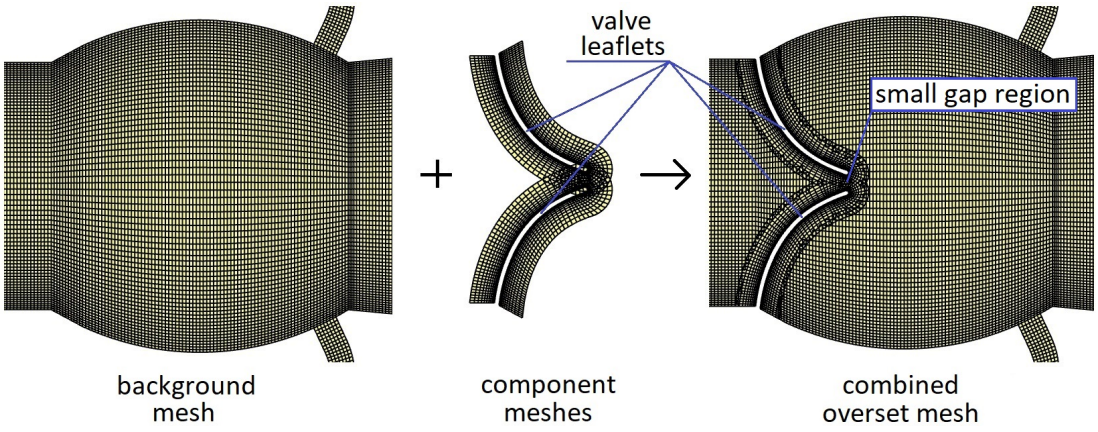

Figure 2.2: Overset mesh methodology and nomenclature, presented on the example of the elastic valve; the background and component meshes are coupled inside the solver to perform calculations

When the interaction between the solid and fluid domain is modeled, the proper FSI algorithm has to be applied. This includes the Bucket Surface and General Grid Interface algorithms [41, 59], which are used for mapping, i.e., creating pairs between the fluid and solid mesh nodes, to exchange information between them. Most importantly, the type of FSI solver has to be chosen, i.e. the monolithic (single solver) or partitioned (two separate, fluid and solid solvers). If the latter is used, the stabilization algorithms for changing the pressure and force data between the solvers has to be applied, to obtain the converged results for the highly flexible bodies.

2.1 The governing equations

The finite-volume solver (Ansys® Fluent) calculates the flow field based on solving the set of partial differential equations ((2.1), (2.2)), formed for the unsteady flow in instantaneous form, with omitted gravitation as follows

$$\frac{\partial \rho_{fl}}{\partial \tau} + \nabla \cdot \left(\rho_{fl}\mathbf{u}\right) = 0 \tag{2.1}$$

$$\frac{\partial}{\partial \tau}\left(\rho_{fl}\mathbf{u}\right) + \nabla \cdot \left(rho_{fl}\mathbf{u}\mathbf{u}\right) = -\nabla p + \nabla \cdot \left(\overline{\overline{\tau}}\right) \tag{2.2}$$

where ρ_{fl} is the density of the fluid, τ is the time and $\mathbf{u}$ is the velocity vector [33, 88]. The stress tensor $\overline{\tau}$ is defined as

$$\overline{\overline{\tau}} = \eta\left[\left(\nabla\mathbf{u} + \nabla\mathbf{u}^T\right) - \frac{2}{3}\nabla\cdot\mathbf{u}I\right] \tag{2.3}$$

where η stands for the dynamic viscosity, I is the unit tensor, and the term on the right side of the bracket is the effect of volume dilation [88]. For the incompressible fluid $\frac{\partial \rho_{fl}}{\partial \tau} = 0$ and $\frac{2}{3}\nabla\cdot\mathbf{u}I = 0$.

The governing structural equations used by the structural solver Ansys® Mechanical, to determine flexible body deformations are expressed as [89]

$$\rho_{sol}\cdot\frac{\partial^2\mathbf{u}}{\partial\tau^2} - \nabla\cdot\sigma_{\mathbf{s}} = \mathbf{F_v} \text{ in } \Omega_{\mathrm{s}}(\tau) \tag{2.4}$$

where $\Omega s(\tau)$ is the structural domain at time τ, ρ_{sol} is the solid body density, $\mathbf{u}$ stands for the displacement vector, $\mathbf{F_v}$ defines the body load in N/m^3 and σ_s is the Cauchy stress tensor, which is calculated as

$$\sigma_s = \mathbf{D}\varepsilon \text{ in } \Omega_{\mathrm{s}}(\tau) \tag{2.5}$$

where $\mathbf{D}$ is the Lagrangian elasticity tensor, ε stands for the infinitesimal strain tensor for a linear elastic isotropic material, while the equilibrium condition is given as

$$\sigma_s\mathbf{n} = \mathbf{T} \text{ in } \Gamma_{\mathrm{s}}(\tau) \tag{2.6}$$

where **n** is the outward normal vector on the surface of the wall $\Gamma_s(\tau)$, and **T** defines the surface traction vector at time τ. The linear isotropic material is defined by Lame' constants φ and G as

$$\varphi = \frac{E\nu}{(1+\nu)(1-2\nu)} \tag{2.7}$$

$$G = \frac{E}{2(1+\nu)} \tag{2.8}$$

where E and ν are the Young modulus and the Poisson ratio, respectively, of the valve leaflet material.

2.2 The moving mesh

Body movement, flexible or rigid, can be captured during transient calculations using different approaches, such as sliding mesh, dynamic mesh (smoothing, remeshing, layering) and overset mesh. For the rigid body artificial bileaflet valve, the usage of an overset-only module was sufficient, because body deformations were negligible and not modeled. Additionally, the dynamic mesh was used instead of the overset approach to compare the results and the applicability of the model. To absorb elastic valve deformations in the fluid domain, two moving mesh modules were coupled, i.e. dynamic and overset mesh. The proper choice and application of the moving mesh module is a very challenging task. Many related problems may arise. For the *dynamic mesh methods*, the mesh may become deteriorated, i.e. highly-skewed cells may appear and the mesh may become highly densified or coarsened. Also, even the Negative Cell Volume (NCV) error may appear, which means that at least one numerical mesh cell have the volume below 0 mm^3. Such an error stops the solution and demands further modification of the dynamic mesh controls on the backup point. For the *overset mesh method*, the node interpolation pairs may not be possible to create, which results in worse solver convergence or even solver error. For all the moving mesh methods, the proper time discretization, adjusted to the moving body velocities is demanded, i.e. for the single time step the body can not move or deform much, to ensure the proper solving.

Overset mesh technique

The overset mesh [90] also known as the Chimera methodology, allows one to perform calculations on the overlapping meshes: the background mesh, which is stationary, and component meshes, which can be static or moving (Figure 2.2). Originally proposed in 1981 by Atta [90] and then developed by Benek et al. ([91], [29], [92]) and Chesshire and Henshaw [93]. It facilitates the creation of appropriate body meshes for domains consisting of several bodies that differ in geometrical features, static or moving. The overset technique was used to update the geometry and mesh due to the movement of the leaflets [29, 91, 92]. The overlapping meshes are coupled inside the solver, with data interpolation done between their cells, to transfer the solution information. The overset coupling procedure consists of the subsequent operations: hole cutting, overlap minimization, and donor search. The compoenent's or background's cells lying outside the domain are cut, and *solve cells* remains, which on the interpolation process is performed. If the meshes do not match properly, *orphan cells* may appear, which means that the interpolation pairs are not created. Therefore, sufficient overlap, number of cells across the small gap, and proper cell sizing has to be provided.

Each time the leaflets rotate or deform, the overset procedure is performed again, to prepare the new donor-receptor pairs. They are assigned to realize interpolation of the flow variables λ as [59, 94]

$$\lambda(S_0) = \sum_{i=1}^{n} \frac{\psi_i \lambda(S_i)}{\sum_{i=1}^{n} \psi_j} \tag{2.9}$$

where S_0 is the receptor node, S_i is the i-th donor node. The weight of the donor decreases with distance d from the receiver node

$$\psi_i = \frac{1}{d(S_0, S_i)^p} \tag{2.10}$$

which ensures that the interpolation of the local variables are not affected by the far-field flow variable values.

However, in the case of the overset, orphan cells can be generated in the region when the background and component meshes overlap, which means that the receptor cells

cannot find the donor cell [59]. This will reduce the computational domain and may affect the computational stability and convergence and can be caused by three different reasons [59, 95]. First, the overlap between the meshes is insufficient, or the mesh resolutions are much different. Then, the number of cells across the gap is not enough, preventing proper data interpolation. The minimum allowable number is equal to 4 and in the meshes used, at least 8 cells were imposed. Finally, when movement (translation or rotation) performed in a single time step significantly exceeds the cell height; this may cause the dead cells to become solved cells before they become receptor cells.

The second aspect related to the overset mesh objection is that the calculations are non-conservative, as in the traditional approaches, because there is an interpolation process realized between the values stored in the meshes. Generally, this is not a problem when the results converge [59, 95]. During the calculations, the overall mass balance was verified, and it indicated that this approach does not produce any imbalances. The maximum time step size equal to 0.001 s was found to be sufficient to ensure overset mesh stability and convergent results, in the case of bileaflet valve model.

The cell matching priority is done to minimize the overlap between the background and component meshes. By default, it depends on the cell volume [59], so the interface could sometimes not directly follow the position of the overset boundary. Thus, the donor priority was set as boundary-distance, and both components' body priority was applied. In this way, the densified mesh was preserved in the leaflets' vicinity, which also enabled better boundary layer resolving.

Dynamic moving mesh

The dynamic mesh, applied for the elastic and rigid valve, is carried out based on the creation of a new mesh inside the fluid solver, every time the motion is observed in the fluid domain. This technique is based on two modules: remeshing and smoothing. The smoothing method moves the internal mesh nodes to absorb movement. When cell quality characteristics extend beyond the acceptable values defined, cells are remeshed locally, preparing a new tetrahedral mesh. Three different approaches for dynamic mesh were used in the Thesis for dynamic mesh: 1^{st} - remeshing+diffusion smoothing;

2^{nd} - remeshing+spring smoothing; 3^{rd} - remeshing only, where the mesh used must be without the boundary prism layer.

Coupled overset and dynamic mesh

Typically, the overset mesh is applied for the cases with rigid bodies, moving or stationary. Due to the flexible character of the natural aortic valve, this moving mesh model is not sufficient to absorb motion and perform the hole cutting process on the background mesh. Thus, an additional dynamic mesh module was applied for the elastic valve, only on the component mesh bodies. The linear elastic solid smoothing method was chosen to avoid more expensive remeshing and to maintain structural mesh in the leaflets surroundings. The described coupled moving mesh approach was used to improve stability, decrease wall clock time, and avoid mesh problems when the valve leaflets are close to each other.

For the linear elastic solid-based dynamic mesh smoothing model, where the component mesh is treated as linear-elastic with small-strain approximation, the motion of the mesh is governed by the following set of equations [31, 59]

$$\begin{aligned} \nabla\sigma(\mathbf{y}) &= 0 \\ \sigma(\mathbf{y}) &= \lambda\,(tr\varepsilon(\mathbf{y}))\,I + 2\mu\varepsilon(\mathbf{y}) \\ \varepsilon(\mathbf{y}) &= \frac{1}{2}\left(\nabla\mathbf{y} + (\nabla\mathbf{y})^{T}\right) \end{aligned} \tag{2.11}$$

where σ is the stress tensor, ε is the strain tensor, and $\mathbf{y}$ represents the displacement of the mesh. The ratio between the shear modulus ν and Lame's first parameter λ is parametrized by the Poisson ratio, set here as equal to 0.45; $\nu = 1/\left(2\left(1+\frac{\nu}{\lambda}\right)\right)$. Described equation (2.11) govern the fluid mesh, and then the fluid solver calculates the mesh velocity based on the size of the time step and the displacement of the mesh $\mathbf{y}$. Afterward, depending on the velocity of the mesh, the individual nodes move or become stationary [31]. After moving the mesh nodes of the components using the dynamic mesh module, the overset procedure is realized between the components and the background meshes.

2.3 Turbulence modeling

The flow can be determined by three states: laminar, transitional, and turbulent [88]. The dimensionless number, which characterizes the flow state, is the Reynolds number. It is the ratio of inertial to viscous forces and is defined by $\mathrm{Re} = \rho \mathrm{ud}/\eta$, where ρ is the density of the fluid, u is the velocity, d stands for the diameter and η is the dynamic viscosity. According to different sources [2,33,88], the flow could be assumed to be laminar when the Reynolds number does not exceed the maximum value from 2100 to 2300. Therefore, arterial flow is mainly laminar, except for the brief period immediately post-systole in the ascending aorta, when the instantaneous Re value falls between 4000:5000 [2,80]. The aortic root partially inhibits the turbulence effect [96]. The transition from laminar to turbulent flow could be due to increased velocity, which appears during physical exercise, aortic stenosis, or due to a prosthetic implant [61].

The **k-ε realizable** model was applied based on model transport equations for the turbulence kinetic energy (k) and its dissipation rate (ε). These variables are calculated from equations [45,97]

$$\frac{\partial}{\partial t}(\rho k) + \nabla \cdot (\rho k \mathbf{u}) = \nabla \left[\left(\mu + \frac{\mu_t}{\sigma_k} \right) \nabla k \right] + G_k + G_b - \rho \varepsilon \tag{2.12}$$

$$\frac{\partial}{\partial t}(\rho \varepsilon) + \nabla \cdot (\rho \varepsilon \mathbf{u}) = \nabla \left[\left(\mu + \frac{\mu_t}{\sigma_\varepsilon} \right) \nabla \varepsilon \right] + \rho C_1 \Omega \varepsilon - \rho C_2 \frac{\varepsilon^2}{k + \sqrt{\nu \varepsilon}} + C_{1\varepsilon} \frac{\varepsilon}{k} C_{3\varepsilon} G_b \tag{2.13}$$

where

$$C_1 = max \left[0.43, \frac{\eta}{\eta + 5} \right], \ \eta = \Omega \frac{k}{\varepsilon}, \ \Omega = \sqrt{2 \Omega_{ij} \Omega_{ij}} \tag{2.14}$$

where the vorticity tensor is calculated as:

$$\Omega_i = \frac{1}{2} \left(\frac{\partial U_i}{\partial x_j} - \frac{\partial U_j}{\partial x_i} \right) \tag{2.15}$$

where $U(x, \tau)$ is the flow velocity vector having components u_i in the x_i direction and u_j in the x_j direction. C_2, $C_{1\varepsilon}$ and η are the model constants, G_k is the generation of turbulence kinetic energy due to mean velocity gradients, G_b is the generation of

turbulence kinetic energy due to buoyancy. σ_{k} and σ_{ε} are the turbulent Prandtl numbers for k and ε, respectively, and μ_{t} is the turbulent viscosity.

The **k-ω SST** model combines the standard k-ω and k-ε turbulence models, thus it combines the good prediction of the freestream flow of the k-ε model and well behavior of the k-ω model in the near wall region of the flow. The transport equation for the model constants k and ω are [98]

$$\frac{\partial}{\partial t}(\rho k) + \nabla \cdot (\rho k \mathbf{u}) = \nabla \left[\left(\mu + \frac{\mu_t}{\sigma_k} \right) \nabla k \right] + P_k - Y_k \tag{2.16}$$

$$\frac{\partial}{\partial t}(\rho \omega) + \nabla \left[\left(\mu + \frac{\mu_t}{\sigma_\omega} \right) \nabla \omega \right] + P_\omega - Y_\omega + D_\omega \tag{2.17}$$

where $\mathrm{P_k}$ stands for production of turbulent kinetic energy and $\mathrm{Y_k}$ to dissipation rate of kinetic turbulence energy. P_ω is the production of the specific dissipation rate, y_ω stands for dissipation rates of specific dissipation rate and D_ω is additional cross-diffusion term.

2.4 Non-Newtonian viscosity model

Blood is a non-Newtonian fluid, which means the nonlinear dependence between shear stress and shear rate [34, 35]. To take into account such dependence in the blood flow modeling, the Carreau [36] model can be implemented into the solution procedure. Such a model determines the dynamic viscosity locally, as described by Eq. (2.18):

$$\eta = \eta_\infty + (\eta_0 - \eta_\infty) \cdot [1 + (\lambda \dot{\gamma})^2]^{\frac{m-1}{2}} \tag{2.18}$$

where η is the non-Newtonian local viscosity, $\dot{\gamma}$ stands for the local shear rate, η_0 and η_∞ are the shear-rate viscosities, equal respectively 0.056 Pa·s and 0.00345 Pa·s. λ=3.313 s stands for characteristic time and m is the power-law index equal to 0.3568. The shear rate in Eq. (2.18) $\dot{\gamma}$ is the gradient in streamwise velocity in the direction perpendicular to velocity.

2.5 Outflow boundary condition model

The boundary condition for the numerical model comes from the physical measurement. For the inlet and outlet this may be in the form of the velocity or pressure-time profile. However, a scenario may arise, where only the inflow profile is known. In such a situation, to model the time-varying pressure and mass flow at the outlets, the Windkessel model can be implemented into the solution procedure, which is based on the electrical analogy. This model is more realistic compared to the constant outlet pressures or loss coefficients imposed [99], because it takes into account the distensibility of the walls of the aorta and the resistance of the entire cardiac system. The 3-element model constants include two values for resistance, i.e., proximal R_1 (simulates aortic or pulmonary resistance) and distal R_2 (peripheral resistance), as well as one value for compliance C, which represents the compliance of the veins. The solution procedure determines the time-variable pressures at the outlets of the computational domain, with respect to the blood volumetric flow rate. The final forms of the ordinary differential equation (ODE) that was used are defined as

$$\frac{\mathrm{d}P(\tau)}{\mathrm{d}\tau} = \left(1 + \frac{R_1}{R_2}\right)\frac{Q(\tau)}{C} + R_1\frac{\mathrm{d}Q(\tau)}{\mathrm{d}\tau} - \frac{P(\tau)}{R_2 C} \tag{2.19}$$

where P stands for pressure, Q defines the volumetric flow rate, and τ is time. The derivation of the above equation is as follows [100]

$$\begin{gathered} I(\tau) = I_1(\tau) + I_2(\tau) \rightarrow I(\tau) = C\frac{\mathrm{d}U_{C,R_2}}{\mathrm{d}\tau} + \frac{U_{C,R_2}}{R_2} \\ U(\tau) = U_1 + U_{C,R_2} \rightarrow U_{C,R_2} = U(\tau) - I(\tau)R_1 \\ U(\tau) = P(\tau) \\ I(\tau) = Q(\tau) \end{gathered} \tag{2.20}$$

2.6 FSI-6DOF algorithm for the artificial valve

FSI modeling of the artificial bileaflet valve involves calculation of the leaflet rotations and deformations. The material constant describing body elasticity, i.e. susceptibility to deformations, is Young's modulus. Young's modulus of the valve leaflets, which are mainly created from pyrolytic carbon, is on the level of 29.4 GPa [101] and is approximately twenty thousands times higher than the modulus of elastic blood walls. Because of that, the artificial valve does not need to be simulated using any of the FSI approaches. In the presented work, the rigid body motion solver discussed in the latter section was implemented into the Ansys® Fluent solution procedure using a set of UDFs. The commercial Fluent software has already 6DOF solver available, however, its usage for the application discussed here fell short due to several reasons. First, serious problems with achieving convergence and built-in stabilization mechanisms were experienced, as changing stabilization factors and implicit updates did not help. Due to the lack of access to the source code, no further solver manipulation was possible. Second, it was not clear to us which moment of inertia should be imputed, namely if the global or local coordinates should be considered. It was also not known whether pressure and viscous forces were applied to calculate the motion. Third, there were problems with blocking motion when the leaflets achieved the maximum or minimum allowable angle. Ansys® enabled the possibility of wide customization using UDFs and it was decided to implement an in-house rigid body motion model. This allowed to get rid of any insecurities and allowed the additional manipulation, debugging, and results postprocessing. The results of the implemented model were compared with the build of the 6DOF solver, using several other simpler-to-converge cases, and no substantial differences were not observed.

In the classical rigid body motion theory, the motion of the body is decomposed into translation along three directions and rotations around three axes [30, 102]. To calculate every motion component properly, two different coordinate systems are used: the global (inertial), which is fixed, and the body (local) coordinate system, as presented in Fig.2.3. The origin of the body coordinate system is generally placed at the center of gravity of the rigid body. In the case of the mechanical valve leaflet, where only

one degree of freedom is allowed (1 rotation), the origin is in the center of the axis of rotation.

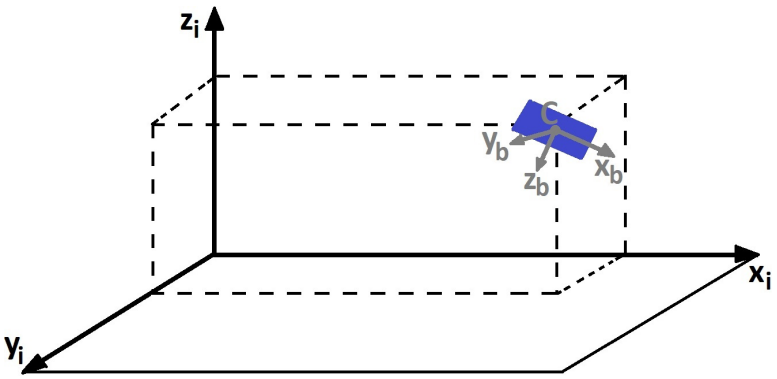

Figure 2.3: Inertial coordinate system (x_i, y_i, z_i) and the body coordinate system (x_b, y_b, z_b), presented on example of the cuboid. The point C relates to the origin of the body coordinate system, i.e. the cuboid center of gravity.

The translational motion of the rigid body's center of gravity is calculated in the global coordinate system from the Newton's second law:

$$\mathbf{a_c} = \frac{1}{m} \sum \mathbf{F_c} \tag{2.21}$$

where $\mathbf{a_c}$ is the acceleration of the center of gravity, m is the body mass, $\mathbf{F_c}$ the forces crossing the center of gravity based on the force translation theorem.
The rotational motions are calculated in the local coordinate system. The body's momentum of momentum is defined

$$\mathbf{L_B} = I \cdot \omega_B \tag{2.22}$$

where I is the inertia tensor, ω_B is the vector of angular velocity of the rigid body in the local coordinate system. The momentum theorem

$$\frac{\mathrm{d}\mathbf{L_B}}{\mathrm{d}\tau} = \mathbf{M_B} \tag{2.23}$$

is applied to the body coordinate system. Finally, the governing equation for angular

motion is as follows [30]:

$$I \cdot \frac{\mathrm{d}\vec{\omega}_B}{\mathrm{d}\tau} + \vec{\omega}_B \times (I \cdot \vec{\omega}_B) = \mathbf{M_B} \tag{2.24}$$

The transformation matrix T is used to transform the moments from the inertial coordinate to local coordinates with equation $\mathbf{M_B} = T \cdot \mathbf{M_I}$, where ϕ is the rotation about an x-axis (roll angle), θ rotation about the y-axis (pitch angle) and ψ - rotation about the z-axis (yaw angle):

$$T = \begin{pmatrix} cos\phi \cdot cos\psi & cos\phi \cdot sin\psi & -sin\theta \\ sin\phi \cdot sin\theta \cdot cos\psi - cos\theta \cdot sin\psi & sin\phi \cdot sin\theta \cdot sin\psi + cos\phi \cdot cos\psi & sin\phi \cdot cos\theta \\ cos\phi \cdot sin\theta \cdot cos\psi + sin\phi \cdot sin\psi & cos\phi \cdot sin\theta \cdot sin\psi - sin\phi \cdot cos\psi & cos\phi \cdot cos\theta \end{pmatrix}$$

For the purpose of the 6DOF model in the Fluent solver, the UDFs and Fluent journal files were used. The overall procedure is presented in Fig. 2.4. At the beginning of the computation, the flow field is initialized as well as the variables used in model. Then, the timestep size for the solver is determined. Dynamic timestep size was implemented for several reasons. It was intended to avoid the orphan cells (in case of overset) and negative cell volumes (in case of dynamic mesh), which are present when too much rotation is performed in a single timestep. This could also deteriorate the mesh quality. Furthermore, better solution accuracy is expected when the timestep is smaller than when the angular velocity is higher. Moreover, this leads simultaneously to optimize the solution time. The dynamic timestep size was achieved using UDF `define_deltat`. The value is calculated using equation:

$$\Delta\tau_n = \frac{-\left|\omega_{n-1}\right| + \sqrt{\omega_{n-1}^2 + 4 \cdot \frac{\left|M_{n-1}\right|}{I} \cdot \Delta\theta_{max}}}{2 \cdot \frac{\left|M_{n-1}\right|}{I}} \tag{2.25}$$

The derivation of the above formula is as follows: the maximum allowable increment of the angle per timestep $\Delta\theta_{max}$ is specified as the constant value. Then, a set of equations for the n-th timestep was prepared:

$$\begin{aligned} \Delta\theta_{max} &= \left|\theta_n - \theta_{n-1}\right| \\ \Delta\theta_{max} &= \left|\omega_n \cdot \Delta\tau_n\right| \\ \omega_n &= \omega_{n-1} + \frac{M_{n-1}}{I} \cdot \Delta\tau_n \end{aligned} \tag{2.26}$$

Transforming the set of equations 2.26 lead to the quadratic function of $\Delta\tau_n$:

$$\frac{M_{n-1}}{I} \cdot \Delta\tau_n^2 + |\omega_{n-1}| \cdot \Delta\tau_n - \Delta\theta_{max} = 0 \tag{2.27}$$

Solving this function gives two roots, where only one (presented in Eq.(2.25)) represents nonnegative values; thus only this root could be chosen as a solution because the time increment must represent a positive value. As two valve leaflets are present, two different values of $\Delta\tau_n$ are obtained, where the lower value is taken to adjust the time discretization of the leaflet, that is rotating faster. It was also necessary to define the maximum allowable time step size equal to 0.001 s, to avoid setting excessively large values of $\Delta\tau_n$ when the valve is stationary. The minimum timestep set as $5 \cdot 10^{-6}$ s was specified to restrict the timestep in the case if the formulas give unreasonably low values. After prescribing the timestep size to the solver, the angular motion is calculated with the recursive formula

$$\omega_n = \omega_{n-1} + \frac{M_{n-1}}{I} \cdot \Delta\tau_n \tag{2.28}$$

where M_{n-1} is the moment of force in the step $n-1$. This formula comes from the differential equation for the angular motion towards a single axis, and solving it using Euler method

$$M = I \cdot \frac{d\omega}{d\tau} \quad -> \quad d\omega = \frac{M}{I} d\tau \tag{2.29}$$

The initial condition was set as $\omega(\tau = 0) = 0$ rad/s. The adaptive time-stepping for the Euler method is applied using the derived equation Eq. (2.25).

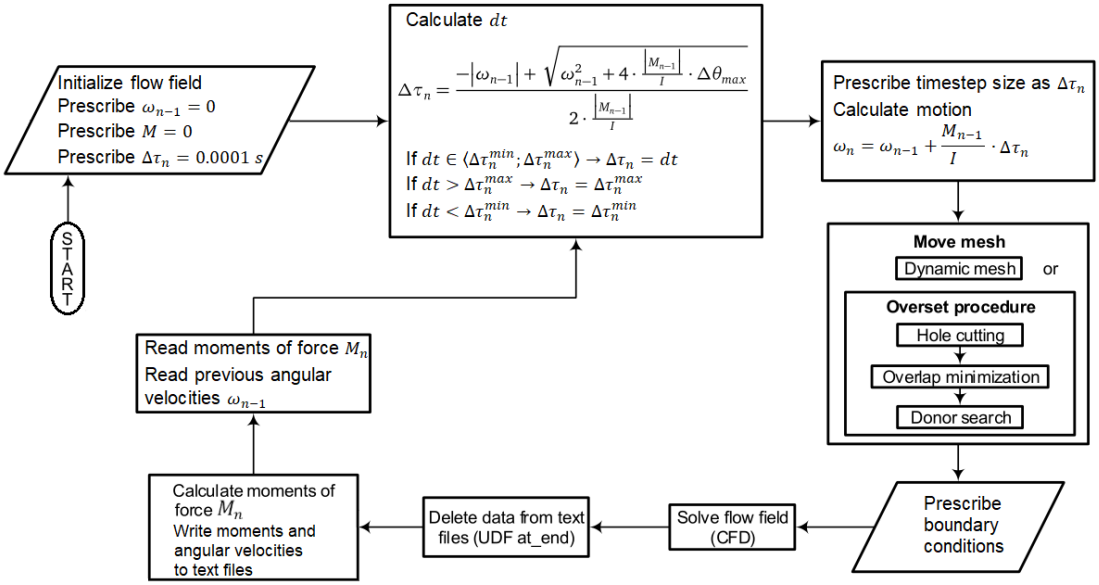

Figure 2.4: Flowchart of the 6DOF model with adaptive timestep size, implemented into the Fluent standalone solver, for determination of the transient valve angular positions

The force moment M_{n-1} is calculated based on the pressure (P) and Wall Shear Stress (WSS) field from the previous timestep. Firstly, the pressure and WSS are integrated over the leaflet wall. Then, based on the force translation theorem, the resultant force is obtained, and it is transformed to the force moment based on the vector distance from the center of rotation as

$$M_{n-1} = M_{n-1}^{p} + M_{n-1}^{WSS} = \sum_{i=0}^{n_b} (P_i A_i \mathbf{k_i}) \times \mathbf{r_i} + \sum_{i=0}^{n_b} (WSS_i A_i \mathbf{k_i}) \times \mathbf{r_i} \tag{2.30}$$

where n_b represents the number of faces on the boundary of the leaflet, P_i and WSS_i are the pressure and wall shear stress exerted on the leaflet on the i-th mesh face, with its vector indicated as $\mathbf{k_i}$; A_i is the area of the i-th mesh face of the leaflet and $\mathbf{r_i}$ is the vector distance of the mesh face from the rotational axis.

If the valve leaflet position is close to the fully opened or fully closed state, there is a possibility that the leaflet motion in the next timestep is blocked in a position that extends the set limit, for example, in a position of up to 60.3° instead of 60.0°, when $\Delta\theta_{max} = 0.3°$. A similar situation occurs for the limit equal to 0° for the closed state, which is even more important due to the orphan cells generated when the leaflet ex-

ceeds the closed state. Therefore, to avoid such situations, the conditional statement was added which checks whether the angular position in the next timestep θ_{n+1}, calculated as $\theta_n + \omega_n \cdot \Delta\tau_n$, will exceed the angular limit, marked as θ_{lim}. If this is true, the angular velocity, instead determined by Eq. (2.28), is calculated as:

$$\omega_n = \frac{\theta_{lim} - \theta_n}{\Delta\tau_n} \tag{2.31}$$

In this way, the calculated valve motion is realized exactly between the limits set due to its construction or motion registered using fast camera.

2.7 FSI algorithm for the anatomical valve

Due to the low Young modulus of vasculature soft tissue on the level of 0.1 MPa to over a dozen megapascals [42], the two-way partitioned approach for FSI was applied to solve the problem of high deformations. In such approach, the coupling of the fluid and the mechanical solver, i.e. Ansys® Fluent FVM solver and Ansys® Mechanical APDL, FEM solver is introduced. The System Coupling module was used, to change information between these solvers, i.e. integrate pressure and viscous forces obtained from Fluent to provide loads for the Mechanical. Also, this module was used to track transferred data convergence, i.e. relative change on the forces and deformations, transferred during subsequent coupling iterations within every timestep. Here the overall solution procedure and data exchange used in the partitioned FSI approach is presented in Fig. 2.5.

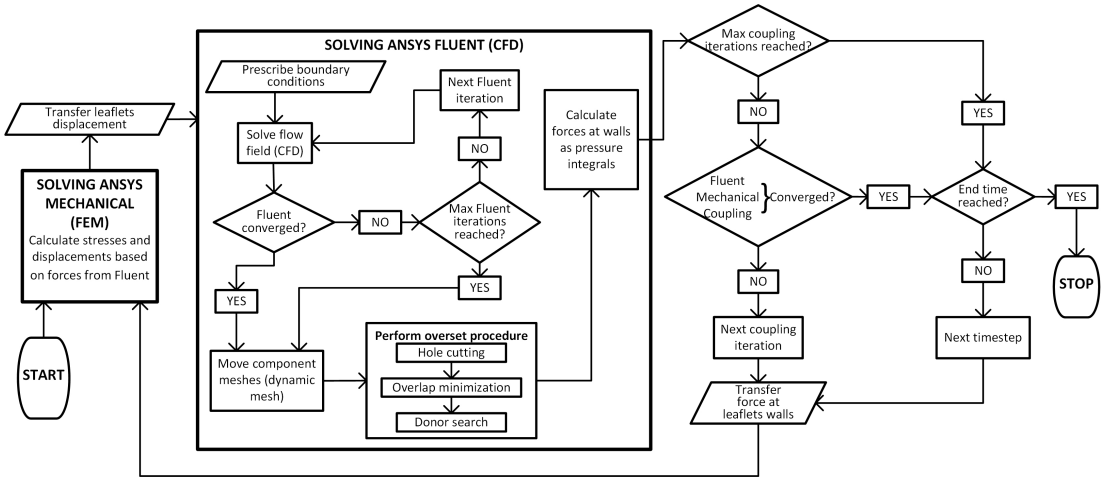

Figure 2.5: Complete flowchart of the prepared 2-way iteratively implicit approach prepared used for the FSI. This procedure was used for the flexible valve model, including the solution of the fluid and structural field, data transferring, and dynamic mesh - overset coupling

The procedure starts with solving the structural field, which calculates leaflet displacements based on fluid forces, coming from pressure and WSS. First, the input data for Mechanical solver come from the Fluent initialization stage, where for all subsequent timesteps, the forces come from the calculated flow field, by integrated pressure and WSS exerted on leaflets walls, as presented in Fig. 2.6. After determination of leaflet displacements, they are transferred back into the Fluent solver, where the fluid mesh is adjusted (by coupled dynamic and overset module) to the new leaflet shape, and then the flow field is solved. Afterwards, new pressure and WSS values are transferred to the Ansys® Mechanical solver. The described procedure is a single *coupling iteration* in a given timestep [51]. The number of demanded *coupling iterations* comes from the convergence characteristics, which refers to both solvers and data transfer values. Namely, the flow and structural residuals need to be sufficiently low; also, the transferred values (forces and displacements) need to differ less than 1% between the previous coupling iteration values. This difference is assessed based on the Root Mean Square (RMS) value and it was checked that for all solution timesteps, the convergence criteria were fulfilled. The RMS is calculated as [51, 103]:

$$RMS = \sqrt{\widehat{\Delta}_l^{\,2}} \tag{2.32}$$

where $\widehat{\Delta}_l$ is the normalized change in the value of the transferred data, compared to the previous coupling iteration:

$$\widehat{\Delta}_l = \frac{\Delta_l}{0.5 \times (max|\phi| - min|\phi|) + |\overline{\phi}|} \tag{2.33}$$

where ϕ is the value of the transferred data, l is the location of these data at the coupling interface, $\overline{\phi}$ is the mean value of the transferred data, and Δ_l is the absolute change of the transferred data:

$$\Delta_l = \frac{1}{\omega} \cdot \left(\phi_l^{curr} - \phi_l^{prev}\right) \tag{2.34}$$

where ω is the under-relaxation factor, equal 1.0, i.e. not modified in the solver settings, ϕ_l^{curr} is the current iteration, ϕ_l^{prev} is the previous iteration.

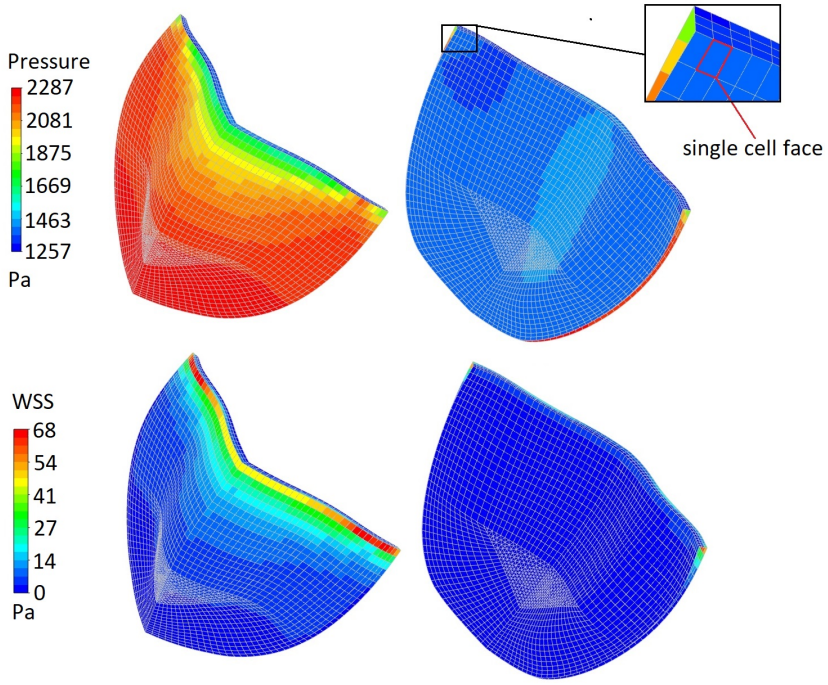

Figure 2.6: Pressure and WSS field exerted on the single 3D leaflet at a given timestep, which is integrated on all the faces of the leaflet cells, to determine the input forces for the structural solver. The structural solver calculates the displacement field, based on applied force field and structural supports

2.8 Indicators of the aortic valve performance

In the thesis, the *hemodynamic* quantities and indicators that are useful for assessing the suitability of the aortic valve were determined, such as wall shear stresses, flow patterns, pressure gradients, regurgitation, pressure drops and Effective Orifice Area (EOA). The use of prosthetic valves must be considered based on their *durability* and *biological response* to the implant [10]. The first aspect involves structural mechanics and material properties, which influence the susceptibility of leaflets and housing to the phenomenon of erosion, resulting from cavitation caused by Negative Pressure Transients (NPTs) [10]. The latter will be investigated in the future author's work by implementation of hemolysis models, as well as mass transport analysis [104, 105].

The artificial valve should not disturb the proper functioning of the cardiac system. Thus, the pressure gradient across the valve should be as small as possible. Higher pressure gradient values can indicate a negative influence on cardiac output, inhibiting proper blood pumping. Moreover, a higher pressure gradient means higher energy losses and more heart workload [10]. To determine the pressure drop at the valve called also as Transvalvular Pressure Gradient (TPG), the difference between the two values is calculated, i.e. the pressure before the valve and after the valve. These values can be determined in the fluid solver as the area-weighted average on the cross-sectional surface.

A common indicator used in the evaluation of aortic valve performance is EOA. This coefficient is the measure of the effective opening of the valve during the forward flow phase and determines how well a valve design utilizes its primary orifice area. It is related to the degree to which the prosthesis itself obstructs the flow [10, 12, 106]. EOA can be calculated using both experimental data and simulation results, with an equation described by Gabbay, based on the principle of energy conservation [12]

$$EOA = \frac{Q_{RMS}}{51.6\sqrt{\Delta \bar{p}}} \tag{2.35}$$

where EOA is the effective orifice area, $\bar{p}$ stands for the mean drop in systolic pressure

and Q_{RMS} defines the root mean square of the systolic flow rate

$$Q_{RMS} = \sqrt{\frac{1}{n}\sum_{i=1}^{n} Q_i^2} \tag{2.36}$$

Blood flowing through the cardiac system exerts forces and stresses on vessels and valves. They can be divided into two components: normal stress, pressure, and tangent stress, WSS. WSS values should fall below the appropriate limits, as too high shear stress (>40 Pa) may cause direct endothelial injury and too low (<0.4 Pa) may lead to the arteriosclerotic plaque [107,108]. In the case of implanted valves, there is some risk of thromboembolism, and therefore patients are on long-term anticoagulant therapy [9, 10]. WSS in the vicinity of the valve is related to the lysis and activation of blood cells, resulting in thrombi deposition in regions with stagnated flow [109]. The wall shear stress is calculated for the laminar flow as follows:

$$WSS = \eta \cdot \dot{\gamma} \tag{2.37}$$

where η is the total viscosity (sum of the fluid and turbulent viscosity) and γ is the local shear rate.

Chapter 3

Artificial valve modeling

This chapter describes the tools and numerical models appropriate for modeling the blood flow through a synthetic aortic valve. The model incorporates the overset mesh technique to capture synthetic valve operation implanted within the aortic root, the aortic arch and the main branches of cardiovascular system. To capture the cardiac system's response and the effect of vessel compliance on the outlet pressure, the lumped parameter model has been also included within the solution procedure. Three different turbulence modeling approaches were used and compared - the laminar, k-ε and k-ω model. The simulation results were also compared with the model excluding the moving valve geometry and the importance of the lumped parameter model for the outlet boundary condition was analyzed. Proposed numerical model and protocol was found as suitable for performing the virtual operations on the real patient' vasculature geometry. The time-efficient turbulence model and overall solving procedure allows to support the clinicians in making decisions about the patient treatment and to predict the results of the future surgery.

3.1 Geometry

The real 8-year-old female aorta model [110], used in the author's work [23] was used in the presented chapter. The geometry was acquired using the Gadolinium-enhanced magnetic resonance angiography. The Geomagic Design X (3D Systems Corporation) [24] was used to convert the base surface triangulated .stl file into the

format supported by Computer Aided Design (CAD) systems. The conversion process included, among others, the STL mesh densification and improving and then auto-surface and loft operations. The aorta model includes: ascending aorta, right subclavian, left common carotid, left subclavian, descending aorta.

However, several operations were performed before the geometrical model depicted in Fig. 3.1 was ready for simulation. Three different regions can be distinguished in the developed model, that is, the ascending and descending aorta, the aortic arch with its major branches, the aortic root with sinuses, and the artificial valve.

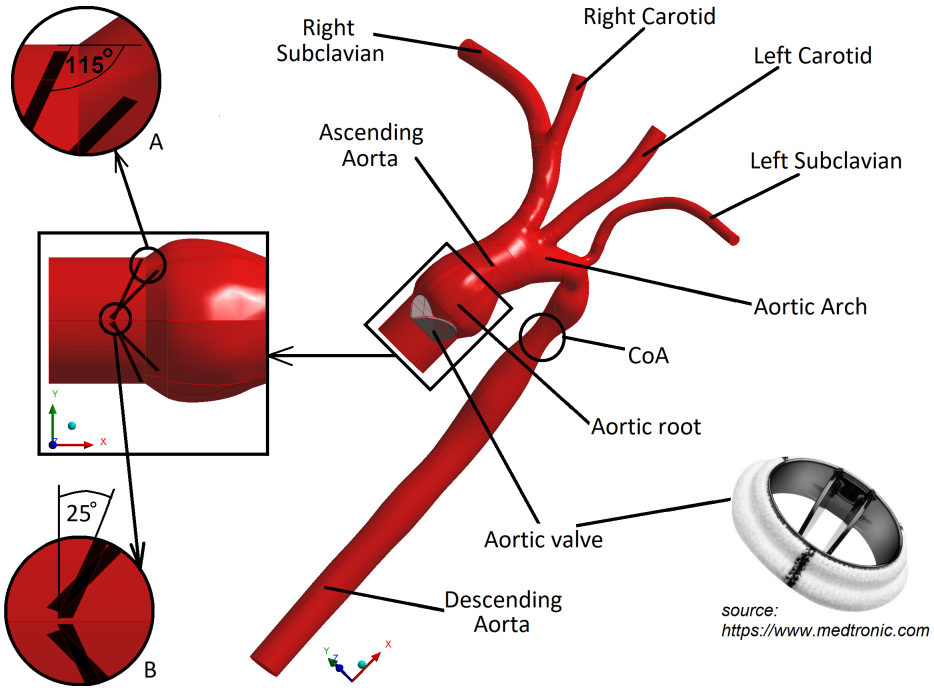

Figure 3.1: Numerical geometry of the aorta with valve and subsequent branches

The aortic root, shown in Fig. 3.2 is the unit that connects the left ventricle and the proximal segment of the ascending aorta. Its function is to support the leaflets of the aortic valve and allow its proper operation [111]. The aortic valve affects laminar flow and proper cardiac output flow [96]. It is composed of the three sinuses of Valsalva and three leaflets or cups. The sinuses end in the Sinotubular Junction (STJ) and the ventriculo-aortic ring.

The three-dimensional (3D) geometry of the aortic root was created based on the measurement data published by [112–114]. Its geometry consists of three identical aor-

tic sinuses. Furthermore, each sinus is symmetric, so only a 60° portion was modeled, and then the mirror operation was performed, resulting in the modeling of the entire sinus. In the inlet section (STJ side), a straight cylindrical tube was added to represent the ventricular portion. It was lengthened up to 13 mm to realize the hydraulic run, for computational stability. On the opposite side, a noncircular tube was constructed to unite the root with the geometry of the ascending aorta. This construction was based on the loft operation of three surface profiles (root surface, mid-surface, aorta cross-section surface), to generate a more smooth transition between the geometries differing with the end face shape. The mid-surface was created based on the magnified mid cross-section of the auxiliary two-surface loft operation.

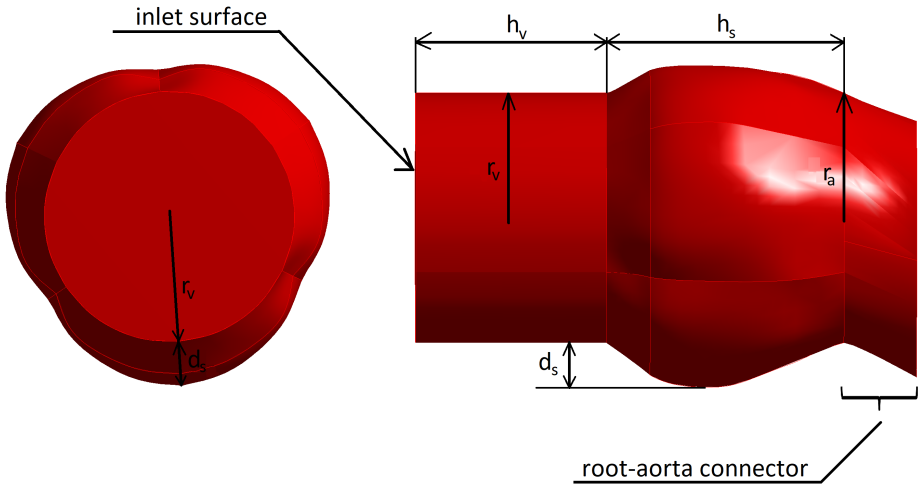

Figure 3.2: Aortic root geometry with marked dimensions, r_a=8.6 mm, r_v=8.6 mm, d_s=3.05 mm, h_s=15.2 mm, h_v=8.94 mm

The geometry of the aortic valve was created based on the user manual provided with the manufacturer documentation. The considered valve's inside diameter is 16.8 mm. The leaflet shape is non-semicircular, because when the closed state is achieved, the angle between the leaflet and the inlet surface is equal to 25° - not 0° (Fig. 3.1). Thus, to obtain the proper shape and chamferings, two semicircular leaflets were created at a 25° angle (closed state) and a greater radius. Then, the slice extrusion operation based on the auxiliary cylinder with the desirable inside diameter was performed to cut out the excess leaflet fragments.

According to [11, 106], even when the valve is in closed state, a small gap exists

between the leaflets (called a b-datum gap, Fig. 3.1 (detail B)) and between the leaflet and its housing (periphery gap, Fig. 3.1 (detail A)). These gaps allow for some level of leakage. According to [115] and due to the conducted observations and analysis, gaps of 0.2 mm were created in these regions. The location of the rotational axis was determined and prescribed in the position located 15% of the valve radius from the centerline of the vessel (Fig. 3.1).

The geometric model of the aortic valve should be scaled to fit the geometry of the aortic root accurately, taking into account the extent of the aforementioned gaps. However, the original 16.8 mm inside diameter size valve was found to perfectly satisfy these requirements and fit correctly in the aorta.

To prepare a geometrical model of the valve that satisfies the requirements of the overset mesh method, several operations need to be carried out. Each leaflet should be extruded in its normal direction with an applied thickness of 2.25 mm to create two separate surrounding geometries, one for each leaflet. Subsequently, these bodies were used to create the overset mesh components. Then, the entire aortic geometry was united with the valve geometry to create the overset background mesh afterwards. The virtual topology utility realized in Ansys Meshing significantly reduced the number of surfaces and edges created in the geometry acquisition process. The effect of this operation improved the mesh quality, due to the great limitation of the unjustified mesh densifying at the wall surface connections.

3.2 Numerical mesh

The background, i.e. aortic geometry, was discretized with the hybrid mesh approach. For this purpose, this geometry was divided into 12 regions and a structurally swept mesh was imposed on each aortic branch, including the ascending and descending aorta (Fig. 3.3). The regions where the branches connect, that is, the aortic arch and the end of the brachiocephalic artery (bifurcation region), were meshed with unstructured tetrahedral elements. The 7 layer boundary layer and the smooth cell size transition between the prism boundary and inner mesh were imposed on the whole aortic geometry.

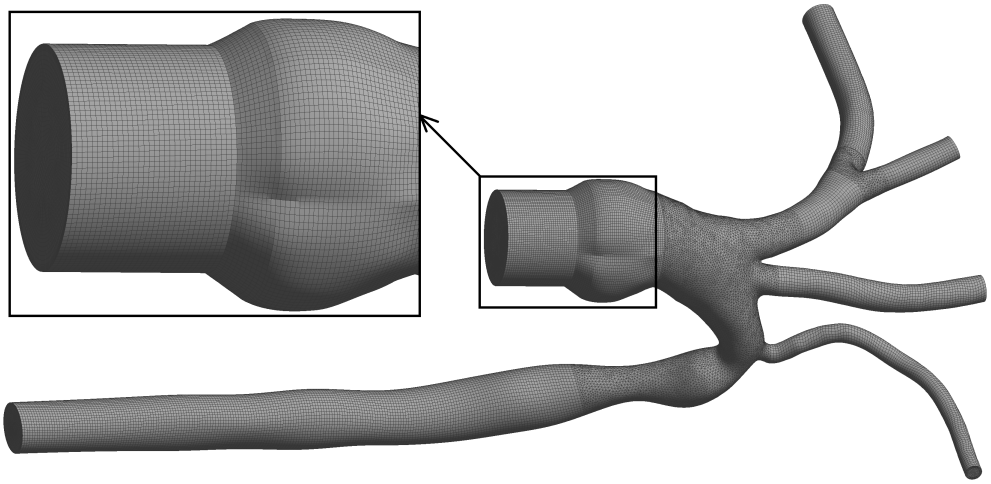

Figure 3.3: Final background hybrid mesh chosen based on sensitivity analysis, 74% of the blood volume consists of the quasi-structural hexahedral elements, rest of the domain was meshed using the combination of the tetrahedrons, pyramids and prisms

To create the quasi-structural mesh, the component geometries were each divided into 18 bodies, meshed individually, with different methods and settings. The body splitting was tested on the geometry with the leaflets in the closed state. It was done to determine the appropriate component bodies creation, i.e. the correct distances from the outward component walls to the leaflet wall, and to determine the proper sizes in the gaps vicinity. The selected methods and cell growth rates ensured the increasing cell size going from all leaflets' walls and the proper quality parameters (Fig. 3.4).

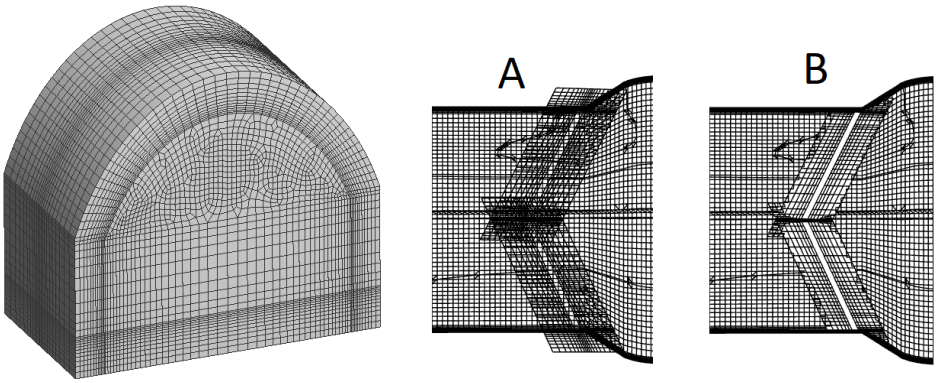

Figure 3.4: Final overset component hex mesh chosen based on sensitivity analysis, cross-section through the background and components meshes, **A** - before the matching process and **B** - after matching process

The mesh sensitivity analysis was performed on three different meshes differing in the number of elements. These meshes were applied for solving all three turbulence models, i.e. 9 models were solved for the uncertainty analysis. First, the connectivity of the overset mesh was tested with the whole range of the leaflet angle using the UDF `define_cg_motion`. The corresponding background and component mesh settings and densities were adjusted until the orphan cells were not present at any leaflets' position. This may occur here when the background mesh resolution is much different than the last layers of the components mesh, or there are too few cells across the gap. The subsequent meshes were prepared for the sensitivity analysis: *coarse* (background 773,000 cells, component 31,000 cells), *medium* (background 1,199,000 cells, component 55,000 cells) and *fine* (background 1,565,000 cells, component 94,000 cells). The impact of the mesh density on results was evaluated on the basis of global and local quantities, i.e. the outlet pressure (area-weighted average) from the descending aorta and the local pressure (single node value) in the boundary layer of the aortic root. For the stability of the solution, four heart cycles were calculated, as the values in the fourth cycle already differed insignificantly.

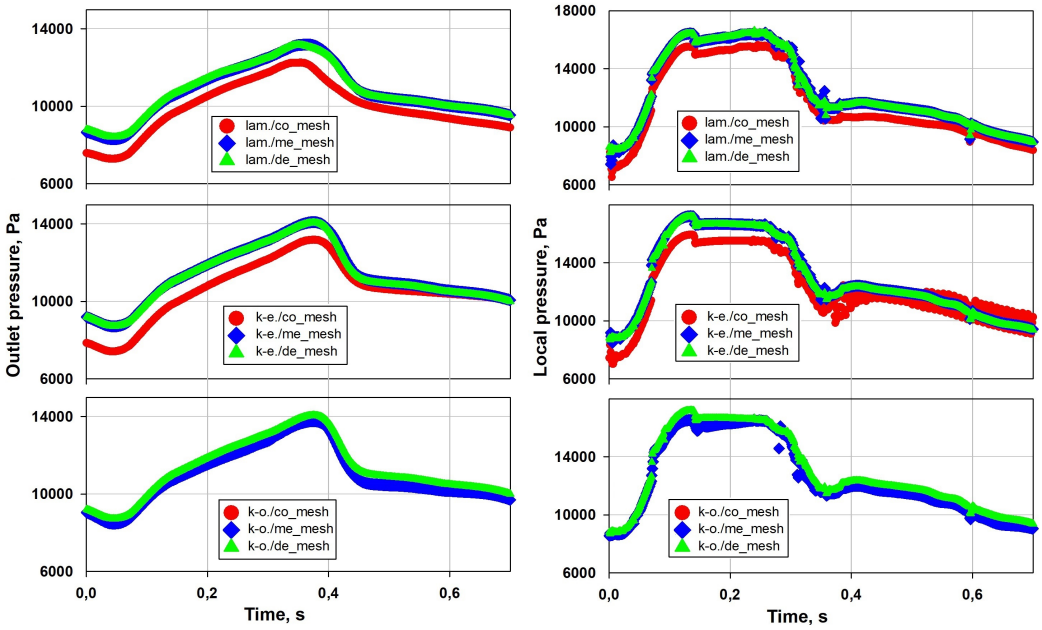

Figure 3.5: Mesh sensitivity analysis, for the laminar (upper), k-ε (middle) and k-ω (lower row); left column - outlet pressure from descending aorta; right column - local pressure in the aortic root. Red marker - coarse mesh, blue marker - medium mesh, green marker - dense mesh

The results are presented in Fig.3.5 where time 0 s means the beginning of the last calculated cycle. The biggest differences between the results of mesh type were observed in the laminar and k-ε models; however, for the *medium* and *dense* type, no significant differences were identified, neither for the global nor for the local pressure values. Finally, the conclusion was made that further mesh densification does not influence the results and the *medium* type was chosen for the analysis.

3.3 Model setup

The Carreau viscosity model and density of 1051 kg/m^3 was applied [36,116], as the blood physical properties. For the inlet boundary condition, the velocity time profile was established, presented in Fig. 3.6, whereas for the outlets the Windkessel electrical analogy model was implemented.

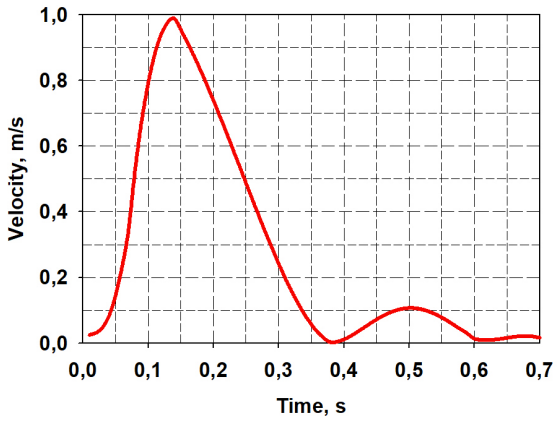

Figure 3.6: Velocity-inlet profile is set as the boundary condition

The locations of resistance and compliance on the electric diagram are shown in Fig. 3.7. The values of the resistors and capacitors for the main vascular branches are collected in Tab. 3.1. To solve set of the ODE (2.19), the fourth-order Runge-Kutta technique with adaptive control of the integration time [117] was used. This solver is invoked within each iteration of the solution process in every time step:

$$
\begin{aligned}
k_1 &= hf(x_n, y_n) \\
k_2 &= hf\left(x_n + \frac{h}{2}, y_n + \frac{k_1}{2}\right) \\
k_3 &= hf\left(x_n + \frac{h}{2}, y_n + \frac{k_2}{2}\right) \\
k_4 &= hf\left(x_n + h, y_n + k_3\right) \\
y_{n+1} &= y_n + \frac{k_1}{6} + \frac{k_2}{3} + \frac{k_3}{3} + \frac{k_4}{6} + O(h^5)
\end{aligned}
\tag{3.1}
$$

where $O(h^5)$ is called as 4-th order error and h is the stepsize changed dynamically during solution procedure.

During the solution process, the variation of the calculated pressure for each outlet is monitored. As the termination criteria, the pressure stability and residual of the continuity equation (value $< 10^{-6}$) were selected.

Table 3.1: LPM model parameters

Artery name	Abbrev.	R_1, $\mathrm{kg \cdot m^{-4} \cdot s^{-1}}$	C, $\mathrm{m^4 \cdot s^2 \cdot kg^{-1}}$	R_2, $\mathrm{kg \cdot m^{-4} \cdot s^{-1}}$
Right Subclavian	RSA	$0.885 \cdot 10^8$	$7.13 \cdot 10^{-10}$	$1.3858 \cdot 10^9$
Right Common Carotid	RCCA	$1.122 \cdot 10^8$	$5.62 \cdot 10^{-10}$	$1.7571 \cdot 10^9$
Left Common Carotid	LCCA	$1.124 \cdot 10^8$	$5.62 \cdot 10^{-10}$	$1.7611 \cdot 10^9$
Left Subclavian	LSA	$2.895 \cdot 10^8$	$2.12 \cdot 10^{-10}$	$4.5361 \cdot 10^9$
Descending Thoracic Aorta	DA	$0.271 \cdot 10^8$	$2.92 \cdot 10^{-9}$	$0.3122 \cdot 10^9$

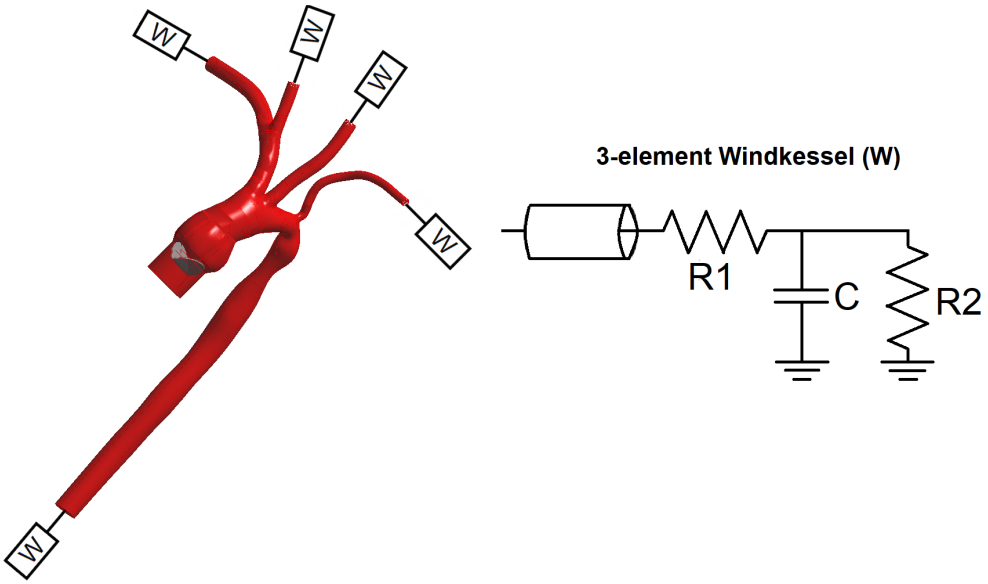

Figure 3.7: Construction of the electrical circuit (marked as **W**) for the arterial tree with five outlets

Figure 3.9 presents the overall solution flowchart. To allow modeling of movable rigid structures, the valve angle time functions were taken and adapted from [55]. In the mentioned research, the Curvilinear Immersed Boundary (CURVIB) method was implemented to model the FSI phenomenon acting between the dynamic movement of the left ventricle wall and the mechanical bileaflet valve. The leaflet kinematics calculated by the authors [55] agree well with the experimental data. The three-dimensional geometry, utilized pulsatile inlet profile, as well as the coincidence with the artificial valve type and motion range considered in this research, allows to implement the calculated leaflet angle motion in the solution procedure.

The x-axis range was scaled from 1.16 s to fit into heart cycle time used in this research, equaling 0.7 s. Then, for each leaflet, the angle polynomial time functions $\theta(\tau)$ were created. Finally, angular velocities were calculated as time derivatives $\omega = \frac{d\theta(\tau)}{d\tau}$, since this is the input value of the UDF macro `define_cg_motion`. Additionally, the proper ω functions signs must be chosen, depending on the direction of rotation. The final angular velocity function is formed as

$$\omega(\tau) = \frac{\pi}{180^\circ} \cdot (a_1 \cdot \tau + a_0) \tag{3.2}$$

where the multiplier $\pi/180^\circ$ is used to transform degrees into radians, and the values

of the polynomial coefficients (a_1, a_0) are listed in Tab. 3.2 and Tab. 3.3 for each of the time intervals. The angle curves are shown in Fig. 3.8.

Table 3.2: Angular velocity - time function coefficients for the upper leaflet

	Upper leaflet	
time interval, s	a_1	a_0
$0 \leq \tau \leq 0.03922$	1089.47	-1551.04
$0.03922 \leq \tau \leq 0.2323$	0	0
$0.2323 \leq \tau \leq 0.29569$	3549.38	-782.32
$0.29569 \leq \tau \leq 0.35603$	8584.5	-1972.46
$0.35603 \leq \tau \leq 0.7$	0	0

Table 3.3: Angular velocity - time function coefficients for the lower leaflet

	Lower leaflet	
time interval, s	a_1	a_0
$0 \leq \tau \leq 0.0453$	-15869.63	1684.82
$0.0453 \leq \tau \leq 0.2353$	0	0
$0.2353 \leq \tau \leq 0.3047$	-14719.57	3537.327
$0.3047 \leq \tau \leq 0.3126$	0	-3594.646
$0.3126 \leq \tau \leq 0.3247$	-54899.38	18320.64
$0.3247 \leq \tau \leq 0.356$	1319.85	-767.89
$0.356 \leq \tau \leq 0.7$	0	0

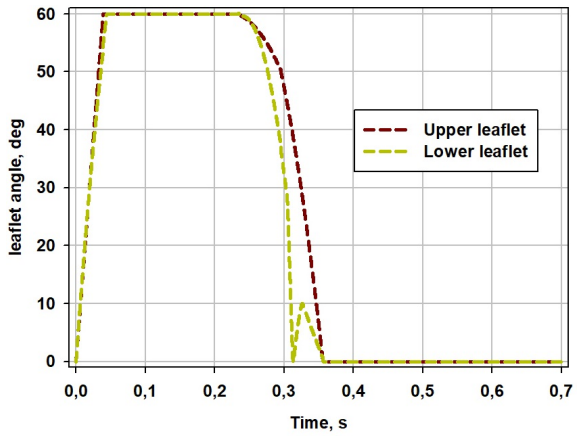

Figure 3.8: Leaflet angle profiles. The value of 0° refers to the fully closed state

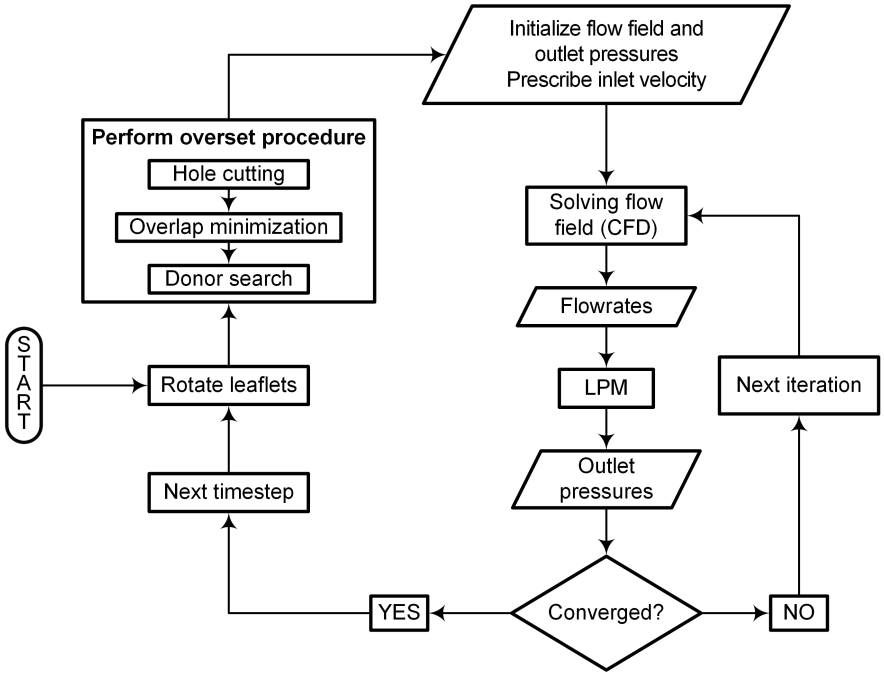

Figure 3.9: Applied solution procedure for modeling of movable rigid structures

3.4 Results

To assess the character of the flow in the vicinity of the artificial valve, a cross-sectional surface was created, where the most turbulent flow is expected, and the estimated Reynolds number $Re = \rho u d_e / \eta$ was calculated, as was done in the published research of the author [23]. The characteristic dimension depends on each case. For the flow through the pipe, d_e is assumed as pipe diameter; here, the calculated equivalent diameter was determined with equation $d_e = \sqrt{\frac{4V}{\pi H}}$, where V is the volume of the body shown in Fig. 3.10 and H the length of the body. The local value of the viscosity η was calculated by Fluent from the Carreau model. As the velocity in the equation for the Reynolds number is related to the whole object, the area-weighted average value was used for u. Figure 3.10 presents the local values of the estimated Reynolds number, located in the cross section through the aortic root. The contours are shown for the moment when the leaflets are moving with the high velocity, i.e. at 0.30 s, and for the maximum inflow, at 0.14 s, which may produce turbulent effects. The maximum local values are on the level of 1500 and 5500, respectively. As this similarity number

relates to the whole object, the average *Re* number was calculated as the area-weighted average through the cross-section. This will give some indicative values that will show whether the flow might be turbulent or not. The values of 1040 for 0.30 s and 3770 for 0.14 s were obtained. This acknowledged the necessity of applying approach for the turbulence modeling.

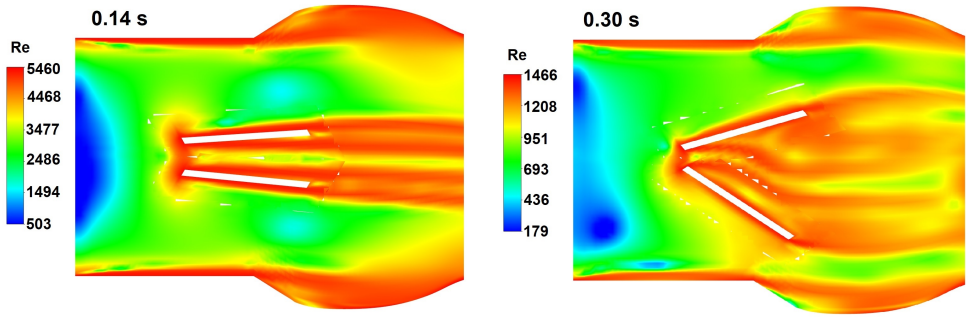

Figure 3.10: Local values of the Reynolds number, determined based on its definition, to assess the necessity of turbulence model usage

Two RANS turbulence models were used instead of the full DNS model, to choose a time-efficient model that could be implemented for virtual patient therapies. The results of those models were compared and the most appropriate model was selected and also used in the research presented in the Chapter 4. and Chapter 5.

To evaluate the validity of the results of the k $-$ ε realizable and k $-$ ω SST model, the values of both models **Turbulent Kinetic Energy** (TKE) were compared with the PIV measurements performed by [77] and [118]. In [118], a 3D PIV experiment was performed to assess blood flow patterns in a very similar aortic geometry with the same type of mechanical valve. The results of two valve configurations, differing in placement by 90° were compared. The conclusion was made, that the configuration of the mounted valve affects insignificantly onto turbulent characteristics. Thus, the PIV results could be compared with those obtained by the model, due to almost the same geometry, similar inflow profile, and results independent of the valve configuration.

Each of the velocity components at the specific time point is decomposed into the medium (time averaged) and the fluctuation part: $u = \bar{u} + u'$, $v = \bar{v} + v'$, and $w = \bar{w} + w'$. The turbulent kinetic energy represents the mean kinetic energy per unit mass

associated with eddies in the turbulent flow [33, 45] and is expressed as

$$TKE = \frac{1}{2}\left(\bar{u}'^2 + \bar{v}'^2 + \bar{w}'^2\right) \tag{3.3}$$

where the values u', v' and w' are the fluctuations from the velocity components in the x, y, and z directions, accordingly. In [118] the fluctuating velocity patterns were obtained by the PIV measurements to calculate the time-varying TKE. The domain (blood volume) used in the analyzed model was split in Fluent into two parts, where the smaller part, ventricular extension and aortic root, was used to calculate the volume-average of TKE. The splitting operation was performed to determine the values based on the same geometry scope, as was done in comparative research [118]. As shown in picture 3.11, the values are highly dependent on the inlet velocity profile and also on the leaflet movement. The same regularity was observed in [118]. The maximum values in [118] were on the level of 5.8 J/m^3, for the maximum flow of 145 l/min, where in this research analysis the maximum flow was equal 240 l/min. Based on the scaling factor of the research [77], where TKE was measured for different mass flows, it should be expected that the TKE values are at the level of 22 J/m^3. For the $k-\varepsilon$ turbulence model, close maximum values were obtained of 17.5 J/m^3, where for the $k-\omega$ model these values are lower, on the level of 8 J/m^3. Finally, the conclusion was made that the results obtained using the $k-\varepsilon$ model were much closer to those acquired by PIV measurements than using the $k-\omega$ model, because the latter produced underrated values of TKE. Thus, in this section, described results are related to the model $k-\varepsilon$.

The pressure drop was calculated between two points located on the centerline, 3.5 mm before the valve and 3.5 mm behind, considering its opened state. Fig. 4.15 (red curve) shows the pressure drop between the indicated points. The monotonicity of the curve is concurrent with the inlet velocity profile. The oscillations are visible during the moments when the valve is moving and are more apparent when the valve becomes fully closed or fully opened. The maximum value achieved about 1.0 kPa and is very close to the validated pressure drop values in [79] and [119], where the pressure drops are slightly higher than 0.8 kPa and 1.3 kPa, respectively.

To observe the influence of the separated velocity profile on the pressure drop, addi-

tional calculations were performed for the case that excluded the moving valve, which contained the interior of the aorta filled with total blood. The maximum pressure drop was 4.5 times lower than in the valve-equipped model. The conclusion was made that the transvalvular drop oscillations are more dependent on the leaflet movement than on the inlet velocity profile (Figs. 3.6 and 4.15).

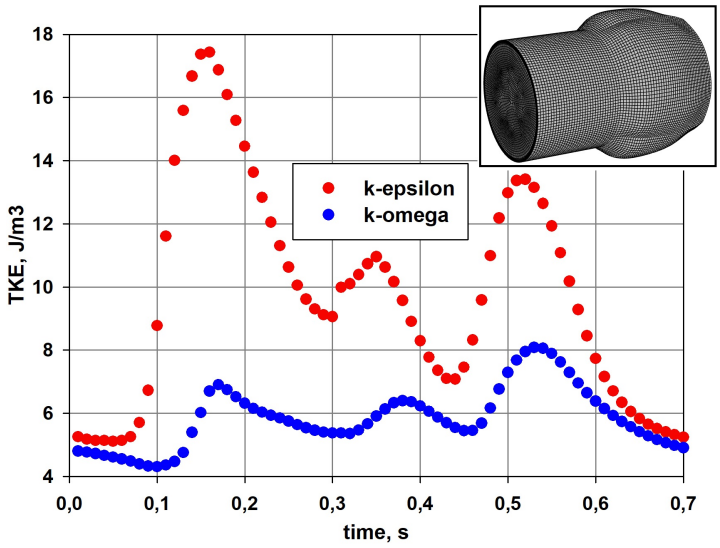

Figure 3.11: Turbulence kinetic energy calculated in the vicinity of the valve shown at the inset for two RANS turbulence models

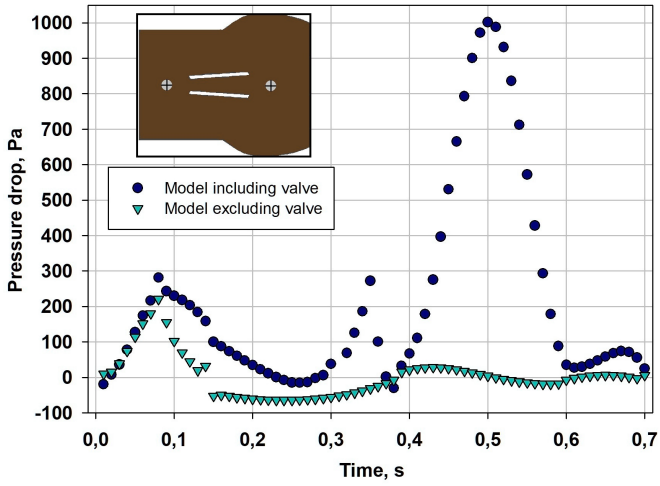

Figure 3.12: Pressure drop calculated between two central points shown in the inset for two models analyzed

Figure 3.13 presents the velocity components, streamwise (x-velocity) and vertical (y-velocity). Five different time instants were considered: the moment when valve started to open (0.01 s), the opening completion (0.05 s), the maximum inflow time (0.14 s), the closing start-up (0.24 s) and closing completion (0.36 s). The x-velocities are plotted on three lines located behind the valve, in its middle cross-section. The y-velocity is plotted for the centerline of the valve. The bottom right picture fragment shows the line locations.

Valve regurgitation is undesirable and can be observed when the valve is fully closed due to leakage areas [10]. Regurgitation reduces the net flow through the valve; however, the backflow contributes to the leaflet washout. Some degrees of this phenomenon is visible close to the sinus wall region when the valve is starting to open and when it is closing, nevertheless, considering the values presented on the scales, this phenomenon is not substantial. As the upper leaflet begins to close slightly earlier than the lower leaflet, thus in moment *0.27 s* discussed effect is present only in the upper gap region. The streamwise velocity distributions remain quite similar moving away from the valve and its changes are related to local maxima stabilizing and the influence of 3D aortic geometry. When the fully opened state is achieved, the flow field is visibly divided into three quite symmetrical regions - one central and two lateral. The unsymmetrical irregular patterns at the beginning of the heart cycle are related to the stagnation of the flow and are rapidly eliminated with the increasing inflow. The greatest difference between maximum and minimum streamwise velocity values is equal to 1.3 m/s and is observed just behind the valve during the peak systole phase.

The axial velocity (Fig. 3.13, red curve) falls behind the maximum 0.081 m/s and minimum -0.081 m/s values. When the leaflets are fully open and stationary, the courses become highly dependent on the curvature of the geometry of the ascending aorta. In addition to these moments, the vertical velocity depends almost only on the motion of the unsymmetric leaflets.

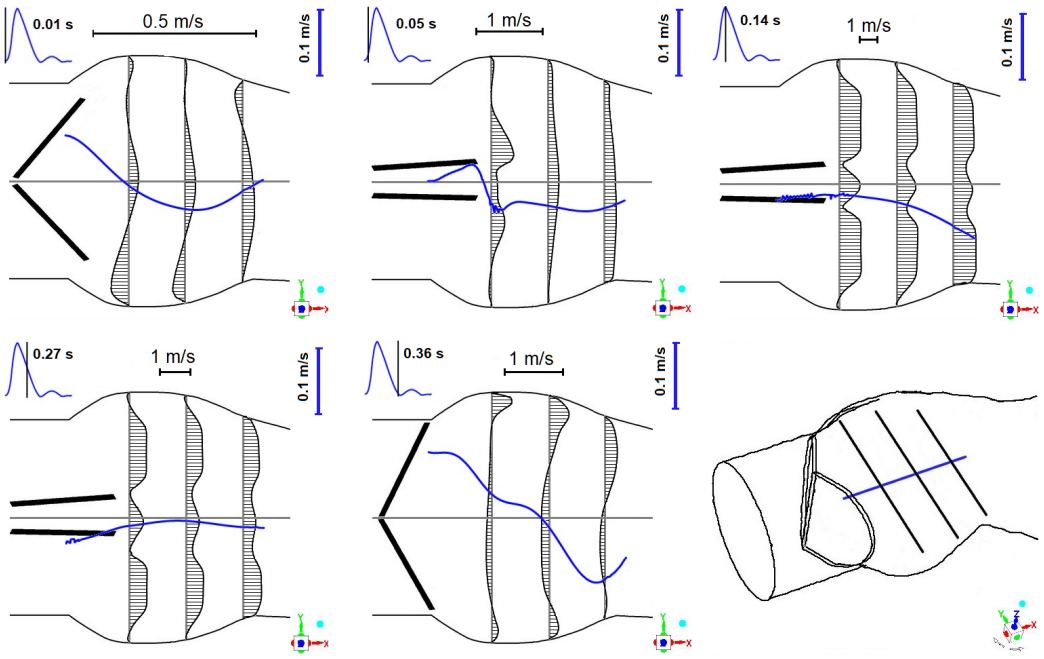

Figure 3.13: Streamwise velocity profiles for three locations (x-velocity, hatched graphs) and the vertical velocity component (y-velocity, red curve)

The velocity vectors for two time instants: 0.03 s (mid opening) and 0.30 s (mid closing) are presented in Fig. 3.14. For the entire heart cycle, they can be found on the videos attached in the supplementary materials. When reversed flow is present in the leaflet vicinity during the fully closed state (from 0.4 s to 0.7 s), these reversed velocity values are very low. Thus, the valve motion in this time interval seems to be not probable, which proves that leaflet time angle profiles are properly selected and implemented. Some minor vortices can be observed near the sinus walls, mainly when the inlet velocity decreases, and they are present in the aortic root section during the closed state of the valve, due to the time-varying inflow. The motion of the valve entrains a certain amount of blood, creating some weak swirls. A maximum velocity value equal 4.08 m/s was observed at the peak systole (0.14 s) in the CoA region.

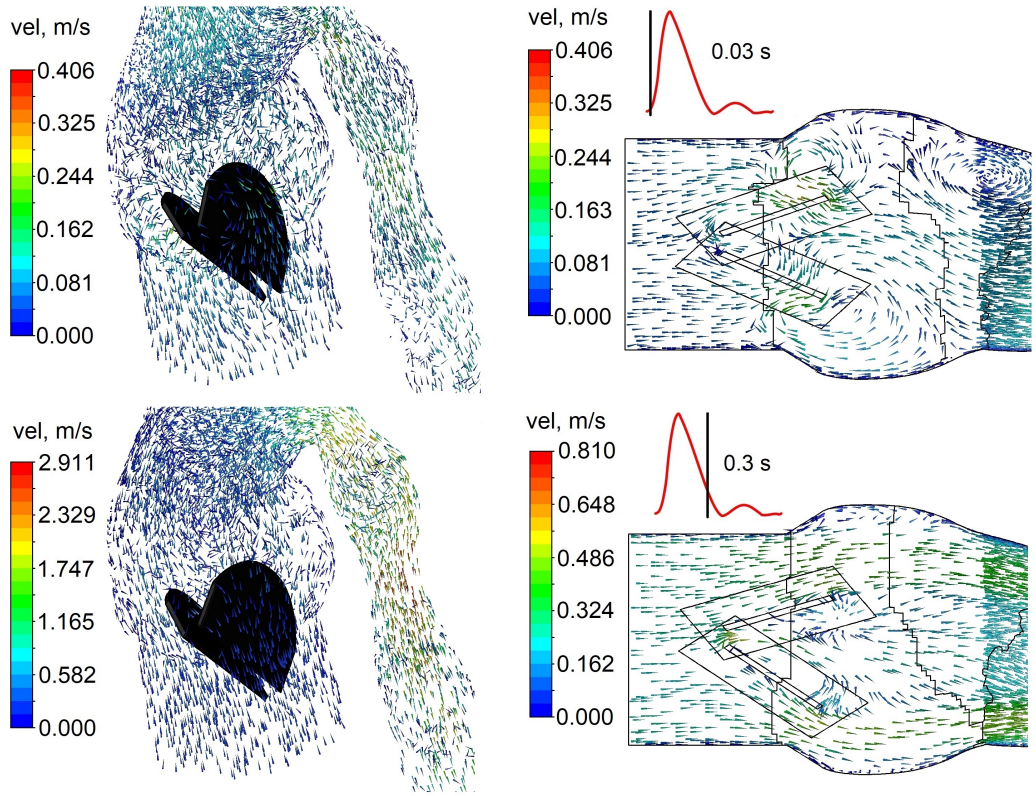

Figure 3.14: Velocity vectors for the valve vicinity and the valve middle cross-section, presented for two time instants while the leaflets are moving

Valve stenosis results in low effective orifice area values, which is related to increased pressure loss and increased heart workload. The bileaflet type mechanical valve construction overcomes the drawback of low EOA values related to former mechanical valve types - caged-ball and ball-and-cage [106]. The EOA typically falls between the values $1.04 - 4.05$ cm^2 [10]. For the same type of construction, it is proportional to the diameter of the valve and may vary in patients [120]. The measured value by [120] for the St Jude Medical® bileaflet valve was equal 2.08 cm^2 and 3.23 cm^2 for size 21 mm and 25 mm, respectively. The value calculated using simulation results considers the 21 mm type (with inside diameter equal 16.8 mm) and was equal to 3.08 cm^2, which indicates the appropriate performance of the prosthesis.

Despite advances in hemodynamics, medical equipment, and replacement, the problem of hemolysis, thrombus deposition, and cavitation bubbles is still present with mechanical valves. High and low pressure values are present on both leaflets' sides at the edges, especially when the closed state is achieved (Fig. 3.16). These high gradients

could be successfully calculated with the described numerical mesh.

Negative Pressure Transients (NPTs), also called surges, are the high and rapid pressure drops [121]. They are caused here by the transient velocity and the moving solid body elements. NPTs could result in cavitation, which is the rapid vaporization and condensation of the fluid in the region with pressures below the vapor pressure. This is especially noticeable with valves equipped with rigid occluders. This phenomenon was investigated and described by [122]. In conclusion, low NPT values during a period of about 1 ms resulted in cavitation bubbles, the presence of which is one of the factors that cause structural failure and deterioration of the leaflet. Thus, the longevity of mechanical valves is about 25 years [10]. The significance of the NPTs phenomenon is highly dependent on the dynamics of aortic valve closure and the pressure loading rate. The time angle profiles of the leaflets shown in Fig. 3.8 show the abrupt closure of the leaflets. Fig. 3.15 presents the minimum pressures at the leaflet walls. It is observed that the pressure values are changing rapidly, especially during the time from 0.30 s to 0.31 s. This is the moment when the leaflet angular velocity is very high and the lower leaflet closure is almost complete, to open subsequently for a while (compare with Fig. 3.8). The results presented coincide with the conclusions for the presence of cavitation bubbles made by [122] and suggest that there is still room for improvement in the optimum mechanical valve geometry and material improvement. However, further investigation on the numerical modeling and test rig validation has to be made to make a proper assessment based on the pressure and WSS results, i.e. the cavitation and hemolysis models should be implemented.

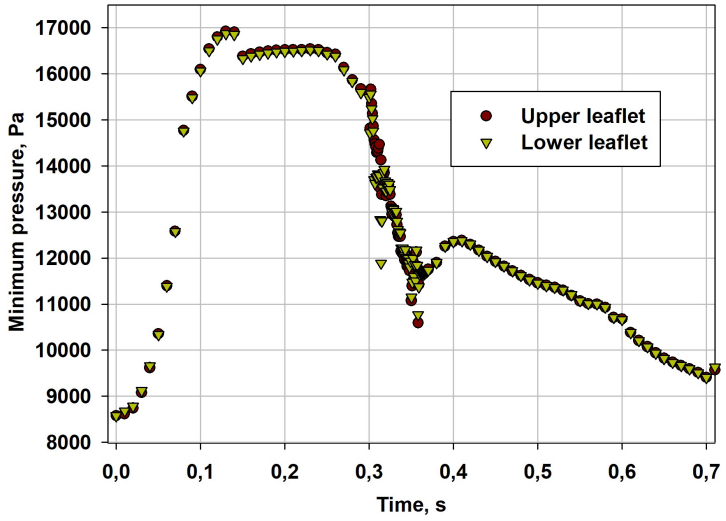

Figure 3.15: Minimum pressure values observed on the leaflets' surfaces

Fig. 3.16 presents the pressure and wall shear stress contours on the leaflet walls, together with the pressures in the valve surroundings - at two perpendicular valve symmetry planes. Two different time instants are demonstrated for both quantities. Pressures (left side) are presented for the maximum inflow (0.140 s), and the closure completion (0.360 s), which is the moment of minimum leaflet pressure. The WSS (right side) are plotted also for the maximum inflow (0.140 s) and besides for the and maximum WSS occurrence (0.310 s). These results indicate high gradients, visible especially at close-ups and at the leaflet edges. Gradients come from blood, which flows through the leaflets and hits the sharp surfaces. Furthermore, they resulted from the unsteady inlet velocity and the valve movement. In such cases, the mesh composition and densification must be adopted correctly.

The maximum and minimum pressure and WSS values are generally observed in the vicinity of gaps. Depending on the angle of the leaflet, they can be seen around the periphery gap (when near the open state) or the B-datum gap (when near the closed state). This agrees with the locations of cavitation bubbles observed in studies related to bileaflet valves ([10, 123, 124]). The minimum pressure on the leaflets surfaces was equal 8.5 kPa at the beginning of the heart cycle. The rapid change in the pressure value is observed in the time interval of 0.02 s, when leaflets are moving with high angular velocities (compare with Fig. 3.15). Depending on the vasculature of the patient, their

state of health and activity, the presence of the artificial valve could be sufficient to promote minor cavitation on its surfaces.

The pressure contours plotted at the cross-section planes show decreasing values coming from the inlet. This remark is correct for the specified time instants and is not valid and physiological for the entire heart cycle (compare with Fig. 3.17 and attached animations). The physiological time pressure distributions could be properly modeled by Windkessel implementation. The maximum pressure exerted on the leaflets was during the peak systole phase (0.14 s) and was equal to 18.2 kPa (i.e. 127 mmHg). During the closed state (from 0.36 s) the leaflet pressure distribution is more regular, with the local extrema on the sides.

The WSS values are high in the time of increased inlet velocity and from the moments when the valve starts to close. The maximum value equals 85 Pa in time instant 0.49 s. As mentioned, high WSS values contribute to blood damage, lysis and platelet activation. This can happen when the values are on the level of 150-400 Pa [125], however, in the case of the presence of a foreign solid surface, much lower WSS values can cause hemolysis. Proper anticoagulation treatment is required for patients. The problem could be minimized by improving the material design and leaflet geometry, especially by affecting the closing dynamics, while maintaining the proper valve characteristics. The findings of other researchers ([78]) state that when the Bental procedure (which is the simultaneous replacement of the valve, aortic root, and ascending aorta) is performed, it is better to take into account the irregular shape of the root. Compared with the circular tube applied instead, the valve closure velocity is 250% lower. Thus, including the specific shape of the aortic root can limit the effect of lysis and cavitation in the case of Bental operation.

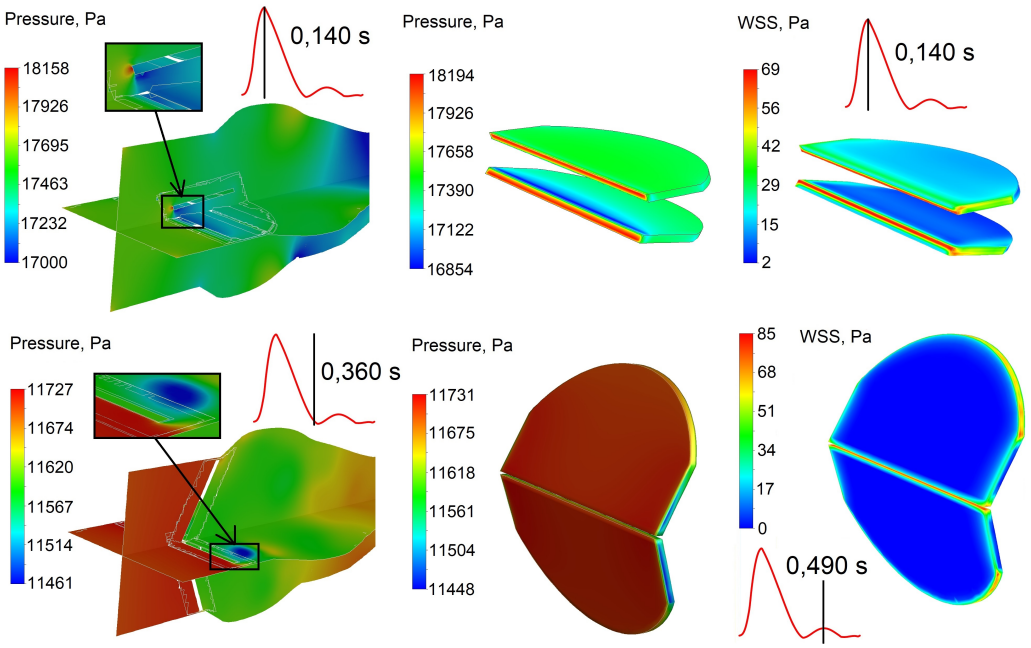

Figure 3.16: Contours of pressure (first and second from the left) and wall shear stresses (right side) for different time instants

Figure 3.17 presents the contours of pressure exerted on the blood walls. The upper part of the figure relates to the model including the aortic valve and the lower part, excluding the valve. Three time instants are presented: the peak systole phase (0.14 s), the diastole phase (0.62 s) and the moment between them (0.45 s). It is observed that the pressure levels are similar in both models; however, the pressure distribution is much different. This results from the resistance to the flow that the valve generates. The contour of the pressure in the aortic root region and the extension of the ventricular strongly depend on the presence of the valve, especially when it is closed (0.45 s). These facts suggest the usefulness of including the appropriate valve, natural or artificial, when the blood flow of the aortic system is modeled to generate more physiological results. In the CoA region, the minimum local pressure is observed due to the narrowing of the vessel. Figure 3.18 presents the pressure drop for the whole cardiac cycle, calculated between the two central points, both placed 1 cm from the narrowing center. The values are very similar for both models – both with and without valve, which could be due to the fact that CoA is quite distant from the valve. The biggest differences are observed when the leaflets move. Research [126] investigates

the influence of narrowing removal on CFD results and states the positive influence of replacing with straight section.

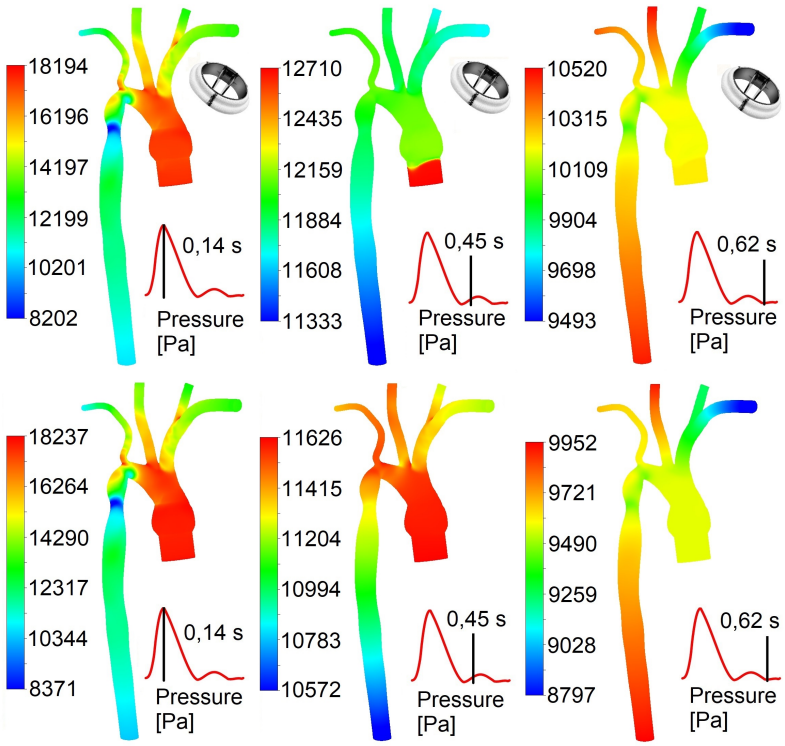

Figure 3.17: Wall pressure comparison. Three time instants are presented: 0.14 s, 0.45 s and 0.62 s. The upper part of the arrangement refers to the model including valve (source of the valve picture: https://www.medtronic.com)

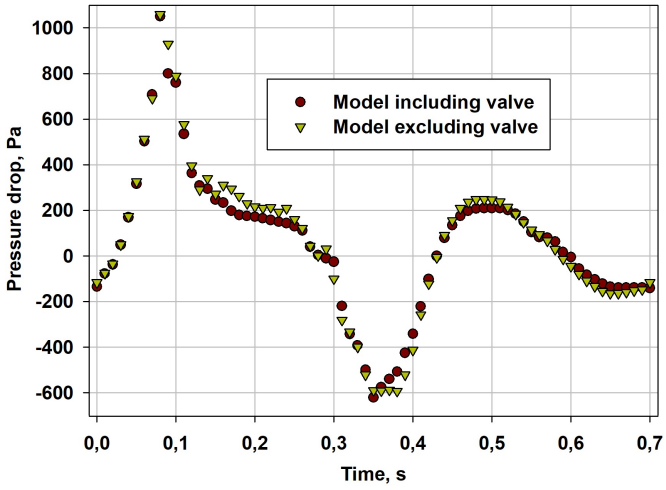

Figure 3.18: Pressure drop across the CoA

The outlets pressures and mass flow values were monitored during the whole solution process. The pressures were calculated using the lumped-parameter Windkessel model, and imposed as the boundary conditions. To achieve repeatable results, the model excluded moving valve demanded calculation of seven heart cycles, where in the model with the valve, four cycles were recognized as sufficient to state repeatability. This regularity was also checked for other monitored values, such as pressures at the walls of the blood vessels. The reason for described differences in the speed of solution stabilization is the lowering of the gradients in the outlets vicinities in the case with the valve. Figure 3.19 presents the calculated outlet pressures and mass flows for the last calculated cycles. As mentioned previously, the valve produces the resistance for blood flowing through the domain, however, for the outlet pressure values, substantial differences were not observed between the model including and excluding valve. The greatest fluctuations are observed 0.32 s from the cardiac cycle beginning. At this moment, the leaflets are moving with high angular velocity and the closure is ending, especially for the lower leaflet, which after the closure opens slightly for about 0.04 s. The similar conclusions for fluctuations were performed for the leaflets pressure (compare with Fig. 3.15). Maximum pressures were observed at the right subclavian and left common carotid artery 0.27 s from the beginning of the cycle and were equal to 136 mmHg and 137 mmHg, including and excluding the implanted valve, respectively.

The mass flows are presented at the lower part of the figure. The positive values are related to the blood flowing into the domain (i.e. reversed flow). It is observed that the valve closure is causing an increase amount of fluid going back into vessels. This observation confirms the physiological results of the model, as the human aortic valve motion invoked by heart compression entrains some amount of blood, changing the velocity field. Physiologically, such reversed flow is compensated by the vessel dilation, as the leaflets work to obstruct the flow for a certain time interval.

To investigate the impact of the Windkessel model and the usage of multiple outlets on the results, the geometry and numerical mesh of the additional aortic model was prepared, with truncated upper branches, so here one outlet was used (Fig. 3.20). For the geometry preparation, special care was taken in order to avoid the sharp edges that come from cutting the branches. The new background hybrid mesh (approximately 1

mln elements) was created based on the sensitivity analysis of the full geometry scope, so the imposed densities came from the *medium* type mesh. The chosen turbulence model $k-\varepsilon$ was also used here. Two models were solved in the geometry scope described: the model with the windkessel outlet boundary condition and the simple 0 Pa gauge pressure outlet boundary condition. This way it could be estimated, how the extended geometry scope, and how the implemented 0-dimensional model with electrical analogy influences onto results. Local quantities were considered - pressure drops at the valve and at the CoA, and global quantities - average pressure exerted on the blood walls in the heart cycle (Fig. 3.20). Also, EOA values were calculated, where for *truncated 0 Pa* and *truncated Windkesel* were equal 3.17 cm^2 and 3.16 cm^2, accordingly. This was very close to the EOA of the reference model (3.08 cm^2).

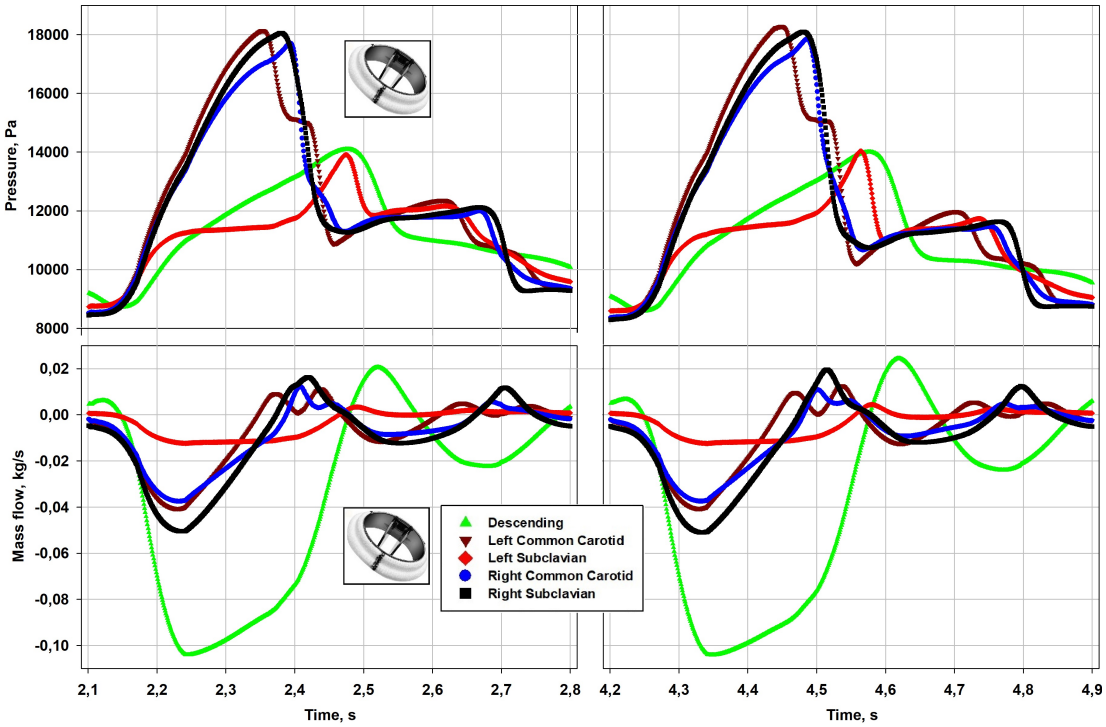

Figure 3.19: Pressure (upper) and mass flow (lower) at the outlets. The left part relates to the model including valve and the right - without valve (source of the valve picture: https://www.medtronic.com)

For the truncated models, the pressure differences, i.e., pressure drops across the valve and the CoA, are almost the same. This could come from the quite long distance between these locations and the outlets. However, this similarity is valid only for the difference, since the values before and after specified locations are substantial. This

remark is analogous to the area-weighted average of pressure exerted on the walls of the blood (Fig. 3.20, lower left part); the values differ between three models, where the model analyzed in the Results section *(reference model)* presents the most physiological values of pressure, on the level of 100 mmHg. The truncated models present underrated values for the 0 Pa outlet gauge pressure, and overrated values for the model including Windkessel outlet boundary condition. Thus, the final conclusion was made that, in order to produce globally proper results, valid not only for the local indicators, usage of the extended geometry scope with the outlet boundary condition based on electrical analogy is preferred.

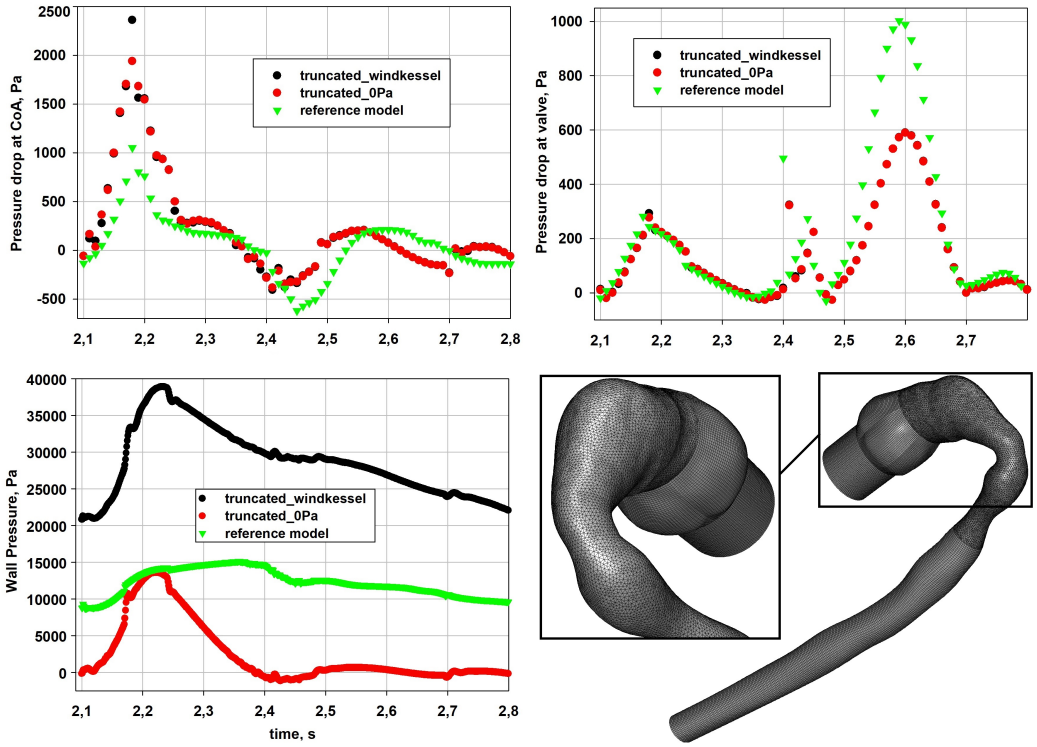

Figure 3.20: Comparison of the model results with the model that excludes the upper branches, where two types of outlet boundary condition were used. The reference model (green markers) is related to the base model chosen regarding the sensitivity analysis ($k-\varepsilon$, medium mesh). The numerical mesh for the truncated model is shown at the lower right part.

The supplementary video materials can be found using the above QR code or the following link:
https://www.youtube.com/playlist?list=PLm0c-zXrCqEIhUCgaYxDt1nFt3fEGg1Wf

Chapter 4

Extension of the FSI approach for the mechanical valve with validation

The model described in Chapter 3 was extended, as the valve motion was calculated. The flow mechanics through an artificial bileaflet mechanical valve was investigated using in-house 6DOF model with the novel adaptive timestepping method. Ansys® Fluent finite volume solver was used here and two different moving mesh strategies were adopted and used: overset mesh and three different options of dynamic mesh, to absorb the valve motion in the numerical mesh. The moving mesh modules were compared, towards differences between results of models using them, their validity, susceptibility to errors, and utility. This comparison was not previously investigated for mechanical valves in the literature. The results were compared with the measurement data obtained using an internal test rig with pressure and flow meters, a fast camera and a prepared own LabView® control application. Fast camera images were processed for leaflet angle reading using Python OpenCV [127], which is currently a novel approach in terms of artificial valve measurements. The 6DOF model sensitivity to the moment of inertia error was quantified via performing a series of numerical simulations, which currently were not found in the literature - all research considered a single inertial moment value. In addition, a novel approach for adaptive timestepping was developed and utilized, which allowed it to decrease the demanded computational time substantially and avoid moving mesh errors.

The angular velocities are calculated using 6DOF model. The leaflets are moving in

the fluid domain using macro `define_cg_motion` and this motion is absorbed by the moving mesh module. The model works using text files, created by Fluent journals and UDFs. Part of these files have to be empty at the end of the step, which is realized by UDF `define_at_end`.

During the first 80 timesteps, the angular velocity is linearly ramped against the function of timestep number: $\omega_n = \omega_n \cdot (0.00125 \cdot n\_time)$, where *n_time* is the integer number of timestep. This was added to start the rotation more slowly, only at the beginning of the computation, when the velocity field is not yet fully developed and thus is harder to resolve. A small number of large force moments higher by orders of magnitude was experienced, in this case they were treated as gross errors by adding to the UDF's conditional statements that discard these kinds of values. As the leaflets can rotate in the specified angular range, an additional module was added that suppresses the rotation when the maximum or minimum allowable angle is achieved. The rotation is unblocked when the force moment takes the opposite sign, which promotes the rotation in the opposite direction.

For the better computational stability at the beginning of the first cycle, the computation starts from the valve at the slightly opened state - with the leaflets rotated by 20° from the closed position. The angular state at any moment is not known a priori , so several heart cycles were calculated for every set of boundary conditions, until fully repeatable results were achieved.

4.1 Geometry and numerical mesh

The overset mesh technology was applied. The same geometry of the bileaflet valve component was used, as in Chapter 3. The three-dimensional background geometry prepared for the numerical model is simply a tube, representing the frame where the valve was fastened and the fragment of the test rig pipe (Fig. 4.1). The inner diameter was equal 1.7 cm. The pipe length after the valve location, equal 5.75 cm, is corresponding to the location of the 2nd pressure sensor. The length before the valve (13.4 cm) was used as shorter than the valve distance to the flow meter section, as it was investigated, by a series of simulations, that the limitation of this length does not influ-

ence the results. This is caused by the fact that the test rig tubes are non-deformable, so pressure wave propagation does not occur, and the used length is already sufficient to realize a hydraulic run. The location of the valve in the pipe can be observed in Fig. 4.1.

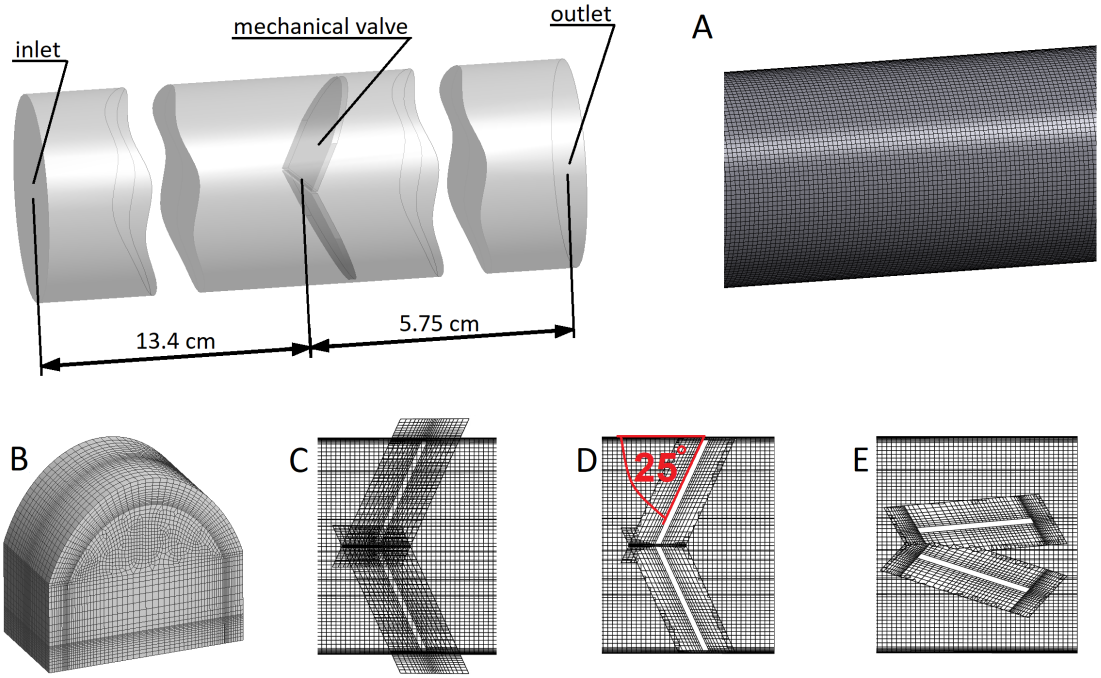

Figure 4.1: Numerical mesh prepared for the overset approach: **A** - geometry and fragment of the background mesh, **B** - component mesh, **C, D, E** - cross-sections through the joined background and component meshes: **C** - before matching process, **D** - after matching process, **E** - after matching process (opened state)

The overset background mesh was prepared as discretized pipe geometry using swept hexahedral cells with the 7-layer inflated prism boundary, with smooth cell size transition between the boundary and inner mesh. This was set to better resolve the boundary layer and to ensure proper number of cells across the gap, for avoiding orphan cells when the valve is closed.

To check the influence of domain discretization on the predicted results, a mesh sensitivity analysis was performed on three different meshes. Firstly, the connectivity of the overset mesh was tested with the entire leaflet angle range using UDF `define_cg_motion`. The corresponding background and component mesh settings and densities were adjusted until the orphan cells were not present at any leaflets' position. Three different mesh types were prepared for the sensitivity analysis: *coarse*

(background 881,000 cells, component 31,000 cells), *medium* (background 1,850,000 cells, component 55,000 cells) and *fine* (background 2,300,000 cells, component 94,000 cells). The leaflet motion and velocity values were compared for different meshes. Finally, the conclusion was made that further decreasing in cell size does not influence the results and the *medium* type was chosen for the analysis.

4.2 The boundary conditions

The prepared 6DOF model can operate with any possible boundary condition applied. In this research, to properly represent the mass flow and pressure levels, the inlet velocity and the outlet pressure boundary conditions were used. The time-varying values were simulated using measurement data, via the use of several approximation polynomials for each measurement set. The use of multiple polynomials allowed a better representation of the measurement data, where the coefficient of determination was on the level of 99%. The substance used in the model is water, as in the test rig. The properties were set: density 998.2 kg/m^3 and dynamic viscosity 0.001003 kg/(m·s). The $k-\varepsilon$ turbulence model was selected, based on the research conducted in Chapter 3.

4.3 Laboratory test rig and measurements

During the experimental investigations at in-house test-rig illustrated in 4.2, a bileaflet artificial heart valve was tested. The polycarbonate valve holder is connected to the Pulsating Blood Pump (Harvard Apparatus®). The pump has the possibility to change the heart rate and the percentage difference between the volume of the systolic and diastolic strokes, as well as the size of the ejection chamber. The electromagnetic flow meter, Enderess + Häuser, Promag 100 [128] was used to measure the flow rate through the investigated valve. Selected flow meter does not generate pressure loss and, due to frequency output, it was possible to acquire flow profile with desired accuracy to use it for further numerical model setup.

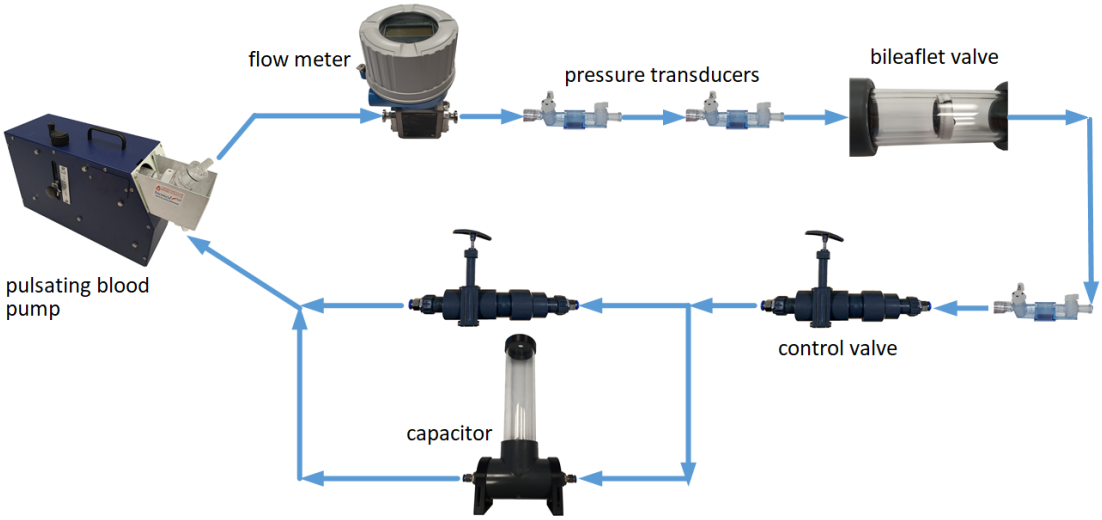

Figure 4.2: Configuration of the laboratory test rig

For measurement of pressure profile during the pump cycle, four fast static pressure sensors (APT 300 – sapling rate: 1 kHz) were used as shown in Fig. 4.3 A. An additional pressure sensor was placed 26 cm before the valve. The information collected from these locations as well as from the flow meter was necessary for a proper initialization of the numerical simulations.

To capture the movements of the valve leaflets, a high-speed camera VEO 710L [129] was equipped with a NIKKOR 200 mm F/4.0 MACRO lens. This configuration allowed the tracking of leaflets movement at a resolution of 1280 x 800 pixels and a rate of 9,800 frames per second. To ensure sufficient illumination for the camera, a backlight (LED Phlox HSC Phantom 10 x 10 cm) was used with a luminance of $\geq$130.000 cd/m^2, uniformity of $\geq$ 95%, and light temperature of 5,700 K. An example of a recorded image is shown in Fig. 4.3A.

The installation was controlled by an in-house application written in National Instrument LabVIEW (National Instruments Corp., USA) [130] to synchronize the measurements with the pump cycle and camera. To capture flow rate through the rig the LabVIEW FPGA was used for efficient and effective control complex systems by application of a highly integrated development environment. All experimental results were stored in ASCI format for future processing.

In the laboratory test-rig, the vertical tube capacitors were used to maintain the con-

stant pressure levels in the measurement system. They were used as the representation of the last part of the circulatory system of human beings [131, 132]. In terms of the human body, they account for the interaction between stroke volume and the compliance of the aorta and large elastic arteries (Windkessel vessels) and the resistance of the smaller arteries and arterioles. In conclusion, distensibility of the aorta and large elastic arteries is therefore analogous to a capacitors used.

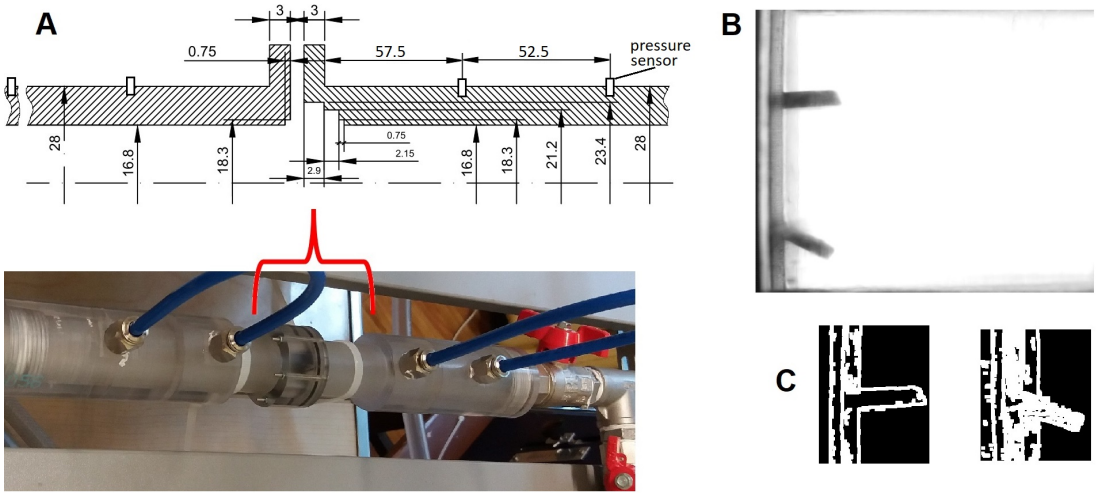

Figure 4.3: Designed aortic valve holder with marked dimensions (**A**); fast camera image (**B**); upper and lower leaflets camera image fragments, after OpenCV processing (**C**)

Measurements were performed for five different conditions, resulting from different heart pump settings by adjusting: pump rates, stroke volume, and stroke volume division between systole and diastole as collected in table 4.1. Therefore, different velocities and pressure levels were achieved, as well as cycle times, as shown in Fig. 4.4. The numerical model was tested and validated on the basis of every data set. The model constant - moment of inertia - was calibrated based on the 5^{th} dataset, then using the four remaining ones the calculations were performed and validated, to assess its reliability under different flow conditions. The choice of the 5^{th} dataset for calibration was based on the pump settings closest to the applied average.

Dataset no.	systole:diastole % : %	pump rate RPM	volume, cm^3	cycle time, s
1^{st}	30:70	50	80	1.20
2^{nd}	30:70	60	80	1.02
3^{rd}	30:70	70	80	0.84
4^{th}	35:65	60	80	1.02
5^{th}	40:60	60	80	0.98

Table 4.1: Heart pump setpoints applied to measurement sets

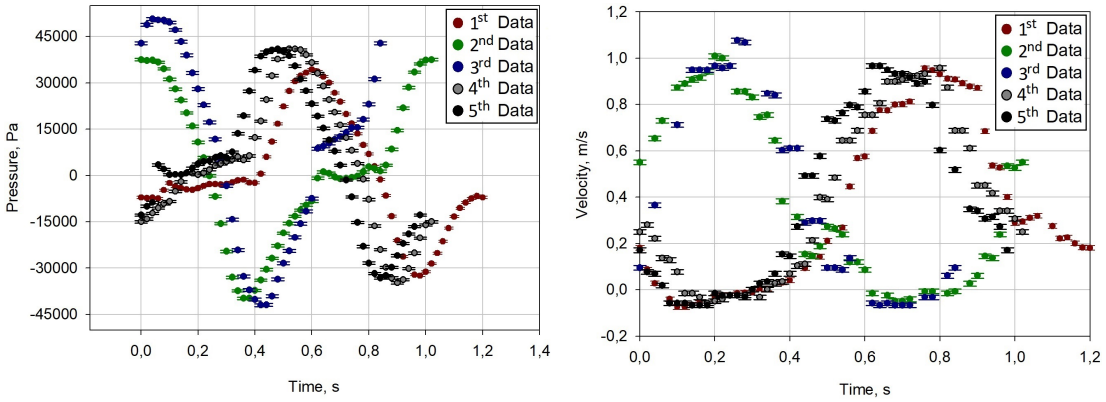

Figure 4.4: Measurement data provided for the numerical model boundary conditions, presented for five datasets

4.4 Extraction of the leaflet angles

The fast camera greyscale images registered during the test rig measurements were used to validate the numerical model results in terms of leaflets' angular motion. Thus, these images have to be processed into the values of the leaflets' angle. The procedure for angle determination was created in Python OpenCV environment.

The analysis of images is present in many different fields. It is used in everyday situations, such as face or fingerprint recognition, to complex algorithms utilizing machine learning tools [133]. Its applications take place among others in automatic inspections, manufacturing, controlling processes, navigation, medical examinations, object detection, motion detection, robotics, and security systems. The visual and manual inspection is highly inefficient, time-consuming, non-replicable and inaccurate. Thus, nowadays many different imaging techniques and software tools are developed in the field of computer vision - the computer algorithms for high-level and automatic processing of images and videos. The most common modules can be found in [134]. For the purpose of processing the images registered at the test rig, the program was prepared using the OpenCv library. OpenCV is one of the most popular image libraries, originally developed in 1999 by the Intel Corporation [135]. Is is applicable in many programming languages, as Python, C, C++, Java, MATLAB, SciLab, from which the Python was chosen, as it corresponds well with the popular NUMPY and PANDAS matrix libraries, is regularly updated and supplies many state-of-the-art algorithms.

In the algorithm prepared, it was necessary to transform parts of grayscale images into binary format, where the number *0* is referred to black and the number *1* to white color. The typical conversion to binary itself, as in previous work [27] worked well, however, the Canny operation was chosen over the binary conversion [136]. The reason is that this allowed for better identification of the edges of the leaflets. The Canny algorithm is the popular multistep edge detection technique. It consists of Gauss filtering, gradient calculation, non-maximum suppression, double thresholding, checking the edges and connecting the edges [137]. It was invented by John F. Canny in 1986 [138].

The first step of the Canny algorithm is to remove the noise in the image with a 5x5 Gaussian filter, as the edge detection is susceptible to the image noise [136].

Afterwards, the smoothened image is filtered with a Sobel kernel in horizontal (x) and vertical (y) direction, to find the first derivatives G_x and G_y. Different kernels based on finite differences can be used. After finding the gradients, the direction θ for each pixel is calculated:

$$\theta = \tan^{-1} \frac{G_y}{G_x} \tag{4.1}$$

This gradient direction is always perpendicular to the edges. To reflect the intensity of the edge in the pixel *(i,j)*, the magnitude of the gradient $M_{i,j}$ is also calculated as follows:

$$\begin{gathered} M_{i,j} = \sqrt{L_x^2(i,j) + L_y^2(i,j)} \\ where \quad L_x = \frac{\partial G}{\partial x} \cdot \varphi(x,y) \quad and \quad L_y = \frac{\partial G}{\partial y} \cdot \varphi(x,y) \end{gathered} \tag{4.2}$$

The function noted G in eq. (4.2) is the two-dimensional Gaussian function

$$G(x,y) = \frac{1}{2\pi\sigma^2} \cdot exp\left(-\frac{x^2+y^2}{2\sigma^2}\right) \tag{4.3}$$

and $\varphi(x,y)$ is the original image matrix.

Afterwards, the image is scanned to suppress unwanted pixels around the edges. Finally, the stage called *hysteresis thresholding* is done to decide which edges should be discarded, based on the maximum (THR_{max}) and minimum (THR_{min}) threshold values. The edges with a gradient magnitude greater than THR_{max} are saved, whereas those less than THR_{min} are discarded. The ones that lie between the threshold values are judged based on their connectivity. The threshold values should be based on trials and may differ a lot for the specific pictures. In this research, the values $THR_{min} = 25$ and $THR_{max} = 50$ worked well.

The algorithm developed for automatic determination of the leaflet angle was devided into several steps. First, the fast camera image is loaded and the fragments where the upper valve leaflet is visible (in previously defined coordinates) are cut. Similar procedure is repeated for the lower leaflet. Described procedure is done for all the pictures from the fast camera folder. Afterwards, the cutted images are loaded and the Canny operation is performed, to extract the leaflet edges and make them white, for easier identification (see Fig. 4.3). These edges are then thickened with the *dilate* operation, to facilitate the processing of images that may be blurred. The procedure

is searching for the first white pixel, starting from the upper right corner (for upper leaflet) and lower right corner (for lower leaflet). In this way, the coordinates of the ending of both leaflets are found. The last step is the calculation of the arcus tangens of the slope of straight line, which is created between two points: ending of the leaflet and its center of rotation. This way the angles of both leaflets are determined. The centers of rotation were found by overlaying several images, where the valve was in different positions. The leaflet edges were extended to find the point where extensions intersect each other, then the point coordinates were read out. Described here algorithm can be found in Appendix A.

4.5 Model results

4.5.1 Dynamic timestep size sensitivity analysis

The timestep size for time intervals where leaflets are moving, is calculated using eq. (2.25). Thus, excessive mesh distortion is avoided by time-discrete adaptation. For stationary leaflets, fixed value of $\Delta\tau_n = 0.001\ s$ was applied. The model constant in eqs. (2.25) - $\Delta\theta_{max}$, describes the maximum allowable angular displacement per single timestep, and affects directly the computational time. The timestep size sensitivity analysis was performed on the fifth dataset, using different values of $\Delta\theta_{max}$. This was done to check how the number of timesteps increases by lowering this value, to check whether it impacts onto numerical model results and also to assess the moving mesh operation. The results are presented in Fig. 4.5 and Tab. 4.2. The number of timesteps per heart cycle decreases rapidly up to the value of $\Delta\theta_{max} = 0.2^\circ/\Delta\tau_n$, then the change becomes inconsiderable. After increasing the allowable angular displecement to 0.5 degree per timestep, the model could not be resolved due to the orphan cells.

The computational saving was calculated by comparing $\Delta\tau$ per cycle, with the number of time steps that will be necessary to ensure that the $\Delta\theta_{max}$ is applied with the constant time step:

$$solv_{red} = \frac{n_{\Delta\tau\_dyn}}{n_{\Delta\tau\_const}} \cdot 100\% = \frac{n_{\Delta\tau\_dyn}}{\frac{cycle\ time}{\Delta\tau_{min}}} \cdot 100\% \tag{4.4}$$

where $solv_{red}$ is the solving time reduction, $n_{\Delta\tau\_dyn}$ - number of timesteps resulted from applied time discretization methodology, $n_{\Delta\tau\_const}$ - number of timesteps for constant time discretization, $\Delta\tau_{min}$ - minimum timestep size (which occured during the fastest angular velocity).

The computational savings is highest for the lowest angular displacement per timestep and decreases linearly with increasing $\Delta\theta_{max}$. The angular time variations of the leaflets, as well as pressure values, were compared for different $\Delta\theta_{max}$. The conclusion was made that for the considered time discretizations, the results are independent. Possibly, applying the highest maximum timestep, some flow-field characteristics would differ, however, this was not necessary due to time-efficient time discretization.

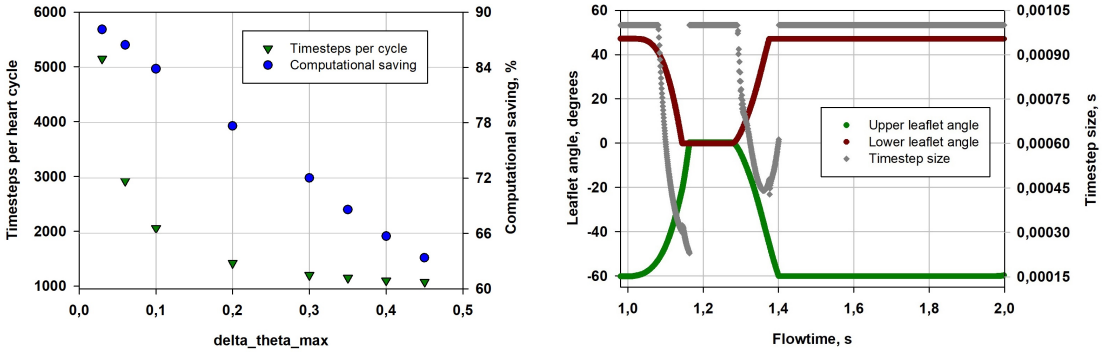

Figure 4.5: **Left:**Timestep size sensitivity analysis, based on the change of model constant $\Delta\theta_{max}$; **Right:** results obtained for the selected value $\Delta\theta_{max} = 0.3^{\circ}/ts$ - leaflet angle profiles with variable timestep size

Taking into account the described remarks, the model constant of $\Delta\theta_{max} = 0.3^{\circ}/ts$ was used, mainly due to the inconsiderable reduction in time steps with higher $\Delta\theta_{max}$, and to avoid eventual orphan cells. The final time angle profile of the leaflet with the time step size plotted is presented in Fig. 4.5. The angle of 0° is referred to the closed state. As observed, the value depends on the angular velocity (i.e., angle curve slope), which changes smoothly during valve motion.

No.	$\Delta\theta_{max}$, deg/ts	$\Delta\tau$ per cycle, ts/cycle	$\Delta\tau_{min}$, s	$\frac{cycle\ time}{\Delta\tau_{min}}$, -	computational saving, %
1	0.03	5 149	0.000 023	43 257	88%
2	0.06	2 916	0.000 046	21 493	86%
3	0.10	2 054	0.000 077	12 710	84%
4	0.20	1 417	0.000 155	6 335	78%
5	0.30	1 198	0.000 229	4 278	72%
6	0.35	1 148	0.000 268	3 653	69%
7	0.40	1 100	0.000 306	3 205	66%
7	0.45	1 072	0.000 335	2 924	63%
9	0.50	unconverged results			

Table 4.2: Dynamic timestep size sensitivity analysis indicators

4.5.2 Moment of inertia multivariant analysis

The usage of 6DOF model in this case could be restricted to only one rotation around the z axis. The proper momentum of inertia has to be calculated. This quantity determines how large the rotational force should be, to achieve specified angular acceleration around the rotational axis [139]. Here, only one of the nine components of the inertial tensor is demanded: $I = I_{zz} = \int \left(x^2 + y^2\right) dm$. According to this equation, the value depends on the chosen axis, body mass, and its distribution.

Several different ways are available to determine the moment of inertia. Sometimes the value can be measured using the rotary disc. For the simpler geometrical features, analytical formulas are possible. For example, the valve leaflet could be estimated as the half disc with radius R, whose value calculated against the edge of the half disc is equal to $I = 0.25 \cdot m \cdot R^2$. As the inertial moment is an additive property, the composite system is the sum of the moments of inertia of its component subsystems, only if the same axis is considered. Thus, the computer software products can be used for any complex geometrical features, to calculate the momentum of inertia, virtually dividing the geometry into simpler shapes. Due to the geometrical character of more complex leaflets and the location of the rotational axis, the SpaceClaim software mass tools were utilized [140]. In this way, the inertial moment value divided by the density could be found, with the rotational axis coincident with the center of gravity. This is called

principal moment [mm^2] [59, 139]. To ensure that the software used calculates proper values, several cases where analytical solutions are available were prepared and almost the same results as analytical. Then, the mean leaflet density was calculated. Is is made from pyrolytic carbon ($\rho = 1\,940\ kg/m^3$) and coated by tungsten ($\rho = 19\,300\ kg/m^3$) in 20% by weight [10, 141]. The below set of equations:

$$\begin{aligned} m_t &= 0.2 \cdot m_l \\ m_l = m_W + m_C &= V_W \cdot \rho_{\mathrm{W}} + V_{\mathrm{C}} \cdot \rho_C \\ V_l &= V_W + V_C \end{aligned} \tag{4.5}$$

where m is the mass, V defines the volume, ρ stands for density, C refers to pyrolytic carbon, W stands for tungsten, and l is the leaflet, gives the possibility to calculate the mean density of the leaflet, equal $\rho_l = m_l/V_l = 2365.6$ kg/m^3. Then the value of the principal moment from SpaceClaim was multiplied by the calculated density and the principal inertial moment was obtained: $I_0 = 2.62 \cdot 10^{-9}$ kg·m^2. However, it was determined that the rotational axis is in the position located 15% of the valve radius from the vessel centerline (Fig. 4.1D, E). Thus, Steiner's law for parallel axes was used to transform the calculated moment to the proper axis [102]

$$I_{\mathrm{geom}} = I_0 + m \cdot d^2 \tag{4.6}$$

where I_0 is the moment of inertia with respect to the axis passing through the center of mass, m is the mass of the body and d is the distance between the two axes. Finally, the value $I_{\mathrm{geom}} = 3.5331 \cdot 10^{-9}$ kg $\cdot$ m^2 was obtained. However, valve motion is influenced by factors that slow the motion, extend beyond rotational inertia, and are not easily calculated or measured. These factors are, e.g., friction of the mechanism, small particle deposition, impurities in the laboratory test rig, water settling on the valve, and non-uniformity of leaflet mass distribution. Furthermore, different values of I were noticed in other works, depending on the inner diameter size and the density of the leaflet material assumed or calculated (compare: [142] $8.75 \cdot 10^{-9}$ kg $\cdot$ m^2, [143] $7.947 \cdot 10^{-9}$ kg $\cdot$ m^2, [144] $3.99 \cdot 10^{-9}$ kg $\cdot$ m^2, [145] $6.95 \cdot 10^{-9}$ kg $\cdot$ m^2). Therefore,

faster rotations were determined than observed in the test rig.

To find the proper I constant that includes all the factors that influence motion, the calculated value was magnified with different multipliers $n > 1$: $I = n \cdot I_{\text{geom}}$ until the differences between the measurement data and the numerical model were minimized. To assess these differences, the function **F** (e.q., (4.7)) was prepared. It was based on calculating the area under the leaflet angle courses, for the angles that are visible in the fast camera field of view, for every stage: opening, opened valve, closing, closed valve−see Fig. 4.6A. The base area A_{meas} was calculated using the fast camera data.

$$F(n) = \frac{A_{6DOF}(n)}{A_{\text{meas}}(n)} = \frac{A^{c.u.}_{6DOF}(n) + A^{o.u.}_{6DOF}(n) + A^{c.l.}_{6DOF}(n) + A^{o.l.}_{6DOF}(n)}{A^{c.u.}_{\text{meas}}(n) + A^{o.u.}_{\text{meas}}(n) + A^{c.l.}_{\text{meas}}(n) + A^{o.l.}_{\text{meas}}(n)} \tag{4.7}$$

where $c.$ - closing, $o.$ - opening, $u.$ - upper leaflet, $l.$ - lower leaflet

By considering the areas under time angle course, it was possible to analyze the model differences in the motion in the whole spectrum that leaflets were visible at camera. If the function was based, e.g., on the times between certain angular states, it would omit the motion profile.

The calculation of 43 cases with different inertia multipliers was performed in the scope $2 \leq n \leq 7$. To obtain the results of the model as close to the measurement as possible, the multiplier n should be chosen for which function F has a value of 1. Results of the multivariant analysis are presented in Fig. 4.6 - the variance of the function F together with the angle-time courses. The 6DOF model was stated to be quite sensitive in the multiplier scope $2.0 \leq n \leq 2.7$, then up to the maximum analyzed value of the function 7 F changes slowly and linearly. It is also apparent that when angle time variations are compared, the angular course between $m = 3$ and $m = 7$ differs much less than between $m = 2$ and $m = 3$. In the multiplier range $< 2.75; 3.5 >$ the results remain almost the same. Thus, the average value in this scope $n = 3.125$ was finally chosen, as the model results are very close to the measurement (F value close to 1.0) and the model is not sensitive to the errors (upper error and lower error) of determination of inertial moment:

$$I = n \cdot I_{\text{geom}} = 3.125 \cdot 3.5331 \cdot 10^{-9}\,\text{kg} \cdot \text{m}^2 = 1.1041 \cdot 10^{-8}\,\text{kg} \cdot \text{m}^2 \tag{4.8}$$

The multiplier n was chosen based on calculations performed using the fifth dataset. Then, the remaining four data sets were calculated with the same moment of inertia I, where similar results validity should be expected.

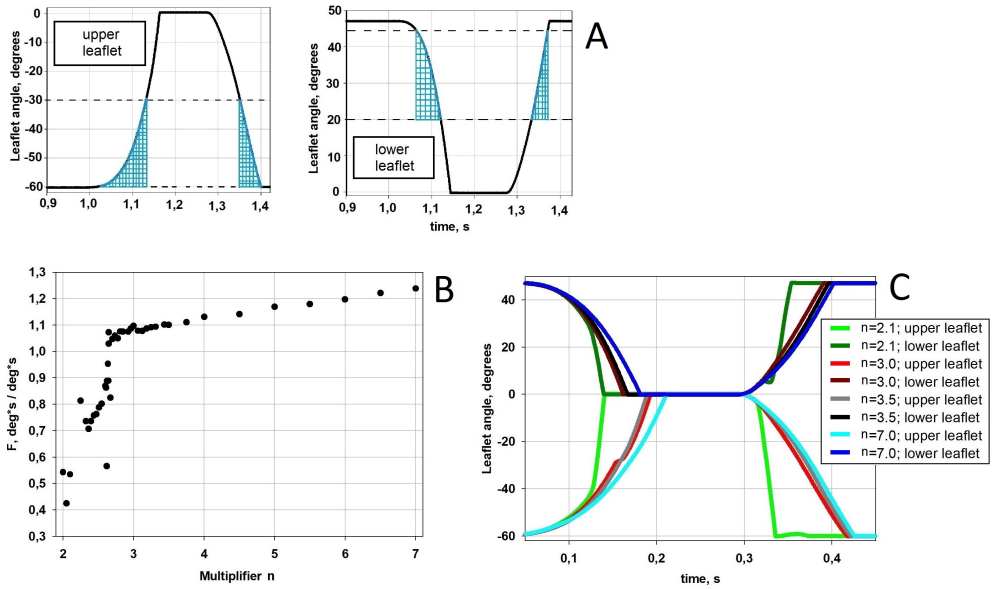

Figure 4.6: Multivariant analysis: **A** - procedure of integral determination for function F; **B** - function values for different magnifications m of the geometrical moment of intertia; **C** - leaflet angle courses for different m values

When the moment of inertia is changed, the variability of the results presented in Fig. 4.6 comes from several reasons. First, the higher inertial moment promotes slower leaflet angular velocities, which is straightforward from Eq. (2.28). However, the values of ω do not change linearly with I, as the equations suggest. This comes from obtaining different moments of force M_{n-1}, which results from the changed angle of incidence. For example, during the closing phase, when the moment of inertia is lowered, the rotation calculated from eq. (2.28) is faster and thus the angular position is nearer to the closed state. Thus, the fluid hits the leaflet more perpendicularly, which promotes greater forces and greater force moments. This also promotes even faster rotations. The additional factor that affects the calculated valve motion for the changed inertial moment is the fact that the inflow profile is fixed as a boundary condition. Thus, the inlet velocity profile corresponds to different leaflets' angular positions, when the moment of inertia is changed. This causes the production of other force moment values

for the same inlet velocity.

4.5.3 Transient leaflet angle results

As described in Sec. 4.5.2, the correction of the model constant - inertial moment I - was performed on the fifth dataset. To verify the validity of the model, four other measurement sets with different flow conditions were performed and solved within the prepared 6DOF model using the same corrected I. As the leaflets motion resistance is independent from the flow condition, the same results' validity should be present for both calibration set and validation sets.

The results are presented in Fig. 4.7 and Fig. 4.8. The uncertainties for the error bars were calculated by checking the times for which several angles (maximum visible, medium, minimum visible) are achieved. This was done for at least eight heart cycles, because this was the minimum number of cycles captured for every dataset on the fast camera. Subsequently, the standard deviations were calculated. It is worth adding here, that very high repeatability of registered leaflets' angle coursed and fluid pressures was achieved.

Figures present the validity of the calculated leaflet angles for three cycles. As expected, the first heart cycle does not coincide with the validation data, because the proper valve starting position at the beginning of the simulation is unknown, thus it is always necessary to solve more than one cycle. The results for the second and third cycle are the same, so calculating two heart cycles is sufficient to ensure the repeatability of the results.

The simulation results present satisfactionary validity with the measurement data for every dataset. The level of validity does not differ between the momentum of inertia calibration (5^{th} data) and four remaining sets. Some minor differences in angle courses between the numerical model and measurement are observed for the lower leaflet, however they generally lay within the scope of one standard deviation. Also, very good validity of the opened state time and extrapolated closed state time is observed, and the moments where leaflets starts moving coincide well. One of the probable reasons for the differences is a sampling time for the inflow measurement equal to $0.02\ s$ resulting from the abilities of the device. This time is quite large, comparing that

the time necessary to turn from fully closed to fully opened valve state (or reversely) is on the level of $0.1s$. It was stated that the inflow profile measurement accuracy is more important for the numerical model' time angle reliability, than the pressure measurement (see Sec. 4.5.5). Also, the uncertainty quantification for the model planned for future work will assess which parameters play the key role in the validity of the model [146].

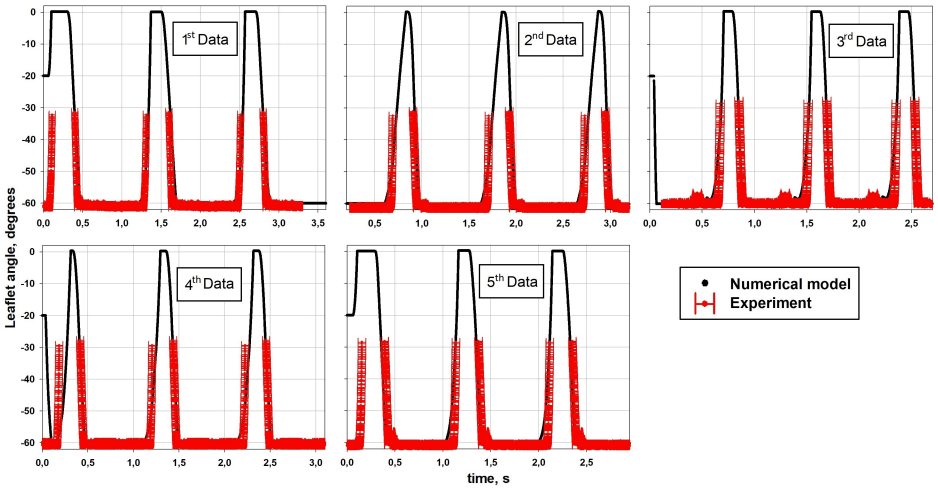

Figure 4.7: Comparison of the upper leaflet, between the measurement data and the numerical model, for three calculated cycles. Results are presented for five datasets. Angle 0°refers to the closed state, and -60°- opened state

The inertial moment for the 6DOF model was set as the same value, both for the upper and lower leaflet. This may be the reason why the angular courses deviates from the measurement data slightly more for the lower than upper leaflet. Possibly, factors slowing the motion, which extend beyond body inertia, such as mechanism friction and suspended deposition impurities are higher in the lower leaflet in the analyzed case. Performing multivariant analyzis of the inertial moment with allowed different multiplier values for both leaflets may let to obtain even better consistence with fast camera data. However, it was not needed as the validity was stated as satisfactory, and this will lead to increase the number of cases with a square. Moreover investigating the multivariant analysis for the multipliers dependent on the leaflets angle will increase the number of cases even more. Thus, a single constant value for the inertial moment was used.

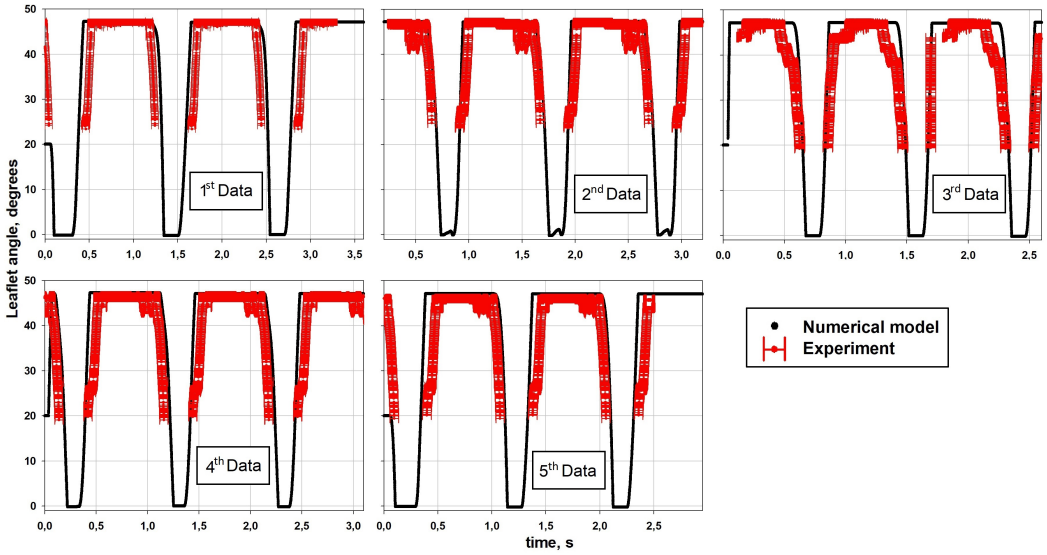

Figure 4.8: Comparison of the lower leaflet angle variation, between the measurement data and numerical model, for calculated three cycles. The results are presented for five datasets. Angle 0°refers to the closed state, 47°- opened state

4.5.4 Pressure validation

Validation of the pressure values between the valve location is presented in Fig. 4.9. Comparison between the numerical and experimental pressure results was peformed for all datasets presented in Tab. 4.1. The numerical results are presented for the second calculated cycle. The numerical model was stated to have good agreement with the measurement of the test rig also in terms of the pressure values. Some inconsistency was stated at the time when the leaflets are moving (compare Sec. **??**). This regularity is observed in all datasets and may be caused both by the measurement and model errors. When the valve is moving, especially with fast angular velocity, the pressure is rapidly changing, thus it may be harder to measure (notice the gross measurement errors) and calculate its value properly. Also, the pressure in the valve vicinity is highly dependent on the leaflets' angular position; thus, even small angular inconsistency with the measurement data may cause visible discrepancies. However, during most of the heart cycles, the measured profiles coincide in the range of error bars.

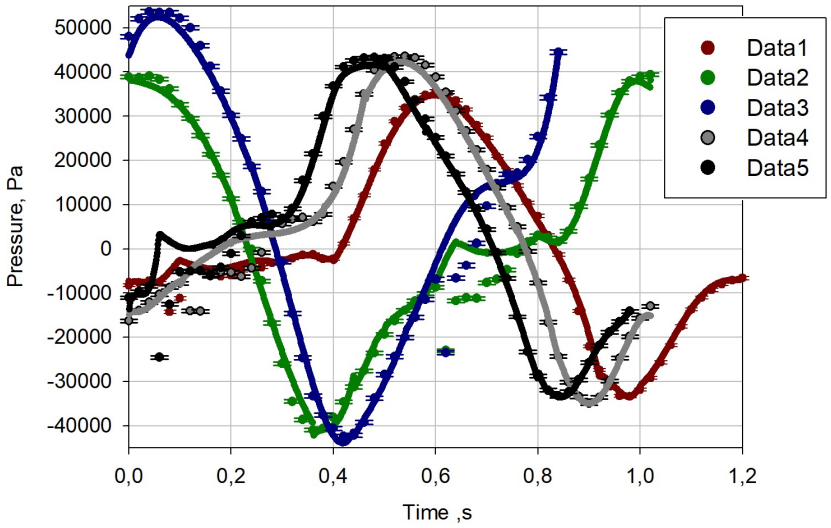

Figure 4.9: Validation of the pressure values in place between the valve. Results are presented for five datasets, the measurement is represented by points with errorbars, the numerical results are shown as continuous lines

4.5.5 Simplified model results

Comparative analysis was performed for the model, where only the velocity time profile is introduced for the boundary condition. The outlet section was elongated by 50 mm and the 0 Pascal gauge pressure boundary condition was prescribed for the outlet. The model was solved for the 3rd and 4th datasets. The conclusion was made that leaflet motion is governed primarily by the inflow boundary condition - the outlet pressure values do not have a substantial impact on the valve motion - Fig. 4.10. However, when comparing the values of the pressure exerted on the leaflets, it was stated that the model with 0 Pa constant outlet pressure lowers the leaflet pressure by an order of magnitude. Thus, for a reliable estimate of the valve characteristics, it is necessary to also put the information of the outlet pressure profile in the numerical model, in addition to the inflow profile.

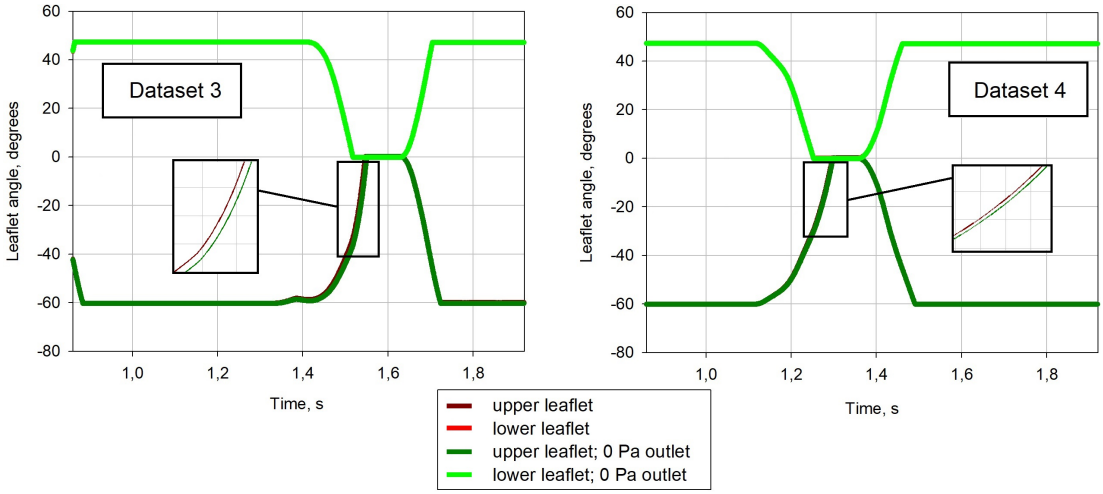

Figure 4.10: Comparison of the time leaflets angle profiles, for the model including and excluding the outlet pressure variation in the input data

4.5.6 Results comparison with dynamic mesh approach

The model results involving the overset moving mesh method were compared with other moving mesh approach - dynamic mesh. This demanded creation of new geometry discretization, which final form is shown in Fig. 4.11. The dynamic mesh was prepared and solved based on 3rd dataset. This technique is based on two modules: remeshing and smoothing. The smoothing method moves the internal mesh nodes to absorb the motion. When cell quality characteristics extend beyond the acceptable defined values, the cells are locally remeshed, preparing a new tetrahedral mesh. To prepare the geometry for this moving mesh approach, the lefleat geometries were subtracted from the pipe geometry. The new discretization for dynamic mesh was prepared based on the element size and the number of boundary layer settings chosen based on the overset mesh sensitivity analysis. Thus, *medium mesh* settings were applied. The modification for this moving mesh approach was to prepare the tetrahedral mesh in the surrounding valve, instead of the hexahedral swept mesh (Fig. 4.11). This was done to allow a remeshing process. The hybrid mesh consisted of 1,200,000 mln of mixed tetrahedral+prism elements (valve region) and 0.76 mln of mixed hexahedral+prism elements (remaining parts).

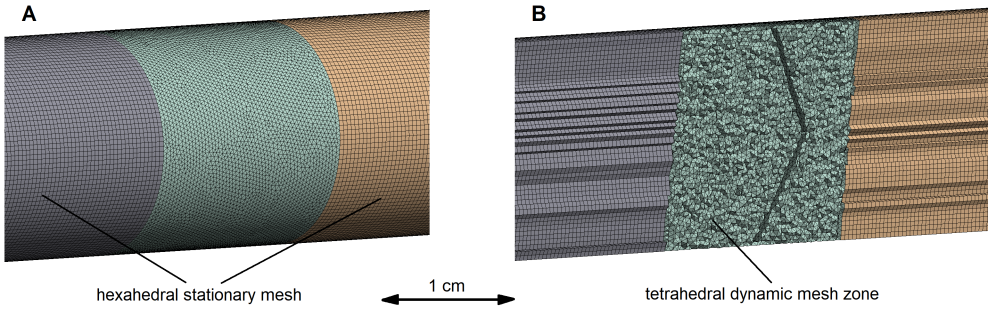

Figure 4.11: Hybrid mesh prepared for the dynamic mesh approach: **A** - outer mesh, **B** - cross-section through domain

Three different approaches were used here: 1st - remeshing+diffusion smoothing; 2nd - remeshing+spring smoothing; 3rd - remeshing only, where the mesh was used without the boundary prism layer. The dynamic mesh model calibration was primarily set by setting the maximum and minimum allowable element size, the acceptable cell skewness limit, and the smoothing parameters which depend on how far from the moving body the mesh absorbs its motion. These settings are very case-dependent, where not only geometry, but also motion characteristics play its role. Much effort was demanded to prepare proper settings, which allow both to avoid the negative cell volume error and prepare high-quality cells with proper density. The prepared mesh in the valve vicinity is shown in Fig. 4.12. Outside the geometry region shown in picture, the hexahedral mesh was used as the one prepared for the overset method. Observed smoothing' layer compression and stretching allows for good-quality cells to remain, avoid negative cell volumes, and remain proper densification in high-gradient regions.

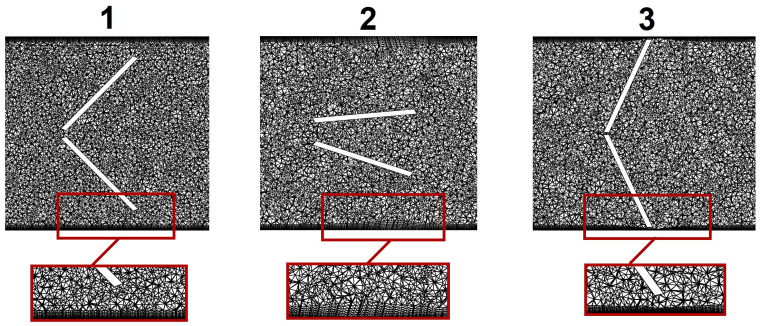

Figure 4.12: Cross-section of the mesh prepared for the dynamic mesh approach: 1 - the initial mesh, 2 - the opened valve state with stretched boundary layer, 3 - the closed valve state with compressed boundary layer.

Overset mesh approach significantly improved the computational stability and solver convergence due to the avoidance of generation of some low-quality cells in the gap vicinity (presented in Fig. 2.1 and Fig. 2.2), in the case of dynamic mesh usage instead. Moreover, it enabled the creation and preservation of the hexahedron structural mesh during body movement in the majority of the two individual leaflet surroundings and in the background as well, which improved the boundary layer resolving. An additional advantage of the overset meshing is the limitation of the solver wall-clock time, because this utility is less consuming than smoothing or remeshing, and eliminates the negative cell volume error. This error will stop the solution process. Furthermore, the dynamic mesh could deteriorate the cell quality, especially by increasing the skewness parameter. Maintaining high-quality cells, especially near moving or deforming bodies, is crucial to improve accuracy and stability in the simulation.

Two different approaches used for the moving mesh, i.e. overset and dynamic mesh, differs with their applicability and preparation process. The overset mesh method demands multiple tests on the components and background mesh settings during their creation, whereas preparing discretization for dynamic mesh could be done only once, but different settings in the numerical solver have to be tested for dynamic mesh modules. In the overset mesh method, a higher maximum leaflet rotation of $\Delta\theta_{\max} = 0.45^{\circ}/\text{ts}$ was allowed to avoid the orphan cells and properly solve the model, where in dynamic mesh the value equal $\Delta\theta_{\max} = 0.3^{\circ}/\text{ts}$ did not allow to avoid negative cell volume error, no matter what settings for mesh motion were applied. Thus, $\Delta\theta_{\max} = 0.075^{\circ}/\text{ts}$ for dynamic mesh timestep size constant was set and used to solve the model with dynamic mesh method, which implied greater solving time. When in the overset approach several orphan cells appeared, the solving process was not affected and residuals represented satisfactory values. In the case of the dynamic mesh, the single cell with negative volume caused solving termination with no possibility of restarting the calculation. The dynamic mesh method provides conservative calculations, where overset mesh is based on data interpolation between the background and component meshes. However, interpolation is not a problem in the case where a convergent solution is achieved [59].

Similar mesh motion patterns were obtained for the diffusion and spring smoothing. The dynamic mesh method is more error-prone, because during its settings calibration, negative cell volume appeared more often, than orphan cells during the overset mesh calibration. Moreover, it was not possible to calculate three heart cycles using 2nd dynamic mesh approach due to the negative cells, however it was stated that two cycles are sufficient to achieve result repeatibility. Furthermore, higher acceptable rotations in the case of the overset method entail computational saving (See Fig. 4.5 and Tab. 4.2). Thus, it seems more reasonable to use the overset meshing, especially within simulations involving multivariant analyses. For the dynamic mesh, the number of cells changes with the subsequent timesteps. This change may be substantial, if the settings related to the maximum and minimum allowable element size are not proper. For the overset mesh - number of elements remain almost constant - only during the closed valve state some parts of the component bodies exceed the background geometry, which leads to a slight limitation in the number of solve cells.

Similar results were obtained from both moving mesh methods, as shown in Fig. 4.13. The differences possibly come from the necessity of producing a new mesh during every timestep, where the motion is present, and the presence of tetrahedras in the valve region for the dynamic mesh. In the case of the overset method, constant meshes are present, only the donor-receptor pairs changes with motion. The highest differences were noticed in the model, where remeshing was used without smoothing (3rd model), but here it was necessary to use a mesh without boundary layer and this is the most probable reason of the differences. For the overset, 1st and 2nd dynamic mesh configurations, any visible motion discrepancies are visible only for the upper leaflet during the closing stage.

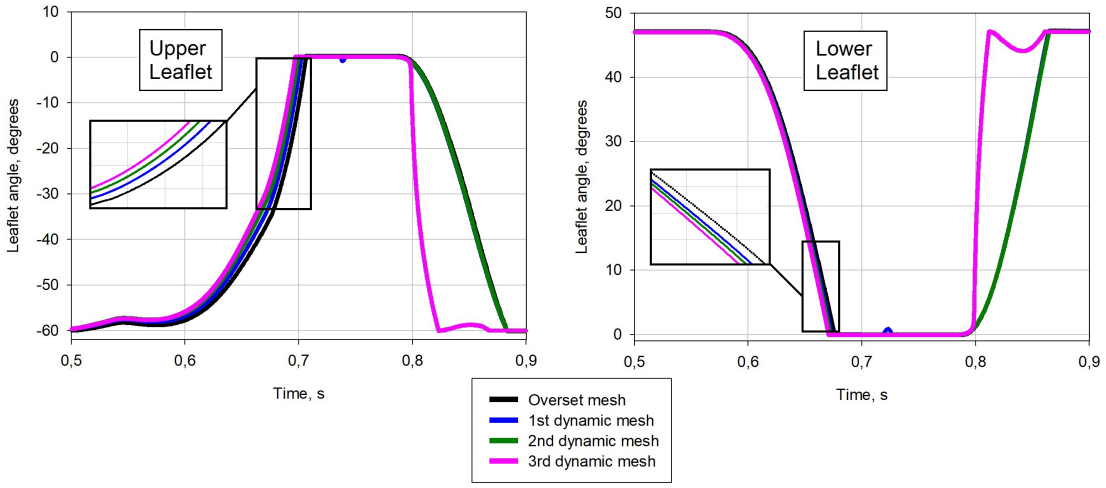

Figure 4.13: Comparison for the 3rd measurement data set between the numerical overset mesh model results and three different dynamic mesh modules

4.5.7 CFD results and valve performance indicators

In this section some typical indicators for artificial valves were described and determined. The results with the overset mesh applied was used for this purpose. Note that some of the quantities will be highly dependent on the patient's specific geometry and blood flow conditions; however, the tendency for the regurgitation gradients and the effective orifice area should present regularity for the same prosthesis construction. To assess how the blood flow specifics influence onto indicators, five datasets' numerical results were used for indicators calculation. Part of the results described in this section, such as wall shear stresses and pressure gradients on leaflets' walls, are not measurable and can be determined only via CFD calculations.

The pressure drop was calculated between two points located on the centerline, 3.5 mm before the valve and 3.5 mm behind (Fig. 4.15). The monotonicity of the curve is concurrent with the inlet velocity profile. Visible oscillations are present during the moments when the valve is moving, and are more apparent when the valve becomes fully closed or fully opened. The pressure drop peak was maximum for the 3rd data set and was equal 0.4 kPa, where the mimimum peak equal 0.31 kPa was present in 4th data set. The exemplary curves for mentioned data set models are presented in Fig. 4.15. The results achieved are close to the validated pressure drop values

in [79], [119], [147], [148], where pressure drops were at a level of 0.2 kPa to 1.0 kPa, depending on the velocity profile of the inlet and the geometry of the vasculature.

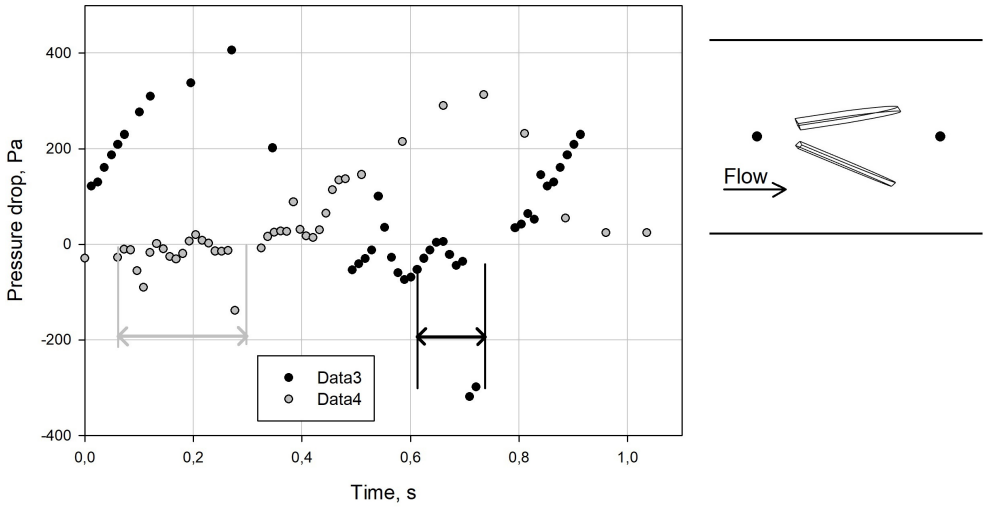

Figure 4.14: Pressure drop calculated between two central points shown at the inset for for 3rd and 4th dataset. Marked time intervals correspond to the valve closing phase.

High- and low-pressure values are present on both sides at the edges, especially when the closed or opened state is achieved. The highest leaflets' pressure gradient, calculated as the difference between the maximum and minimum pressure exerted at their walls, was present during the maximum inlet velocity and was on the level of 2.5 kPa, see Fig. 4.14. Presented longitudinal and transverse cross-sections indicate high gradients, which could be successfully calculated with the described numerical mesh.

The WSS values are high in the time of increased inlet velocity and from the moments when the valve starts to close. The maximum value equals 54 Pa and it was achieved for the 2nd dataset. As can be seen in Fig. 4.16, the maximum achieved wall shear stresses are rising with the applied inlet velocity. Also, the values are higher for the lower leaflet for all datasets, which may be due to the upper leaflet is closer to parallel during opened state.

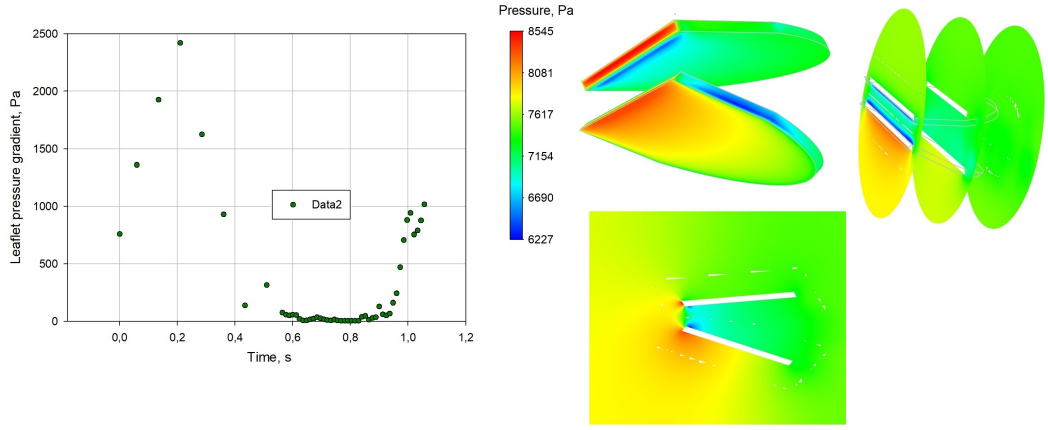

Figure 4.15: Pressure gradient on the leaflets walls for 2nd dataset. The contour is presented for the time instant corresponding to the highest gradient

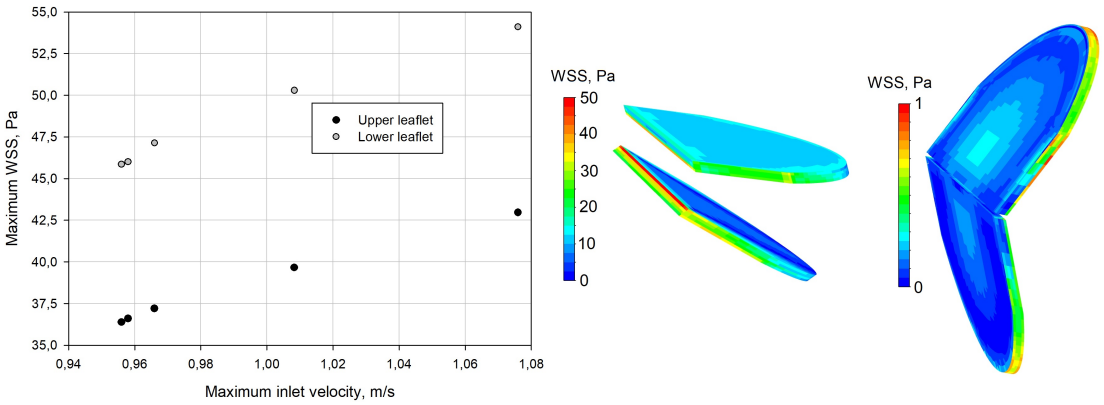

Figure 4.16: The maximum wall shear stress on the leaflets walls, presented for all datasets and correlated with the maximum inlet velocity. The chart presents the WSS contour during the closed and opened valve state

The measured EOA value by [120] for the St Jude Medical® bileaflet valve equals 2.08 cm^2 and 3.23 cm^2 for size 21 mm and 25 mm, respectively. The calculated average value from the simulations of five data sets performed in this research was equal 2.73 cm^2 with standard deviation 0.05 cm^2, which indicates the appropriate prosthesis performance and almost constant EOA value, regardless what pressure, flow and cycle time applied.

Figure 4.17 presents the velocity pathlines for the 5th dataset model. Five different time instants were considered: the moment when the valve started to open (0.321 s), the opening completion (0.429 s), the maximum inflow time (0.666 s), the closing

start-up (0.128 s) and closing completion (0.189 s). As can be observed, the pathlines in the valve vicinity obtain irregular vorticity-like patterns, especially when the valve is moving. At a distance of several pipe diameters, the flow field becomes regular, no matter what the angular positions of the leaflets are. During the opened state, a stable three-jet flow is achieved and remained, which can be stated by comparing 0.429 s and 0.666 s time stamps' contours. During the closing, startup, and closed states, some minor regurgitation can be observed. Here, the velocity values are higher when the closure is complete, because of a small area of the leakage gap. Therefore, the regurgitation is not substantial, due to the fact that the already small reversed velocity values instantly provoke valve closing, and the leakage area is small.

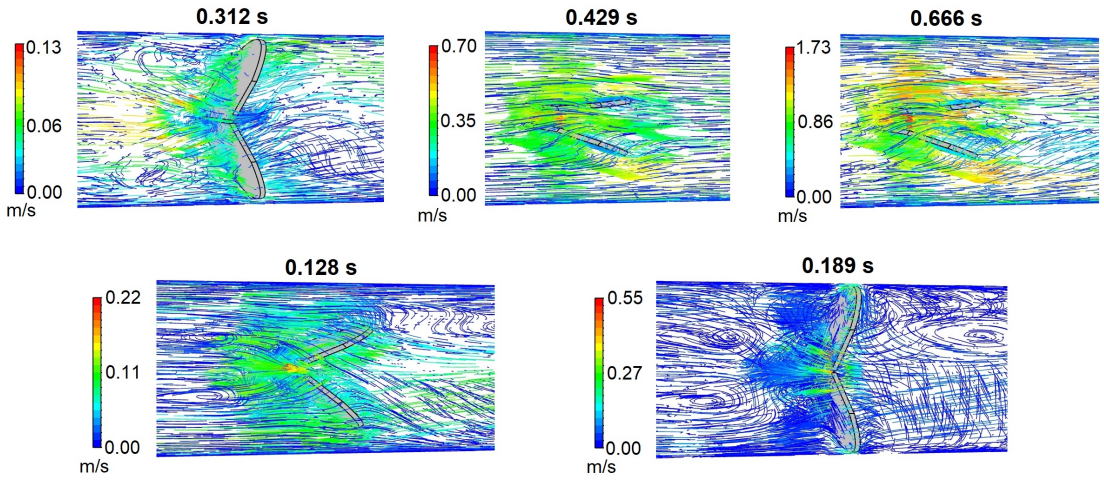

Figure 4.17: Pathlines of velocity magnitude for 5th dataset, presented for five different time instants

The supplementary video materials can be found using the above QR code or the following link:
https://www.youtube.com/playlist?list=PLm0c-zXrCqEKiZ8tOxeWXtuV13FYyJ3Fk

Chapter 5

Modeling anatomical and artificial aortic valve stenosis

Based on the research and findings described in Chapter 3. and Chapter 4., the model was applied for the comparative study of blood flow through the artificial bileaflet valve and the anatomical (human) aortic valve. The $k-\varepsilon$ turbulence model was used. The 6DOF model with adaptive timestepping, described and validated in Chapter 4., was applied for the artificial valve implanted within the real patient's vasculature. To compare the results with those obtained for the human valve, the coupled dynamic and overset mesh model was created, to encounter the elastic body deformation in the numerical domain. The FSI model for the elastic valve was realized by coupling of the Ansys® Fluent and Mechanical solvers. The same FSI and moving mesh protocol can be applied for the modeling of the artificial deformable valves, biological or synthetic. The in-house OpenCV program was created to determine the elastic valve opening and used for numerical simulation, which can also be applied to the measurement of the test rig and the examination of the patient. Real 2D and 3D vasculature and valve geometries were created based on the echocardiography images available in the literature.

Calcified aortic valve disease is the most common among valve diseases, reaching 13% in the general population over 65 years [5, 6]. After valve replacement by the artificial bileaflet aortic valve, the risk of calcification process, resulting in stenosis is still present, however - this is not thoroughly invastigated in literature. Therefore, the

calculations of anatomical and artificial valve models were performed for the various severity of the atherosclerosis, not previously published for the bileaflet mechanical valve. The impact of the calcification process on natural and artificial aortic valves was assessed and compared.

Two moving mesh strategies were coupled, for several reasons. Firstly, FSI, as well as individual Ansys® Fluent calculations, were much more stable, compared with the previous attempts with the dynamic mesh (smoothing and remeshing) only. The reason is that using the described strategy, the prepared meshes of the structural components were maintained throughout the heart cycle, including the leaflet boundary layer. Also, the creation of highly-skewed, deteriorated tetrahedral cells was avoided, and they were created in the case of separate dynamic mesh for FSI. Furthermore, when remeshing was not used, the structural mesh in the entire geometry could be imposed, which also improved the convergence and limited cell count. The second motivation of application of the described approach in this investigation is the great limitation of the wall clock time, caused by the usage of the structural mesh in the component and background fragment as presented in Figure 2.2 (the less amount of cells, better quality indicators) and the avoidance of the computationally expensive remeshing. Also, more stable FSI calculations allowed to use about two times greater time step size. Moreover, the usage of coupled overset and dynamic mesh modules eliminates problems with fluid domain collapsing, when the elastic leaflets connect each other and the fluid domain vanishes. In this situation, a small number of orphan cells were present, but the solving could be further processed, which will not be possible in the case of dynamic mesh-only usage, due to negative cell volume error.

5.1 Three-dimensional aortic valve model

The medical measurement data published by [112], [113] and [114] were used to create the aortic root geometry, which is the connector of the ascending aorta and the left ventricle. It supports the aortic valve leaflets and assists to the proper valve functioning among others by production of the laminar flow and better transition of the large amount of blood from the ventricle [111]. The geometry consists of the three

identical parts (called sinuses of Valsalva), where each of them is symmetrical, so only 60° portion was created. Then, the appropriate mirror operations were performed to create the complete root. The root is ended by the ventriculoaortic ring (inlet side) and the sinotubular junction (STJ). To represent the ventricular portion, the simple 13 mm straight tube was added by the extrude operation.

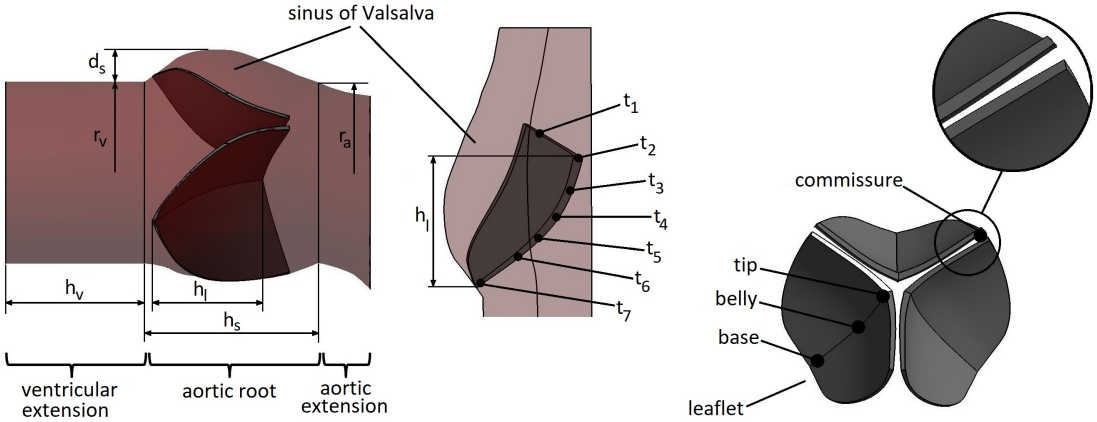

Figure 5.1: Three-dimensional aortic root and leaflet geometry. Root dimensions: r_a=8.6 mm, r_v=8.6 mm, d_s=4.13 mm, h_s=15.2 mm, h_v=8.94 mm; leaflet dimensions: h_l=5.1 mm, t_1=0.55 mm, t_2=0.75 mm, t_3=0.47 mm, t_4=0.25 mm, t_5=0.21 mm, t_6=0.12 mm, t_7=0.31 mm

On the aortic side of the root, the STJ (aortic extension) was created in the way that lead to the proper merging of the root with the patient aorta geometry, used in previous research [23, 110] – see Fig. 5.1. The loft operation between the root and aorta cross-section surface properly merged these regions.

The valve leaflets were created simultaneously with the root geometry and in both cases creation of 60° geometry portion was sufficient to achieve the complete geometry via the mirror operations. Thus, the 3D geometry of the one leaflet half was drawn. The leaflet thickness is changing across the three axes, in the whole geometry scope, between the minimum value of 0.12 mm in the belly region and maximum of 0.75 mm on the tip (called also Nodulus of Aranti) – Fig. 5.1. The variable thickness was achieved using the mesh of points that are coincident with the edges of the leaflet surface laying on the symmetry plane. After preparing the proper points, they were converted into the closed edges loop, and then the symmetry surface was applied. Afterwards, the sweep operation using described surface has to be performed. The sweep paths were achieved

using the mesh of points as well. These points coordinates were applied in the way to achieve desired thicknesses across the sweep and to obtain the small gap between the neighboring leaflet (commissure region, see Fig. 5.1). The mirror and rotation operations were applied, resulting in the complete valve. The created leaflets are attached to the root wall without any gaps in the attachment. The space between the leaflet and root wall is identified as sinus of Valvsalva (Fig. 5.1).

The overset component bodies creation was performed in Designmodeler on the original, single undeformed leaflet, by thickening two millimeters in the every direction. Three components intersects eachother at the upper part during the closed state, which is allowed in the overset method.

For the proper numerical mesh creation, the component body was divided each into 15 bodies. The mesh densifications have to be imposed, to create the boundary layer coming from the leaflet wall and to fit properly into the background mesh boundary layer, avoiding orphan cells. Finally, the conformal mesh of 63.7k cells was created, where 13 of 15 bodies were meshed with the swept hexahedral cells, and 2 of them with swept prism cells (Fig. 5.2A). The background mesh − aortic root, was meshed using hybrid approach. The continuous 7-element boundary layer with the smooth size transition between the prism boundary and inner mesh was imposed. The final background mesh consists of 867k hybrid elements (Fig. 5.2B). Each of finite-element leaflet mesh consists of 36.3k elements and 299.6k nodes and includes 15-node prism SOLID186 and 10-node tet SOLID187 elements, and was created as the meching mesh to the component bodies' mesh (Fig. 5.2A).

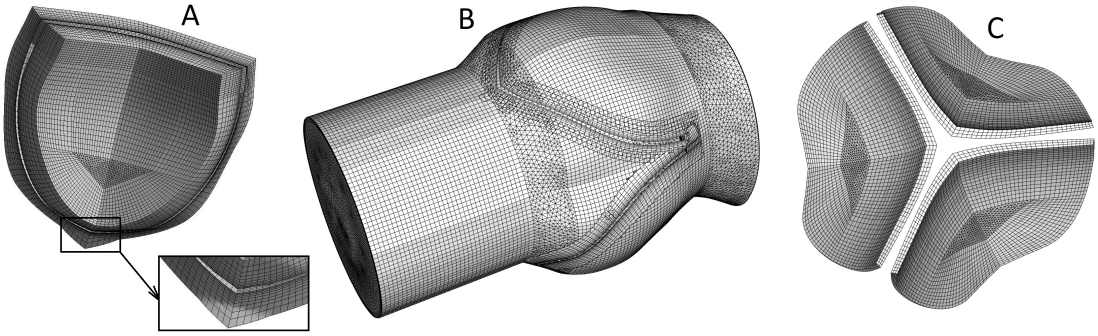

Figure 5.2: Numerical mesh prepared for 3D flexible valve model: A − component mesh, B − background mesh, C − solid leaflets mesh

Based on carried out preliminary calculations, it was pointed that to perform calculations of only 0.06 s heart cycle, it took about 16 days using 12 2.4 GHz Intel Xeon E5-2620 cores. This clearly indicated that to reach multivariant numerical results in reasonable time frame, the 3D approach need to be reduced to 2D models. Thus, at this stage of the research, 2D geometries were used to determine the motion of the valve and the characteristics of blood flow. [31, 32, 62, 63, 68, 149, 150] shows that the selection of 2D model is reasonable, while its testing is required because *all models are wrong, but some are useful* (George E. P. Box). Nevertheless, the initial 3D model result is described. Figure 5.3 present the deformation and velocity contours for time 0.06 s i.e., beginning of the heart cycle. During this time, the inlet velocity from used transient profile was on the level of 0.18 m/s, whereas the determined peak velocity between the leaflets was equal 1.38 m/s due to the narrowed flow region, as shown in Fig. 5.3B. Small vortices are visible for all three sinuses, however the velocity presents there low values. The total leaflets deformation is presented in Fig. 5.3A, where the deformations (except scale values) were magnified by a factor of 2. Also, the non deformed contours are shown by wireframe, to indicate the initial state. The maximum values equal 1.3 mm were present in the same regions for all three leaflets, i.e., at the lower-middle zone at both leaflet sides. The same conclusions were made in the review article [151] and in research works [4, 71, 152]. These articles describe the progression of the calcification process, based on the differences in leaflet strain. In conclusion, during calcification and aging, the arteriolosclerotic plaque is deposited primarily in the location of the high strains, as in the determined zones presented in Fig. 5.3A.

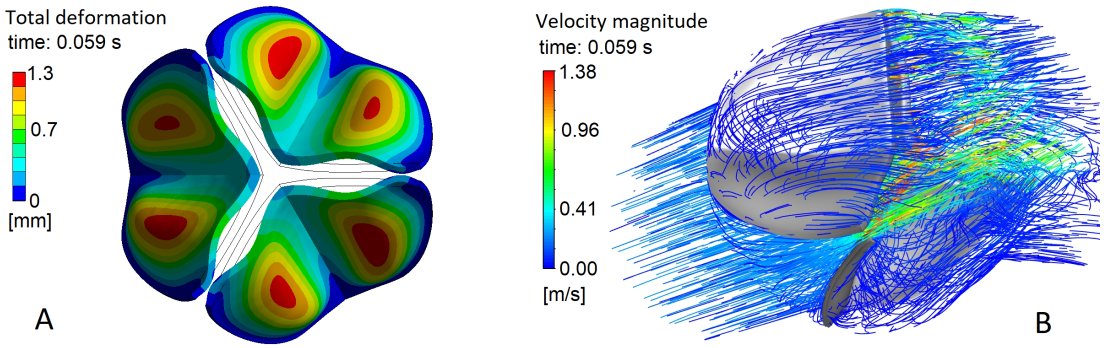

Figure 5.3: Initial results for the 3D model of healthy aortic valve, **A**: deformation contour and **B**: velocity pathlines

5.2 Two-dimensional aortic valve model

Due to computational demanding, two-dimensional geometrical models were used to perform the series of full heart cycles calculations. The leaflet geometry model creation was performed separately for the anatomical and artificial valve, where the same vasculature, i.e.ventricular portion, aortic root and arteries, was used. The 2D geometry of the aortic valve with the vasculature was created based on the information provided in [149], where the echocardiography using 7 and 3 MHz scanners (GE Vivid 7 ultrasound machine) to gain patient images. The geometry consisted of the ventricular extension, the sinus aortic root, the coronary arteries, and the aortic extension. Flexible leaflets are attached at the end of the ventricular portion (Fig. 5.4). The developed geometrical model assumes constant leaflet thickness at the level of 0.324 mm. Coronary artery dimensions shown in Fig. 5.4 were defined based on specific data included in [62].

To create the component meshes for the anatomical valve, each leaflet surface was extruded in its normal direction by 1.7 mm. Subsequently, the mesh of structural hexahedral components was created, where the cell size increased with the distance from the leaflet wall. In this way, better boundary layer resolving was provided. The background geometry was created by filling the cutted leaflets region, shown at Fig. 5.4A, as the moving mesh algorithm itself cuts the leaflet fragment from the background mesh. The entire vasculature region was then meshed using structural hexahedral elements with the boundary layer, as presented in Fig. 5.5. The leaflet mesh for the Ansys® mechanical solver was created in a way that its nodes match perfectly with the component geometries, for better stability of force and displacement transfer. Two elements per leaflet thickness was maintained for the entire leaflet length. The hexahedral elements with midside nodes were used for the structural solver.

To prepare the component and background meshes, along with the moving mesh settings, leading to absorb the solid motion with good cell quality indicators, the meshes testing is demanded. It was not sufficient to check for the orphan cells with the stationary leaflets, as they may appear during the motion, i.e. solution procedure. Testing many mesh sets using the FSI approach would demand tremendous amount of time and

computational resources. Thus, the macro using UDF was created, which impose the leaflet motion, and it could be used with the standalone Ansys® Fluent solver without solving either a flow or structural field. The description of the developed UDF and Ansys® Fluent journals can be found in the Appendix C.

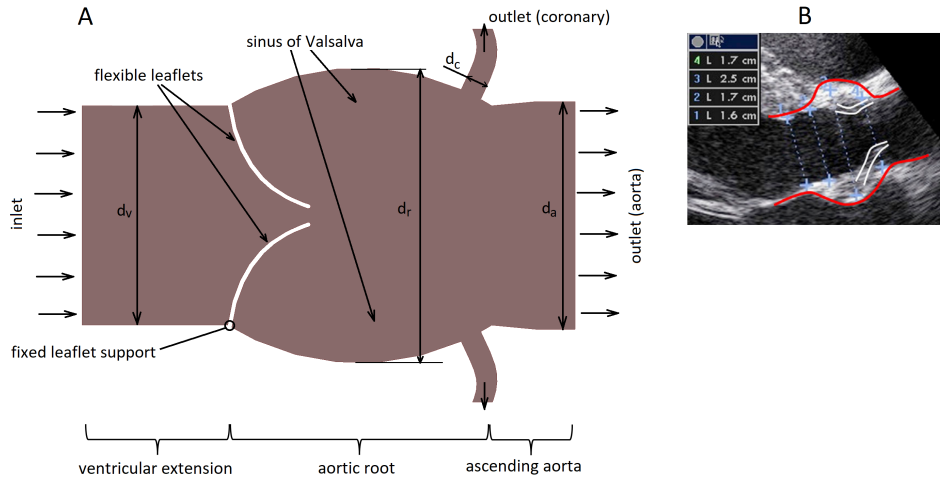

Figure 5.4: **A**: Two-dimensional aortic root and leaflet geometry; **B**: short axis b-mode echocardiography image view *(reproduced from reference [149] with permission of Elsevier)* used to determine geometry dimensions: ventricular diameter $d_v = 17.3$ mm, root diameter $d_r = 23.3$ mm, aortic diameter $d_a = 18.0$ mm, coronary diameter $d_c = 1.73$ mm

To check the influence of the domain discretization on the predicted pressure and deformation values, the **mesh sensitivity analysis** was performed ruining numerical simulations with three different mesh types:

– *coarse* (background: 9,492 cells, component: 862 cells, leaflet: 101 cells),

– *medium* (background: 12,392 cells, component: 1,030 cells, leaflet: 109 cells),

– *dense* (background: 15,260 cells, component: 1,194 cells, leaflet: 117 cells).

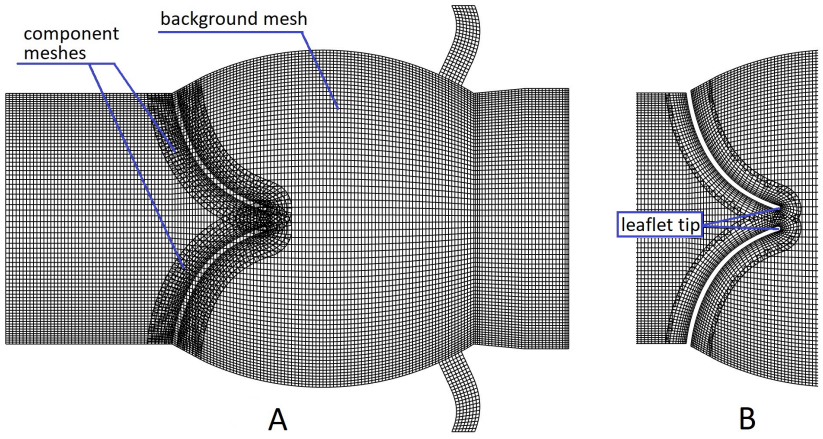

Figure 5.5: Two-dimensional mesh for FSI analysis: **A** – component meshes overlayed on the background mesh, **B** – close-up on the mesh state after the overset process, with cutted valve leaflets and maintained leaflets boundary layer

Firstly, for all mesh resolutions, i.e. *coarse*, *medium* and *dense*, the mesh settings were modified, till the motion was absorbed in the domain with good moving mesh quality. The quality was assessed based on the skewness, cell quality, and aspect ratio values. Furthermore, the presence of orphan cells and negative cell volumes was checked. Subsequently, the FSI calculations for sensitivity analysis were performed for the first 0.12 *s* of the heart cycle. During this time interval, the flexible leaflets undergo the highest deformation, due to the increasing inlet velocity as it is shown in Fig. 5.9). Two quantities were tracked and compared to check the difference between the meshes: displacement of the upper leaflet tip (marked in Fig. 5.5) as structural result, and the pressure drop on the valve as the fluid result. Figure 5.6 shows that the tracked results for three mesh configurations, do not differ much. For the pressure drop, some fluctuations are visible at the beginning of the computation, but only for the coarse mesh. The leaflet tip displacement curves diverge mainly during the moment when the courses change monotonicity, due to the leaflet rebound. Apart from that, the displacement courses coincide, which can be stated for the beginning of the cycle, where the deformations of the valve leaflet are considerable, and for the end of the calculated time interval, when the leaflet rebounds end. The discrepancies between the results of the *coarse* and *medium* meshes are greater than those identified between the *medium* and *dense* meshes. Based on the performed analysis, it was observed that the density of the mesh type *medium* is sufficient to be used for valve study.

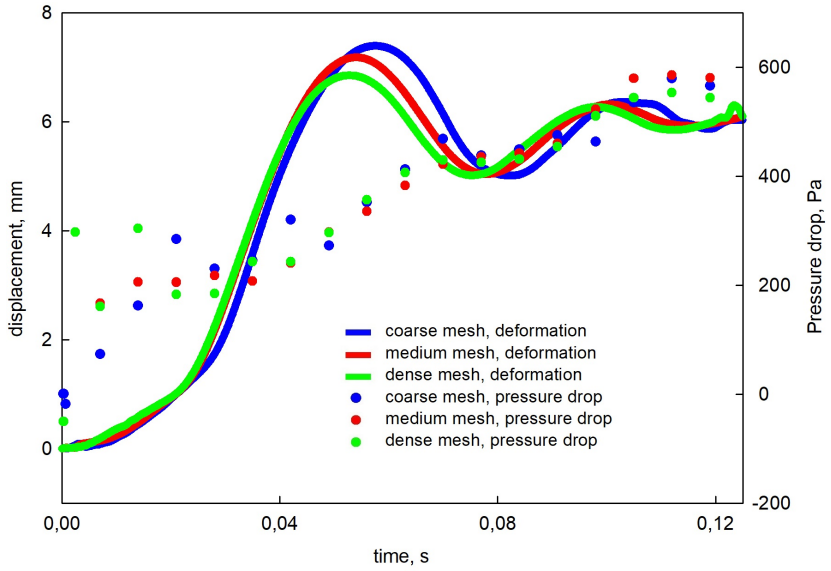

Figure 5.6: Flexible valve mesh sensitivity analysis, in terms of the leaflet deformation and pressure drop values, which lead to the *medium* mesh selection, for the simulation series; displacement was determined as the upper leaflet end point change in its initial location, and the pressure drop was calculated between two central points, before and after the valve

The conclusions based on the flexible valve mesh sensitivity analysis was used for creation of the numerical mesh for the artificial valve. The same background mesh was used as for the anatomical valve, as illustrated in Fig. 5.4), except for the valve leaflets. The artificial valve geometry was created based on the user manual. Taking into account the dimensions of the ascending aorta of the patient and the aortic root, the valve type of 16.8 mm inside diameter and 0.455 mm leaflet thickness was chosen. To create the geometries of the overset components, the leaflets were extruded in their normal direction by 1.7 mm, same as for the anatomical valve. The same numerical mesh density was used, as selected *medium* type based on anatomical valve FSI sensitivity analysis.

As discussed in Section 1, when the stenosed aortic valve is replaced by the prosthetic mechanical bileaflet valve, the calcification process may still arise. This comes from different factors, as blood cell lysis and stagnation areas in the valve vicinity. The literature data [83, 85, 86] describe the process of the plaque deposition in the valve region. Using this information it was possible to prepare the geometries and meshes by properly increasing the vessel obstruction. The base background geometry and mesh

editions were required. The meshes created for the healthy and calcified bileaflet valve are presented in Fig. 5.7A and are described in Tab. 5.1, where progressive calcification is considered. The accumulation of plaques from arteriolosclerosis causes obstruction of the vessel lumen, determined in the table as the percentage difference between the minimum diameter found in the aorta and root region, and the noncalcified ventricular extension diameter. Moreover, due to the presence of plaque obstruction, the leaflet motion is limited by a certain number of degrees, also noted in the table. In this work, the four different stages of calcification were analyzed, which required the creation of three geometries of the calcified vasculature, presented in Fig. 5.7A. The 4^{th} stage of calcification was not modeled by further obstruction of the flow area; instead of this, the upper leaflet motion was permanently blocked in its closed state throughout the heart cycle. This situation occurred in the case report [86]. Thus, during the last analyzed calcification state, only the lower leaflet rotated due to flowing blood.

Calcification stage	Flow obstruction, %	Leaflet motion obstruction, degree	Leaflet motion
1^{st}	5.3%	8°	both movable
2^{nd}	10.8%	12°	both movable
3^{rd}	20.9%	16.5°	both movable
4^{th}	20.9%	16.5°	upper blocked

Table 5.1: Analyzed artificial valve calcification stages with corresponding obstructions created by arteriolosclerosis plaque

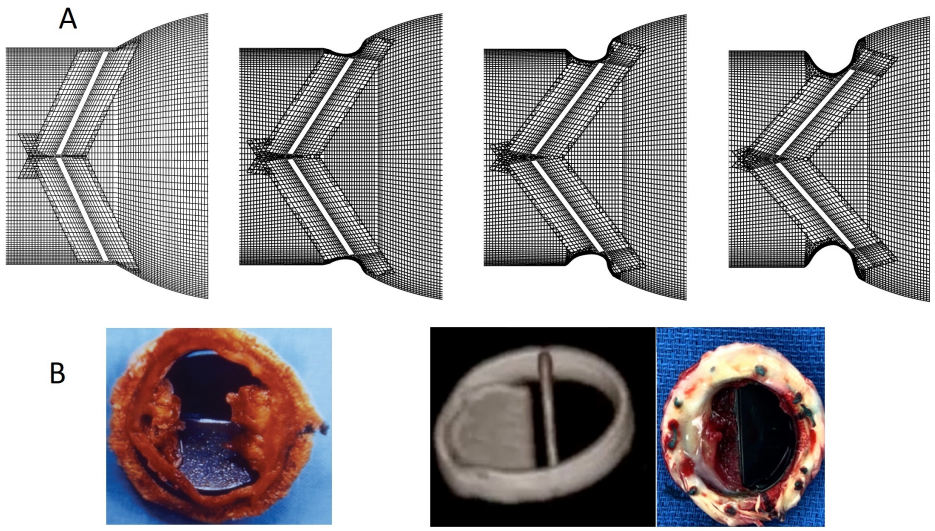

Figure 5.7: **A**: Fragments of the numerical meshes prepared for the analysis of the artificial valve calcification process, going from healthy (left) to severely stenosis (right); **B**: case reports concerning calcified artificial valves (reproduced from references [85, 86] with permissions)

5.3 Numerical model setup

The 6DOF-FSI model was applied for the rigid bileaflet valve, where for the elastic human valve the partitioned FSI approach was used. For blood flow, the velocity-inlet and pressure-outlet boundary conditions were applied using a set of UDFs implemented in the solution procedure. The inlet profile was obtained from measurement data [149], based on Doppler imaging. The reversed flow to the domain starts at 0.31 s after the heart cycle beginning. The transient profile for coronary outlets was taken from the clinical data of the average coronary flow [153]. To obtain the required information from the interior domain, the pressure-outlet boundary condition was considered at the aorta outlet. For the blood fluid properties, a density of 1051 kg/m^3 and Newtonian viscosity 0.0035 kg/(m·s) were used [116]. The non-Newtonian properties were not implemented here, as the results are compared with the works and laboratory measurements considering constant Newtonian viscosity.

For the structural part of the anatomical valve model, the fixed support boundary conditions were applied to the surfaces where the flexible leaflets are attached, as illustrated in figure 5.4. The mechanical properties of the linear-elastic solid bodies for

the structural solver were used as follows, density 1060 kg/m^3, Poisson's ratio was set to 0.3, the Young modulus was defined at the level of 2 MPa for the healthy valve and 5 MPa, 10 MPa, 20 MPa, 30 MPa for different calcification stages [62, 149]. The reason why simpler linear-elastic (Hookean) material model was used, is the stability, but also the convenient modification of the tissue stiffness, corresponding to the progressive calcification process. Therefore, only one material constant (E) was modified to increase a stiffness (similarly as in [62, 149]), where four, up to six constants should be modified in the case of the hyperelastic material – dependent on the chosen constitutive model of the stress-strain relationship. However, to compare the differences between the linear-elastic and hyperelastic model results, and assess the convergence issues, an effort was made to solve these non-linear material models. The Ogden [37] and 3-parameter Mooney-Rivlin model [38] was not possible to solve due to the typical convergence problems coming from the model non-linearities. Changing of the timestep size, and also structural solver number of substeps, did not help much. Mentioned problem and their occurrence is described in the article [154]. Also, the impact of the material characteristics, as plasticity and collagen activation, was investigated in [73]. For described model, only 5-parameter Mooney-Rivlin was possible to solve without structural solver convergence issues, and the results comparison with the linear-elastic model is presented in Figure 5.8. Some difference in the opening is observed, however the material model constants were formed for different substances (valve leaflets and aorta walls) and using different measurements (two literature sources). As observed for the hyperelastic model, when the local deformation rises, the susceptibility to further strains changes – not linearly as for the Hookean model. This leads to more curvy-like shape for the hyperelastic model. Also, as shown at the close-up, the leaflet hyperelastic geometry deforms in the attachment region - this probably comes from the equal leaflet thickness assumption, or the improper compressibility constant, and further investigation is demanded to overcome this issue. In conclusion, much work is demanded to converge a hyperelastic model, as changing structural solver settings, probably mesh edition and even geometry edition, also how to change several model constants to increase stiffness is not very straightforward and clear at-a-glance. Therefore, this work was limited to the linear-elastic model.

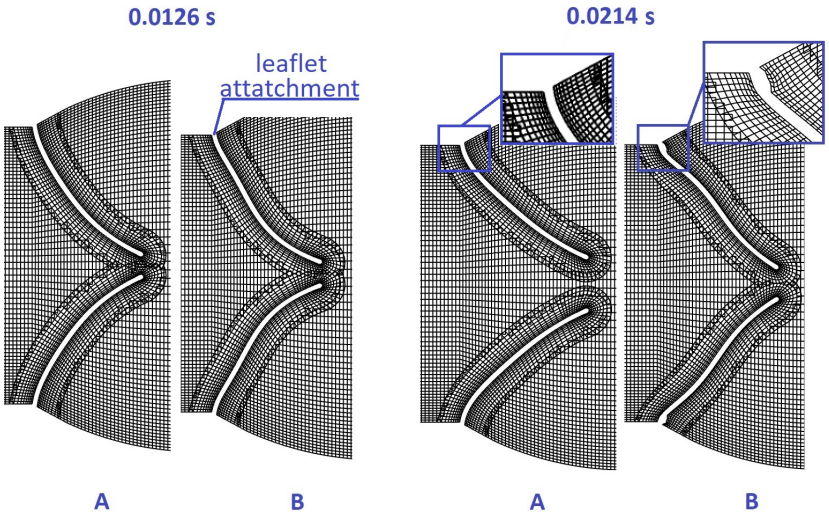

Figure 5.8: Comparison between the linear-elastic **(A)** and hyperelastic **(B)** material model results, for two time instants. The close-up present excessively deformed leaflet in the attatchment region for the hyperelastic model

In the simulations carried out, the walls of the aorta were assumed to be a rigid body. The contact between valve leaflets was not modeled, as the overset mesh enabled a possibility of the complete valve closure and the solid body penetration did not cause problems, neither on the fluid, nor the solid side. Several assumptions have been made to speed up the computations and limit the model nonlinearities. Two-dimensional geometries were used to perform multivariant analyses. The constant leaflet thickness was employed in the 2D anatomical valve model, where they are thicker in the place of attachment and between the belly and tip. The single-material isotropic, linear-elastic solid model was used to improve the model stability, where in reality the valve leaflet is the multilayer anisotropic, viscoelastic and hyperelastic structure [69]. The aorta walls were assumed rigid and stationary.

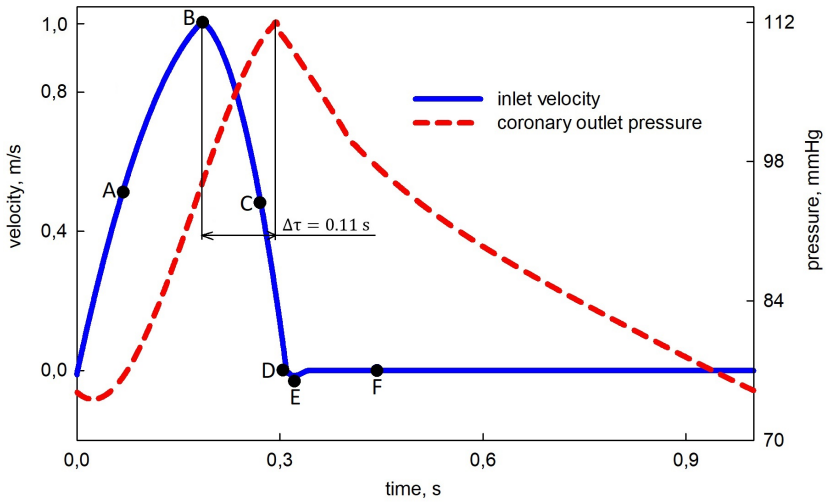

Figure 5.9: Physiological boundary conditions, with the characteristic points: **A** - early systole, **B** - peak systole (maximum inflow), **C** - late systole, **D** - systole ending / diastole beginning, **E** - peak reversed flow, **F** - diastole

To assess the validity of the commonly used rigid blood wall approach, applied in all the researches cited in the Thesis, the additional model of the non-calcified aortic valve with the elastic walls was solved. The material properties for the analyzed region were as follows: Poisson's ratio equal 0.3, Young modulus: 12.5 MPa for the fibrous ring, 10.53 MPa for the aortic sinus, 7.41 MPa for the sinotubular junction, 1.7 MPa for the aorta walls [155, 156]. A constant wall thickness of 0.865 mm was applied as 10% of the lumen of the vessel [23], except for the coronary arteries, where the thickness of 0.5 mm was used [157]. This is the case for which the most prominent wall deformations are expected, as the thicknesses up to 4 mm were found in the literature, and also the wall thickness increases with age [4, 157–159]. Therefore, the maximum deformations that could be expected in the case of the elastic walls were determined. The geometrical model with marked solid zones is presented in Fig. 5.10A. As can be observed, the fluid zone exceeds the solid region and the fixed support location. It was set to realize hydraulic run and also as the physiological function of the aortic fibrous ring is to provide the support to prevent the backflow, when the aortic valve is opened [160]. The point for which the vertical deformation is tracked is marked as **P**. In this location the greatest deformations were noticed. As presented in Fig. 5.10B, the maximum y-deformation was on the level of 1 mm, which corresponds to 4.3%

of the root diameter. Considering that calculated case was related to the lowest wall thickness found in literature and the tracked deformation was located in the position of the highest strains, the rigid wall assumption with the elastic leaflets was recognized as reasonable and also used in the further analyses.

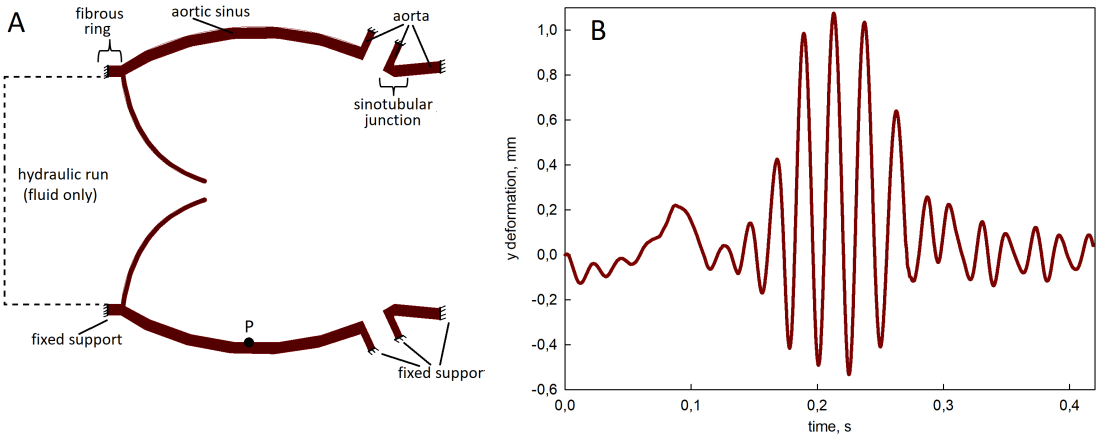

Figure 5.10: Materials and boundary conditions used for the structural model of the elastic blood walls **(A)**; vertical deformation course of the point marked as P

5.4 Model results

The 2D model was validated, based on literature data [149, 161], in terms of the transient leaflet shape and pathlines of velocity magnitude. Beside that, the calculated values, both for the artificial and anatomical valve, were compared with measurement and numerical researches found in literature. Figure 5.11 presents a comparison of the leaflet orientations for the B-mode-echo images and the healthy valve case images of the FSI simulations. The B-mode echo is based on production of points by ultrasound signal, whose brightness depends on the amplitude instead of the spiking vertical movements [162]. Results are presented for three different flow and leaflet states: diastole (flow stagnation), systole (for the maximum inflow), and closure, when the inlet velocity declines and the valve starts to close. For all presented frames, the results represent good agreement, showing the proper application of the numerical method.

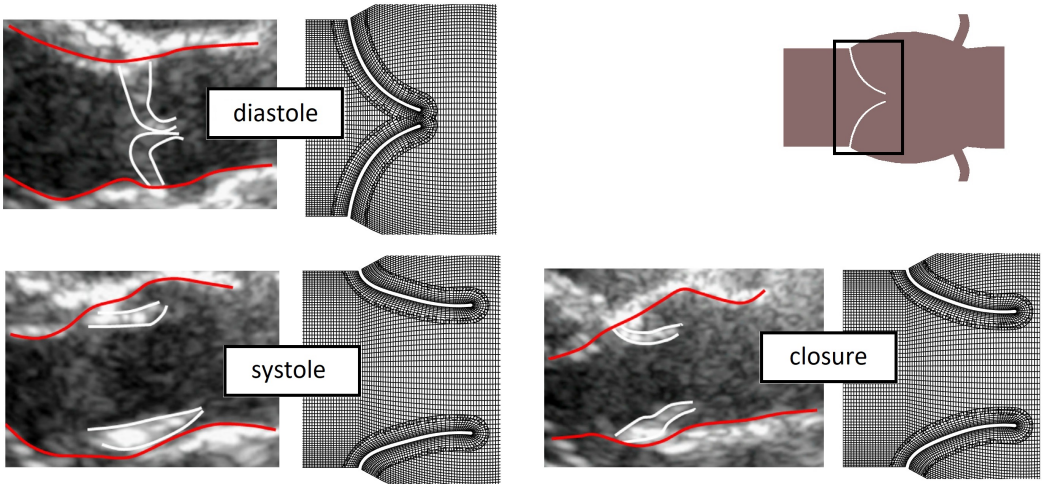

Figure 5.11: Comparison of the leaflet shape determined by the model, with b-mode echo images (reproduced from reference [149] with permission of Elsevier), for different moments of the heart cycle, along with the coupled overset-dynamic mesh operation depicted for geometry fragment shown at the inset

The velocity pathlines were compared in Fig. 5.12 with the PIV experiment [161], for the systole phase. Good agreement was stated in terms of the flow regime and produced recirculation eddies, however, small differences are visible, which may be caused by the presence of the coronary arteries in the numerical model and different geometrical features.

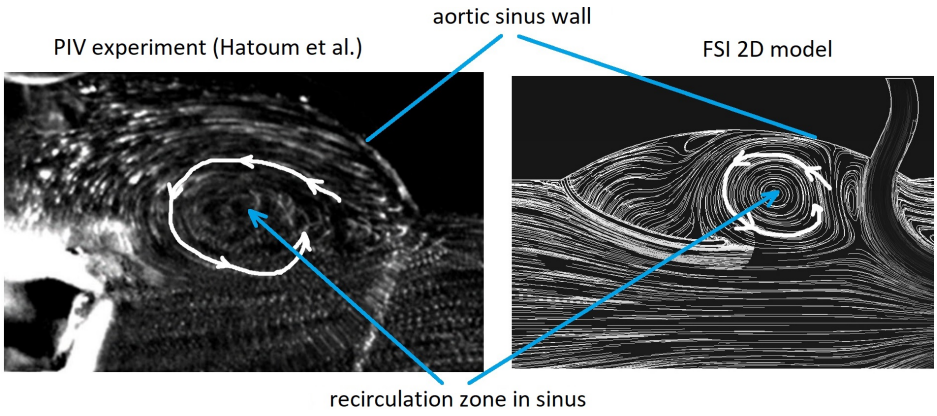

Figure 5.12: Comparison of the velocity pathlines between PIV measurement [161] and 2D FSI simulation for the healthy valve

The valve kinematics, calculated using the applied human and artificial valve models, is presented in Fig. 5.13. The vessel lumen (valve opening) was determined as the smallest flow diameter in the elastic valve region. Determination of the valve opening from the images produced by solver after every timestep, will demand tremendous effort, if it was done manually. Therefore, the OpenCV [127] within the *Python* environment [163], was used for the automatic processing of the images produced by Fluent, to read the values. The source code can be found in Appendix B. The healthy anatomical valve present the highest opening on the level of 10 mm, and with the calcification process, the valve opening is limited. Similar conclusions were drawn for the artificial valve; however, the opening for the bileaflet valve was known a priori due to the known plaque deposition. The vessel lumen rate of change slightly decreases with the calcification stage. The healthy anatomical valve becomes fully closed at time 0.33 s, where the stenosed valves did not become closed, as the opening to the level of 0.5 mm was maintained. The vessel lumen monotonic fluctuactions are caused by their flapping motion, which can be observed in *Supplementary videos*. Comparing the vessel lumens during peak systole, the severe calcification (4^{th} stage, E=30 MPa) causes drop in opening by 35.9%. A very similar drop was observed using computed tomography [71, 164, 165], where the Geometric Orifice Area (GOA) was determined, due to the 3D orientation, and the GOA peak values decreased by 38.7% due to heart valve stenosis.

Figure 5.13B, shows the comparison between the kinematics of noncalcified anatomical and artificial valve. The artificial valve leaflets could rotate freely from the position indicated as 0° (fully closed state) to 60° (fully open state). Both valves are opening at the beginning of the heart cycle, when the inflow velocity increases. Similar time intervals are demanded, to change state from fully closed to fully opened, and vice versa, except for some minor mechanical valve fluctuations of angular position at the end of the opening stage (0.015 s$-$0.075 s). The closing phase starts earlier for the anatomical valve, at the moment of maximum inflow (0.185 s), from which the flow starts to decrease. Therefore, decreasing inflow is sufficient to provoke elastic valve closure, while for the artificial valve, reversed flow causes closing, as presented in Fig. 5.13B. However, the described closing startup delay is not a problem because the function of

the artificial valve is to block the reversed flow. The same conclusions considering the motion of the bileaflet valve and the duration of the opening and closing phases can be found in related researches [17, 56, 75, 78, 79].

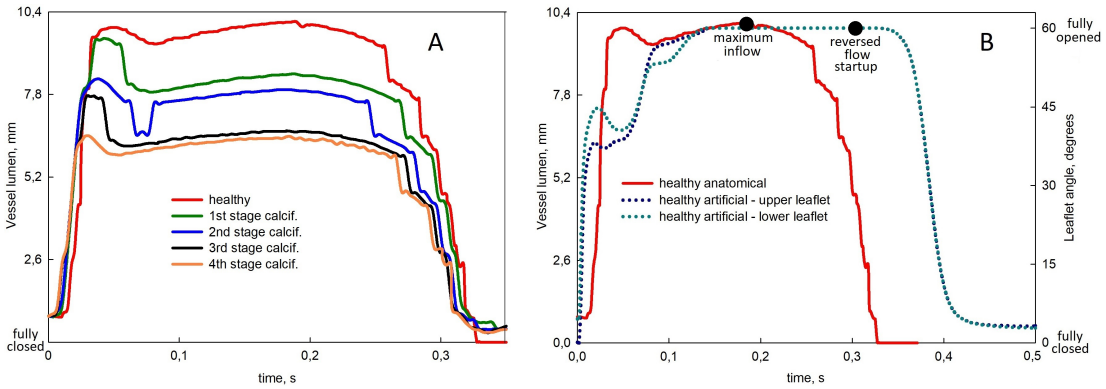

Figure 5.13: Anatomical and artificial valve leaflets kinematics, determined by FSI and 6DOF-FSI models, accordingly. The valve stenosis caused visible drop in the valve opening (**A**). The artificial bileaflet valve closure starts with delay compared with the human valve (**B**)

The transvalvular pressure gradient should be as small as possible, where for the stenosed valve values up to 6 kPa can be observed [166]. The pressure drop was determined for the anatomical and artificial valve, for all analyzed calcification stages. The results changing over time are presented in Fig. 5.14A and B. Results indicate that the transvalvular pressure gradient increases within the calcification process. For the healthy anatomical valve, the maximum value of 850 Pa was observed, where for the artificial valve, the lower value equal 240 Pa was present. The type of mechanical valve of the bileaflet is known from the lower TPG values and the values determined are close to the validated pressure drop in [79, 119, 147, 148], where they were at the level of 0.2 kPa to 1.0 kPa, dependent on the inlet velocity profile and the geometry of the vasculature. For the healthy anatomical valve, similar results were achieved in [63,151,167], where [167] reported maximum TPG equal 792 Pa. During calcification, the calculated maximum pressure drop drastically increases, in the anatomical valve, in the range of 1.72 to 3.57 times (comparable values in [161, 167]).

For the healthy artificial valve, the highest pressure drops are observed during the time when the valve is not yet opened, and the inflow is rising, i.e., 0.00 s-0.07 s, as presented in Fig.5.14B. With the ongoing calcification process, this peak TPG moves

towards the moment of the highest inflow, as it is observed for anatomical valve during all calcification stages. During the 2nd stage (table 5.1), the peak is already visible in the maximum inflow time. As noted in Geometry section and table 5.1, the bileaflet valve calcification process for the 1st, 2nd and 3rd stages was modeled by obstructing the flow, and thus also leaflets range of motion. There, the pressure drop peak increased from 1.12 (2nd stage) to 2.96 times (3rd stage). Therefore, the increase in peak value was not substantial for the mild bileaflet valve calcification, of 5.3% flow and 8° leaflet motion obstruction; however, the mean systolic TPG increased by 108% (Fig.5.14C). For the severe calcification, both anatomical and artificial valve presents similar TPG increase. The 4th calcification stage of bileaflet valve was realized by also blocking one of its leaflet, at closed state, during the whole heart cycle. There, the pressure drop drastically increased, with the peak value of 6950 Pa, meaning 10.2 times increase compared with the model without leaflet blocking. In research [83], the measurements of calcified artificial valve were performed, and for the bileaflet valve with similar flow conditions and valve leaflet obstructions, 10.1 times increase was observed by turbulence-based pressure drop measurement.

The mean systolic TPG values are presented in figure 5.14C. For the anatomical valve, the TPG change rate slows down with the applied Young modulus, where in the anatomical valve, the change rate increases with progressive flow obstruction.

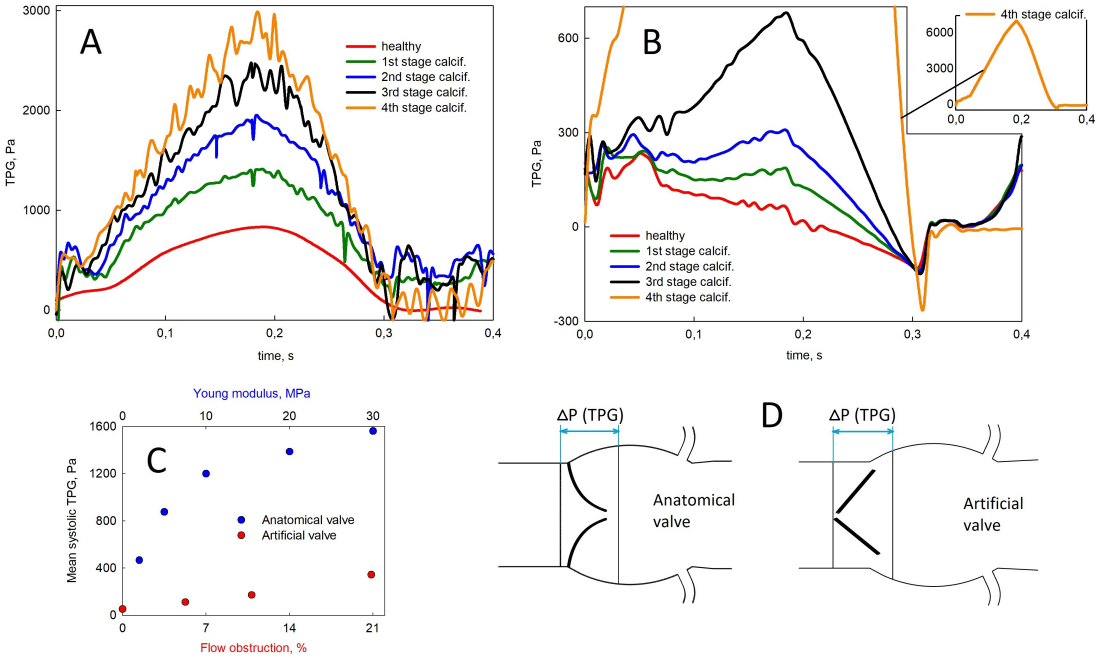

Figure 5.14: **A**: Transvalvular pressure gradient determined for the anatomical valve, **B**: TPG for the bileaflet mechanical valve, **C**: mean systolic TPG, **D**: location of the surfaces used for the TPG determination

The velocity pathlines for the healthy valves are shown in Fig. 5.15 for five different time instants: *early systole* (0.07 s), *maximum inflow* (0.185 s), *late systole* (0.27 s), *maximum reversed flow* (0.321 s) and *diastole* (0.45 s). Very similar velocity values are observed for both valves. For all time stamps, the artificial valve presents three-jet flow, typical for this type of implant. Also, the flow field is more regular, as the vortical structures are present in smaller region, which results from the human valve sinus area blocked by the curvy leaflet from the ventricular side. In particular, for maximum inflow, a singular vortex can be observed in the sinus for the bileaflet valve, where two main vortices are present in the anatomical valve. Vortices in the recirculation zone are also caused by the presence of the coronary arteries. The reversed flow causes swirl production in the whole root region depicted in Fig. 5.4. Despite small reversed flow, the bileaflet valve is fully closed at time 0.42 s (compare Fig. 5.13B) which can be observed at the moment *diastole*, where the flexible valve also closes, but without any flow gap remaining. The irregular flow structures in the vicinity of the valve caused oscillations in the valve deformation (flexible) and angular position (bileaflet type) oscillations (compare figures 5.13 (A and B)). Vortices grow in size as the valves close,

and their location moves towards the ventricular side. During the closure and closed state, blood flows into the coronary arteries to perfuse the myocardium, which is stated by increasing the velocity in the coronary regions.

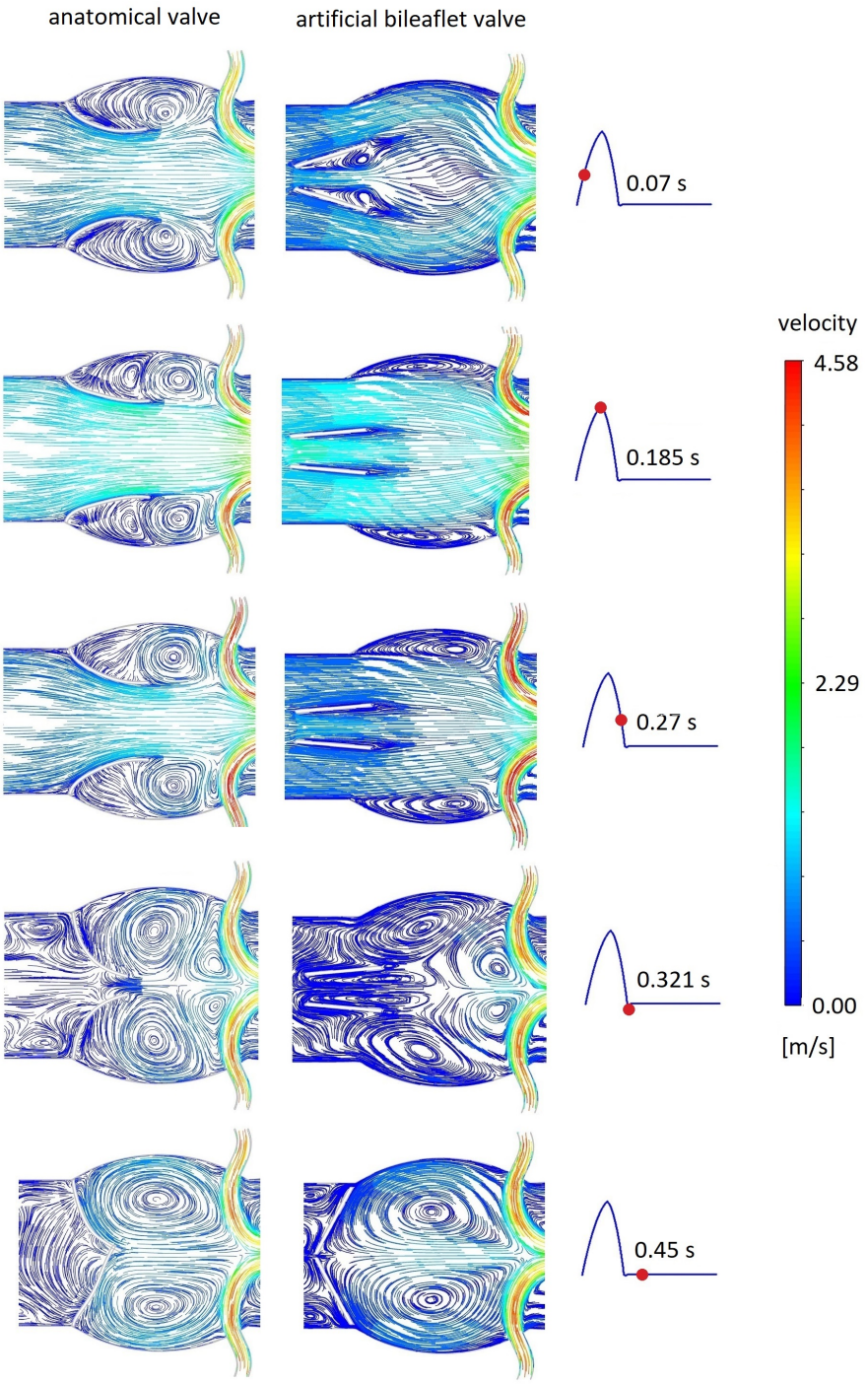

Figure 5.15: Velocity pathlines presented for the healthy anatomical and artificial valve vicinity

The pressure contours at the peak systole (0.185 s) are presented in Fig. 5.16. Both anatomical and bileaflet valve present similar pattern in terms of increasing pressure gradient with progressive calcification. This results from the decrease in the opening of the anatomical valve and the increase in the area of plaque of arteriolosclerosis. Furthermore, similar levels of pressure values are observed, except for the 4^{th} calcification stage of the bileaflet valve (Table 5.1), where due to the upper leaflet sticking to the plaque, a maximum pressure of 15.1 kPa was achieved. The calcification process lowers the minimum pressure value on the aortic side, which is connected to obstruction of the blood flow of the circulatory system. The process of compensation may arise, where hyperthrophy of the left ventricle occurs and heart failure may ensue [63].

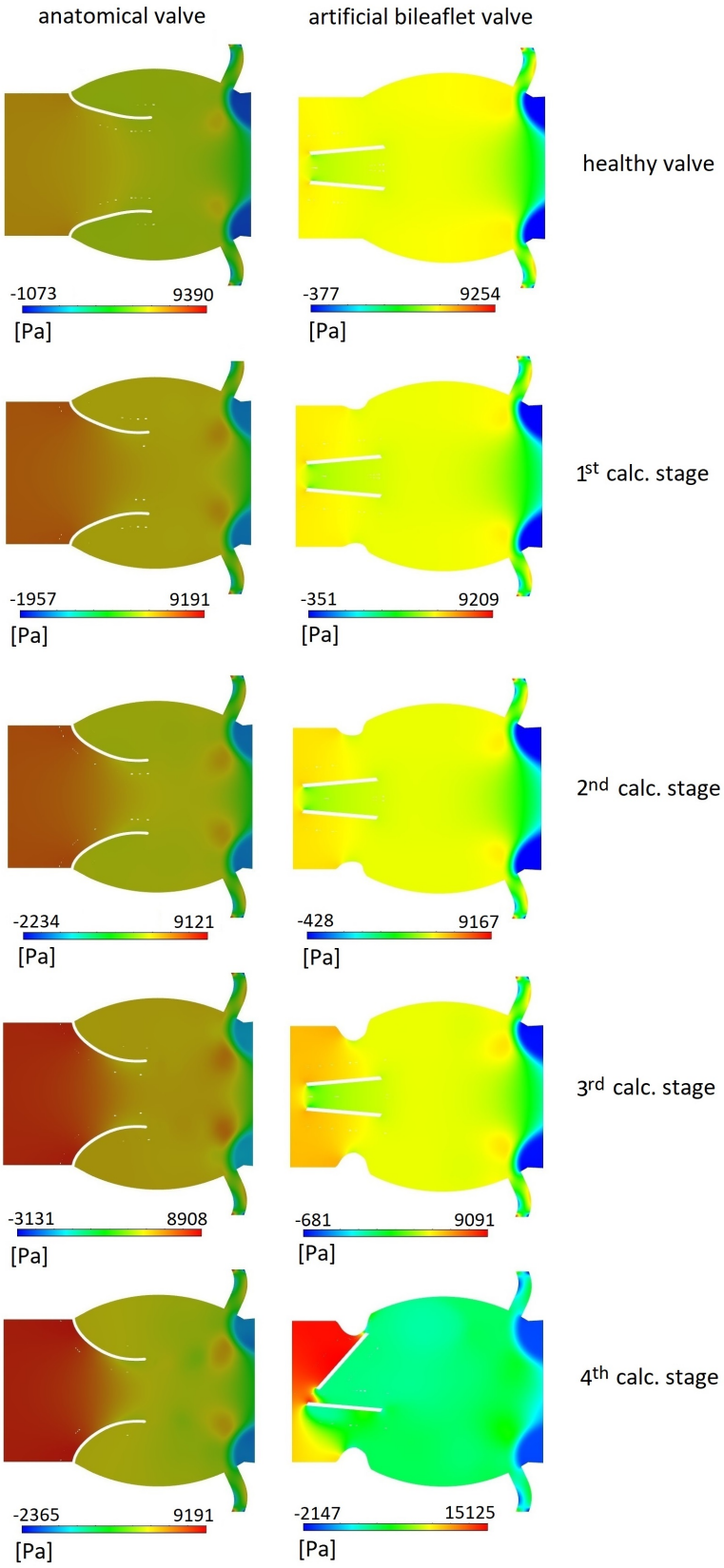

Figure 5.16: Peak systole pressure contour, presented for the anatomical and artificial valve vicinity, for all calcification stages

The average WSS exerted on the leaflets, for the anatomical and artificial mechanical valve is presented in Fig. 5.17. Progressive calcification causes an increase in the mean WSS values for both valve types, and also the rate of such an increase is very similar between the human and artificial valves. Average WSS values are generally very slightly higher for the bileaflet valve, however, at the beginning of the heart cycle, the peak in WSS values is observed for the implanted bileaflet valve. This regularity is not present for the anatomical valve. This is caused by the closed artificial valve leaflets, which lead to a high local velocity in the small gaps' vicinity (central gap between the leaflets and peripheral leaflet-blood wall gaps). When the leaflets open, the WSS average values rapidly decrease. For the 4^{th} calcification stage of the implanted valve (table 5.1), the great increase in the WSS values was observed, which is caused by blocking the upper leaflet and the maximum velocity flowing onto a closed, sharp surface (compare Fig. 5.16 for the 4^{th} stage).

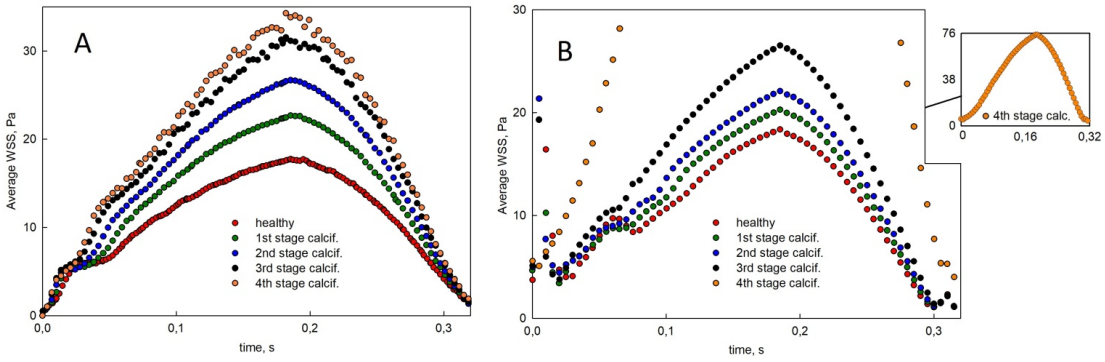

Figure 5.17: Average wall shear stress exerted on the leaflets walls, for the anatomical (**A**) and artificial (**B**) valve

The calcification of the aortic valve has its effect on the vortices location, shape and magnitude. For the healthy valve, the flow field was presented in Fig. 5.15. The vortex formation has its effect on hemodynamics in the coronary arteries, which was quantified by the determination of the vorticity magnitude in the point close to the upper coronary inlet, as presented in Fig.5.18. The increase in vorticity strength causes more energy loss, which is associated with stagnation of blood flow and increased probability of calcium deposition, as discussed in [63]. It is observed that the calcification process increases the vorticity magnitude for the anatomical valve by several percents,

where in the case of the artificial bileaflet valve a progressive decrease by about 3% per each calcification stage is noticed. The higher stenosis impact on coronary vorticity is for the bileaflet valve, however the healthy bileaflet valve presented higher vorticity magnitude on the level of 2500 rad/s, where for the human valve, values on the level of 2000 rad/s were observed. The increase is noticed mailny from the moment when the inlet velocity declines (0.185 s). Calcification causes vorticity fluctuations in the coronary vicinity, only in the case of the anatomical valve, which may be caused by more regular, three-jet flow through the artificial valve. Moreover, the vortex structures in human valve vicinity occupy more space and change their locations faster, wchich can be noticed in Fig. 5.15 and Appendix videos.

Blocking of the upper mechanical valve leaflet during its closed state (4^{th} stage, Table 5.1) caused a great decline in vorticity located in the upper coronary vicinity, as the flow becomes more unsymmetric and the greater part of the blood flows through the lower part of the vasculature.

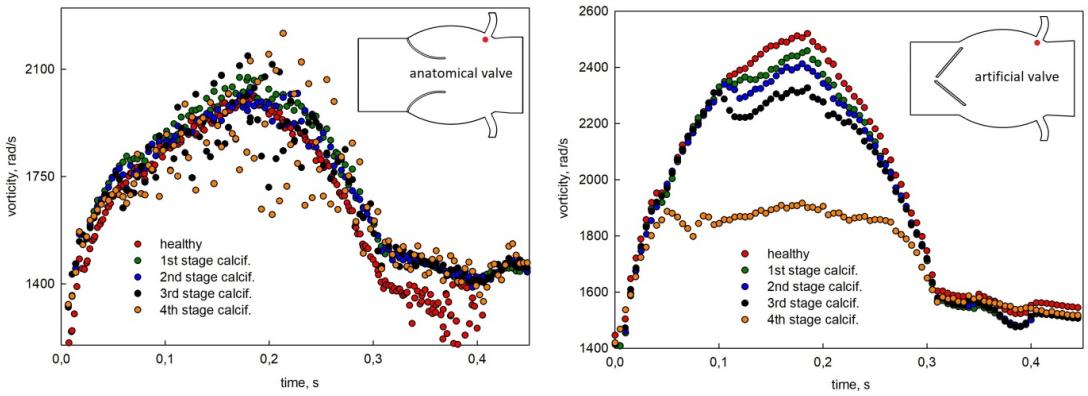

Figure 5.18: Vorticity magnitude in the upper coronary location shown at the insets, determined for the anatomical and artificial valve

The supplementary video materials can be found using the above QR code or the following link:
https://www.youtube.com/playlist?list=PLm0c-zXrCqEI-gLS0E-ta2EM0Bugf7cxS

Chapter 6

Discussion and conclusions

The thesis presents the development of numerical models for the modeling of artificial and anatomical heart valves, applying to rigid and deformable. The comprehensive analysis was performed for accurate, robust, stable, and time-efficient computations, which included selection of an efficient computational strategy, development of an in-house model for modeling fluid-structure interaction, and definition of the geometry, mesh, and proper timestep size of the solution procedure. The in-house model was dedicated for the accurate time discretization control in the transient model, for efficient and reliable application of the moving mesh modules. All mentioned aspects characterized the numerical model in the case of its usage for clinical diagnosed trials, in consideration to support the patient examination, for example for virtual therapies.

The numerical models considering bileaflet valve were validated using inhouse test rig measurements, with dedicated Labview application. The test rig setup and data processing was described in Chapter 4., with the protocol for determining the leaflet angle from the fast camera images. Beside the measurements, the models results were validated against the data from the patients examination available in literature, that included the echocardiography, PIV, flow and pressure measurements, valve leaflet shapes, with the conclusion that developed models present physiological values, and agreed very well to those measured in the dedicated test rig.

The Ph.D. thesis begins with the application of CFD solver and imposed motion, for the study of the bileaflet mechanical valve implanted in an anatomic geometry. This included the aortic root, ascending and descending aorta and aortic arch with its major

branches. The Windkessel model for outflows based on the electrical analogy was implemented, to determine the time-varying pressure and mass flow values. The results were also compared for the truncated geometry and simpler outlet boundary condition of 0 Pa gauge pressure. The results of two different RANS turbulence models (k-ε, k-ω) as well as laminar model, were compared with the validation data in literature, with the conclusion that for the aortic valve the model k-ε performs best, therefore it was used in the subsequent works. The geometry acquisition approaches and realization of the overset mesh in the case of more challenging applications, such as when very small gaps and a moving domain occurs, was described. The guidelines for the proper domain discretization for the overset meshing were introduced. The most difficult part of such meshing preparation, was remaining the similar cell sizes between the background and component meshes, especially in the small gap regions. This moving mesh module proved to be a very stable, efficient and reliable mesh update strategy, for aortic valve modeling. The simulation results were validated against the measurement data available in the literature, in terms of TKE, pressure drop, EOA, WSS and Reynolds number values, and compared with additionally created model excluding the valve. The results indicated the proper work of the artificial valve in the patient's circulatory system. Moreover, including valve geometry and motion in the modeling was recognized as necessary, if the close-to-valve aortic region is considered, to properly model the blood flow character. Some typical phenomena for mechanical bileaflet valves are present, such as the negative pressure transients and high shear stresses, that could effect in the cavitation bubbles or the blood cells lysis, accordingly. However, at this stage such phenomena were not implemented to the solver, which is planned to be realized in the future work.

The knowledge gained by the bileaflet valve modeling with the imposed motion approach, was used to expand the model, by in-house approach for FSI. Therefore, the motion of the structures rotating by the influence of fluid flow, as one-, two- or three-leaflet artificial valve, could be solved by introduced model, implemented by UDFs and Fluent journal files within the solution procedure. Two different moving mesh modules: overset mesh and dynamic mesh, were used and compared, in terms of results, stability, allowable rotations per timestep, reliability and possible errors. Such

comparison for artificial valves was not previously published. The model was realized in terms of 6DOF rigid body motion. The novel approach for dynamic timestep sizing was here used and described, with analysis of how the different values of the model constant can influence onto solving time and moving mesh operation. Implementation of the module calculating timestep size appropriate to the determined leaflet velocity improved considerably the solver stability, moving mesh operation, and significantly reduced solving time by 72%. The overset mesh approach turned out to perform better in terms of computational efficiency, as the smaller rotations per single timestep were demanded for the dynamic mesh module used instead. Moreover, the dynamic mesh demanded creation of the new numerical mesh every time when the motion was registered, which was the time-consuming process. Nevertheless, very similar results were achieved with both approaches for moving mesh. The simulation results were validated with test rig measurements including real valve prosthesis, pulsatile blood pump, pressure transducers, mass flow meter and fast camera. The measurements were performed with dedicated inhouse Labview® application. The fast camera images were processed for the valve angular positions determination with usage of prepared application in Python OpenCV environment. Similar application for the elastic valve, i.e. for determination of the valve opening, was developed and described in Chapter 5, which was used to process the images gained from numerical results. In the future, the test rig measurement of the deformable valve used in the transcatheter aortic valve replacement will be performed, and the camera images will be processes using already developed OpenCV algorithm. The multivariant analysis considering the 6DOF model constant - momentum of inertia, was performed. The model proved to be quite insensitive on momentum of inertia error, cause the value change on the level of ±40% did not influence significantly onto the valve leaflets angular motion, also even with less impact on other CFD characteristics. The CFD results and determined valve indicators shown a proper valve operation, confirming the conclusions made based on the real arterial geometry model with virtually implanted valve.

The approach for modeling deformable valve prostheses was also recognized and implemented, both for the 2D and 3D elastic valve model. The author experience [23] of the arterial flow FSI modeling was transferred to the flow-around modeling of the

deformable valve. Using the remarks made on the moving mesh approach for the rigid valve and flexible aorta, the novel approach combining two modules, namely dynamic mesh and overset mesh, was applied for the flexible leaflets structure, which improved considerably the moving mesh quality, solver stability, boundary layer resolving and solving time. The procedure for using such coupled meshing module was described, both for the 2D and 3D geometries, along with the mesh testing procedure omitting flow and structural field resolving. The partitioned FSI approach combining the fluid and mechanical solver, was used for the anatomical valve, where to compare its operation with the prosthesis, the validated 6DOF model was successfully applied for the bileaflet valve. The flexible valve model demanded tremendous computational resources, therefore the full 3D geometrical model was reduced to 2D approach. However, the opportunities for solving the model in 3D coordinates were recognized. This will demand the modeling of only 1/6 of the geometry, as the elastic valve consists of the three identical, symmetrical structures, also the further focus on the limiting the number of structural mesh elements will be done in the future research. The impact of progressive calcification on valve performance was assessed, both for the anatomical and mechanical valve; the latter was not previously investigated in the literature. The simpler linearly-elastic (Hookean) solid model was compared with the hyperelastic solid structure; however, the latter was not used in the results analysis, as the calcification modeling was realized more conveniently based on the two-constant Hookean model. Nevertheless, further work will be performed towards retrieving the material constants and hyperelastic solid modeling, as the valve is a multilayer structure with properties changing in space. The opportunity is seen in usage of the AI model with the series of 3D FSI calculations combined with experimental or medical validation data set, where the material constants are varying in space, especially with the leaflet layers.

The declining inflow rate provoked anatomical valve closing for all the calcification stages, where the reversed flow have to be present to provoke the mechanical bileaflet valve closing. Similar opening and closing times are determined for the human and artificial valve. Slight fluctuations in terms of the rigid leaflets angular position and flexible leaflets deformations are present during the valve opening and closing phases.

Based on numerical model results, calcification of the human aortic valve change its kinematics more in terms of the maximum opening (35.9% decrease for the severe calcification), than for the maximum closing (approximately equal 5% decreases in closing for all calcification stages). The healthy artificial valve causes less maximal pressure drop (240 Pa) than the anatomical valve (850 Pa). TPG values rised due to valves calcification. The eddy structures are more prominent for the anatomical valve due to its curved leaflet shape. The bileaflet valve produces regular, three-jet flow, however vorticity is still present, especially in the sinus regions, starting from the moment when the velocity decreases. Blocking of the one mechanical valve leaflet, at its closed state, caused by sticking to the arteriolosclerosis plaque, provoked several time increase in the TPG and WSS values exerted on leaflet wall. Slightly higher WSS values were noticed for the bileaflet valve, WSS values rise due to the stenosis. The stenosis increases the vorticity magnitude for the anatomical valve by several percents, where for the mechanical valve a progressive decrease by about 3% per each calcification stage is noticed.

6.1 Future research

As indicated in the review of the literature and based on the conducted research, there is still room for improvement in terms of the artificial valve design, both for rigid and deformable valves. The construction should overcome drawbacks in terms of the possible high shear stresses causing blood cell lysis, high rotational speed that may cause cavitation bubbles, high pressure drops and resulting flow obstruction, durability problem of the elastic valves, also its interaction to the blood walls and overall circulatory system. The developed 6DOF-FSI and FSI validated models can be successfully used in multivariant analyzes, which will support the decision-making process on the best design for the specific patient's conditions. The parameters related to the geometry, influencing the valve operation, are for example the leaflet length (rigid and deformable valves), angular position limitations and location of the rotation center (rigid valve), number of leaflets, leaflet thickness, and material properties. The impact of these parameters values onto prosthesis operation will be analyzed in the future work.

The artificial intelligence is a tool that could be implemented along with the multivatiant numerical analysis, to select the prosthesis design in a fast way, that will fulfill mentioned requirements. Also, implementation of the hemolysis and the Euler-Euler multiphase model [26] will help to understand the interaction between the moving structures in the cardiovascular system and the blood cells. Along with the numerical models, the experiments are possible to be performed with the usage of described laboratory test rig, located in the Institute of Thermal Technology. Furthermore, the calcification mechanisms and their interaction with the anatomical and artificial valves are not fully recognized, therefore additional work should be performed with the approach used in Chapter 5. and the series of patients examination data.

The open-source solvers, as OOMPH-LIB [168] or OpenFOAM [48, 169] could be easier to implement for the clinician purposes as no license fees are needed, therefore their testing, validation and comparison with the commercial Ansys software results seems reasonable. Also, the monolithic approaches, along with the ALE or IBM solvers are seen as more stable, and probably more time-efficient, then the partitioned FSI. Thus the effort will be made to gain knowledge and perform numerical modeling using such approaches. Furthermore, the structural-only approach [73, 81], limited to specific conditions, may be useful to model 3D valve leaflets, for example to retrieve their material properties. Lastly, the reduced order models creation, for example to determine the pressure drop and blood cell lysis based on the valve construction and patient physiological data, will be the easiest way to implement the modeling, towards the clinician use.

Bibliography

[1] E. Wilkins, L. Wilson, K. Wickramasinghe, P. Bhatnagar, J. Leal, R. Luengo-Fernandez, R. Burns, M. Rayner, and N. Townsend, "European Cardiovascular Disease Statistics 2017 edition," *European Heart Network*, 2017.

[2] D. B. J. Hoskins Peter R., Lawford Patricia V., *Cardiovascular Biomechanics*. Springer, 2017.

[3] K. Cao, S. K. Atkins, A. McNally, J. Liu, and P. Sucosky, "Simulations of morphotype-dependent hemodynamics in non-dilated bicuspid aortic valve aortas," *Journal of Biomechanics*, vol. 50, 2017. Biofluid mechanics of multitude pathways: From cellular to organ.

[4] A. M. Tango, A. Ducci, and G. Burriesci, "In silico study of the ageing effect upon aortic valves," *Journal of Fluids and Structures*, vol. 103, p. 103258, 2021.

[5] C. Otto, I. Burwash, M. Legget, B. Munt, M. Fujioka, N. Healy, C. Kraft, C. Miyake-Hull, and R. Schwaegler, "Prospective study of asymptomatic valvular aortic stenosis. clinical, echocardiographic, and exercise predictors of outcome," *Circilation*, vol. 95, no. 9, 1997.

[6] J. Lincoln and P. Dutta, "Calcific aortic valve disease: a developmental biology perspective," *Current Cardiology Reports*, vol. 20, no. 21, 2018.

[7] E. Qiao, Z. Huang, and W. Wang, "Exploring potential genes and pathways related to calcific aortic valve disease," *Gene*, vol. 808, p. 145987, 2022.

[8] C. Wang, Y. Zhang, M. Methawasin, C. U. Braz, J. Gao-Hu, B. Yang, J. Strom, J. Gohlke, T. Hacker, H. Khatib, H. Granzier, and W. Guo, "Rbm20s639g muta-

tion is a high genetic risk factor for premature death through rna-protein condensates," *Journal of Molecular and Cellular Cardiology*, vol. 165, pp. 115–129, 2022.

[9] T. Abe, K. Kamata, K. Kuwaki, K. Komatsu, and S. Komatsu, "Ten years' experience of aortic valve replacement with the omnicarbon valve prosthesis," *Annals of Thoracic Surgery*, vol. 61, no. 4, pp. 1182–1187, 1996.

[10] J. D. B. et al., *The Biomedical Engineering HandBook, Second Edition.* CRC Press LLC, 2000.

[11] "Medtronic® open pivot; instructions for use."

[12] R. J. Gray, A. Chaux, J. M. Matloff, M. DeRobertis, M. Raymond, M. Stewart, and A. Yoganathan, "Bileaflet, tilting disc and porcine aortic valve substitutes: In vivo hydrodynamic characteristics," *Journal of the American College of Cardiology*, vol. 3, no. 2, pp. 321–327, 1984.

[13] E. G. C. Emiliano Votta, Trung Bao Le, Marco Stevanella, Laura Fusini, Alberto Redaelli, and F. Sotiropoulos, "Toward patient-specific simulations of cardiac valves: state-of- the-art and future directions," vol. 46, no. 2, pp. 217–228, 2013.

[14] H. Hatoum, S. Ahn, S. Lilly, P. Maureira, J. Crestanello, V. H. Thourani, and L. P. Dasi, "Flow dynamics of surgical and transcatheter aortic valves: Past to present," *JTCVS Open*, vol. 9, pp. 43–56, 2022.

[15] R. Mittal, J. Seo, V. Vedula, Y. Choi, H. Liu, H. Huang, S. Jain, L. Younes, T. Abraham, and R. George, "Computational modeling of cardiac hemodynamics: Current status and future outlook, journal of computational physics," *Journal of Computational Physics*, vol. 305, p. 1065–1082, 2016.

[16] S. Doost, L. Zhong, B. Su, and Y. Morsi, "The numerical analysis of non-newtonian blood flow in human patient-specific left ventricle," *Computer Methods and Programs in Biomedicine*, vol. 127, pp. 323–247, 2016.

[17] M. Nobili, U. Morbiducci, R. Ponzini, C. Gaudio, A. Balducci, M. Grigioni, F. Montevecchi, and A. Redaelli, "Numerical simulation of the dynamics of a bileaflet prosthetic heart valve using a fluid–structure interaction approach," *Journal of Biomechanics*, vol. 41, pp. 2539–2550, 2008.

[18] H. Baumgartner, V. Falk, and et al., "2017 esc/eacts guidelines for the management of valvular heart disease," *European Heart Journal*, no. 38, 2017.

[19] R. Smith-Bindman, "Is computed tomography safe," *The New England Journal of Medicine*, vol. 363, no. 1, pp. 1–4, 2010.

[20] R. Smith-Bindman, D. Miglioretti, E. Johnson, C. Lee, H. Feigelson, M. Flynn, R. Greenlee, R. Kruger, M. Hornbrook, D. Roblin, and et al., "Use of diagnostic imaging studies and associated radiation exposure for patients enrolled in large integrated health care systems," *Journal of the American Medical Association*, vol. 307, no. 22, p. 2400–2409, 2012.

[21] C. Storrs, "How much do ct scans increase the risk of cancer," *Scientific American*, vol. 209, no. 1, p. 2400–2409, 2013.

[22] G. P. Chatzimavroudis, "Blood flow measurements with magnetic resonance phase velocity mapping," *Measurement*, vol. 37, 2005.

[23] M. Nowak, B. Melka, M. Rojczyk, M. Gracka, A. J. Nowak, A. Golda, W. P. Adamczyk, B. Isaac, R. A. Białecki, and Z. Ostrowski, "The protocol for using elastic wall model in modeling blood flow within human artery," *European Journal of Mechanics - B/Fluids*, vol. 77, pp. 273–280, 2019.

[24] 3D Systems, "Geomagic."

[25] B. Melka, M. Nowak, M. Rojczyk, M. Gracka, W. Adamczyk, Z. Ostrowski, and R. Bialecki, "Flow in a Myocardial Bridge Region of a Coronary Artery- Experimental Rig and Numerical Model," *Information Technology in Biomedicine*, no. 1186, 2020.

[26] B. Melka, W. Adamczyk, M. Rojczyk, M. Gracka, A. Nowak, A. Golda, R. Bialecki, and Z. Ostrowski, "Numerical investigation of multiphase blood flow coupled with lumped parameter model of outflow," *International Journal of Numerical Methods for Heat and Fluid Flow*, 2020.

[27] A. Widuch, K. Myöhänen, M. Nikku, M. Nowak, A. Klimanek, and W. Adamczyk, "Data set generation at novel test-rig for validation of numerical models for modeling granular flows," *International Journal of Multiphase Flow*, vol. 142, 2021.

[28] A. Widuch, M. Nowak, D. Sukiennik, K. Myöhänen, M. Nikku, S. Shah, A. Parente, and W. Adamczyk, "Towards application of uncertainty quantification procedure combined with experimental procedure for assessment of the accuracy of the dem approach dedicated for granular flow modeling," *Powder Technology*, vol. 399, 2022.

[29] S. J. Benek JA, Buning PG, "A 3-D Chimera grid embedding technique.," *AIAA seventh CFD conference, Cincinnati, OH. AIAA paper 85-1523*, 1985.

[30] J. M. Zhan, W. H. Cai, W. Q. Hu, Y. J. Gong, and T. Z. Li, "Numerical study on the six-DOF anchoring process of gravity anchor using a new mesh update strategy," *Marine Structures*, vol. 52, pp. 173–187, 2017.

[31] S. T. Miller, R. L. Campbell, C. W. Elsworth, J. S. Pitt, and D. A. Boger, "An Overset Grid Method for Fluid-Structure Interaction," *World Journal of Mechanics*, vol. 04, no. 07, pp. 217–237, 2014.

[32] W. A. Wall, P. Gamnitzer, and A. Gerstenberger, "Fluid–structure interaction approaches on fixed grids based on two different domain decomposition ideas," *International Journal of Computational Fluid Dynamics*, vol. 22, no. 6, pp. 411–427, 2008.

[33] F. White, *Fluid Mechanics*. McGraw-Hill,New York, 2010.

[34] P. D. Morris, A. Narracott, H. von Tengg-Kobligk, D. A. Silva Soto, S. Hsiao, A. Lungu, P. Evans, N. W. Bressloff, P. V. Lawford, D. R. Hose, and J. P. Gunn,

"Computational fluid dynamics modelling in cardiovascular medicine.," *Heart*, pp. heartjnl–2015–308044–, 2015.

[35] D. Sankar and K. Hemalatha, "A non-Newtonian fluid flow model for blood flow through a catheterized artery-Steady flow," *Applied Mathematical Modelling*, vol. 31, no. 9, pp. 1847–1864, 2007.

[36] Y. I. Cho and K. R. Kensey, "Effects of the non-Newtonian viscosity of blood on flows in a diseased arterial vessel. Part 1: Steady flows.," *Biorheology*, vol. 28, no. September, pp. 241–262, 1991.

[37] A. Tango, J. Salmonsmith, A. Ducci, and G. Burriesci, "Validation and extension of a fluid-structure interaction model of the healthy aortic valve," *Cardiovascular Engineering and Technology*, no. 9, 2019.

[38] K. Cao, M. BukaČ, and P. Sucosky, "Three-dimensional macro-scale assessment of regional and temporal wall shear stress characteristics on aortic valve leaflets," *Computer Methods in Biomechanics and Biomedical Engineering*, vol. 19, no. 6, 2016.

[39] U. Gulbulak, O. Gecgel, and A. Ertas, "A deep learning application to approximate the geometric orifice and coaptation areas of the polymeric heart valves under time – varying transvalvular pressure," *Journal of the Mechanical Behavior of Biomedical Materials*, vol. 117, p. 104371, 2021.

[40] J. D. Humphrey, *Cardiovascular solid mechanics*. Springer Science and business media, 2002.

[41] B. H.J., S. M., and et al, *Fluid-Structure Interaction. Modelling, simulation, optimization*. Springer Science and business media, 2006.

[42] M. Alishahi, M. M. Alishahi, and H. Emdad, "Numerical simulation of blood flow in a flexible stenosed abdominal real aorta," *Scientia Iranica*, vol. 18, no. 6, pp. 1297–1305, 2011.

[43] P. Stradins, R. Lacis, I. Ozolanta, B. Purina, V. Ose, L. Feldmane, and V. Kasyanov, "Comparison of biomechanical and structural properties between human aortic and pulmonary valve," *European Journal of Cardio-Thoracic Surgery*, vol. 26, pp. 634–639, 09 2004.

[44] A. I. Hassaballah, M. A. Hassan, A. N. Mardi, and M. Hamdi, "An inverse finite element method for determining the tissue compressibility of human left ventricular wall during the cardiac cycle," *PLOS ONE*, vol. 8, 12 2013.

[45] H. Versteeg and W. Malalasekera, *Introduction to Computational Fluid Dynamics*, vol. 44. 2005.

[46] A. Amindari, L. Saltik, K. Kirkkopru, M. Yacoub, and H. Yalcin, "Assessment of calcified aortic valve leaflet deformations and blood flow dynamics using fluid-structure interaction modeling," *Informatics in Medicine Unlocked*, vol. 9, no. 0, pp. 191–199, 2017.

[47] Y. Imai, T. Omori, Y. Shimogonya, T. Yamaguchi, and T. Ishikawa, "Numerical methods for simulating blood flow at macro, micro, and multi scales," *Journal of Biomechanics*, vol. 49, pp. 2221–2228, 2016.

[48] K. G. Lyras and J. Lee, "Comparison of numerical implementations for modelling flow through arterial stenoses," *International Journal of Mechanical Sciences*, vol. 211, p. 106780, 2021.

[49] D. Lopes, R. Agujetas, H. Puga, J. Teixeira, R. Lima, J. Alejo, and C. Ferrera, "Analysis of finite element and finite volume methods for fluid-structure interaction simulation of blood flow in a real stenosed artery," *International Journal of Mechanical Sciences*, vol. 207, p. 106650, 2021.

[50] W. Jeong and J. Seong, "Comparison of effects on technical variances of computational fluid dynamics (cfd) software based on finite element and finite volume methods," *International Journal of Mechanical Sciences*, vol. 78, pp. 19–26, 2014.

[51] Łukasz Marzec, Z. Buliński, and T. Krysiński, "Fluid structure interaction analysis of the operating savonius wind turbine," *Renewable Energy*, vol. 164, pp. 272–284, 2021.

[52] D. Lopes, H. Puga, J. Teixeira, and S. Teixeira, "Influence of arterial mechanical properties on carotid blood flow: Comparison of cfd and fsi studies," *International Journal of Mechanical Sciences*, vol. 160, pp. 209–218, 2019.

[53] C. Chnafa, S. Mendez, and F. Nicoud, "Image-based large-eddy simulation in a realistic left heart," *Computers & Fluids*, vol. 94, pp. 173–187, 2014.

[54] Z. Li, G. Oger, and D. Le Touzé, "A partitioned framework for coupling lbm and fem through an implicit ibm allowing non-conforming time-steps: Application to fluid-structure interaction in biomechanics," *Journal of Computational Physics*, vol. 449, p. 110786, 2022.

[55] T. B. Le and F. Sotiropoulos, "Fluid-structure interaction of an aortic heart valve prosthesis driven by an animated anatomic left ventricle," *Journal of Computational Physics*, vol. 244, pp. 41–62, 2013.

[56] L. Yanhong, "A lattice Boltzmann model for blood flows," *Applied Mathematical Modelling*, vol. 36, no. 7, pp. 2890–2899, 2012.

[57] R. Sadeghi, N. Gasner, S. Khodaei, J. Garcia, and Z. Keshavarz-Motamed, "Impact of mixed valvular disease on coarctation hemodynamics using patient-specific lumped parameter and lattice boltzmann modeling," *International Journal of Mechanical Sciences*, vol. 217, p. 107038, 2022.

[58] J. H. Lee and B. E. Griffith, "On the lagrangian-eulerian coupling in the immersed finite element/difference method," *Journal of Computational Physics*, vol. 457, p. 111042, 2022.

[59] *ANSYS® Academic Research, Release 17.2, Help System, ANSYS, Inc.*

[60] M. Grigioni, C. Daniele, C. Del Gaudio, U. Morbiducci, and A. Balducci, "Three-dimensional numerical simulation of flow through an aortic bileaflet valve in a realistic model of aortic root," *Asaio Journal*, vol. 51, 2005.

[61] A. V. L. Formaggia, A. Quarteroni, *Cardiovascular Mathematics*. 2009.

[62] A. R. Kivi, N. Sedaghatizadeh, B. S. Cazzolato, A. C. Zander, A. J. Nelson, R. Roberts-Thomson, A. Yoganathan, and M. Arjomandi, "Hemodynamics of a stenosed aortic valve: Effects of the geometry of the sinuses and the positions of the coronary ostia," *International Journal of Mechanical Sciences*, vol. 188, p. 106015, 2020.

[63] A. R. Kivi, N. Sedaghatizadeh, B. S. Cazzolato, A. C. Zander, R. Roberts-Thomson, A. J. Nelson, and M. Arjomandi, "Fluid structure interaction modelling of aortic valve stenosis: Effects of valve calcification on coronary artery flow and aortic root hemodynamics," *Computer Methods and Programs in Biomedicine*, vol. 196, p. 105647, 2020.

[64] A. Arzani and M. R. Mofrad, "A strain-based finite element model for calcification progression in aortic valves," *Journal of Biomechanics*, vol. 65, pp. 216–220, 2017.

[65] M. Loureiro-Ga, C. Veiga, G. Fdez-Manin, F. Calvo-Iglesias, V. Alfonso Jimenez, P. Pazos, and A. Iñiguez, "Including coronary ostia in patient-specific 3d models of the whole aortic valve apparatus, derived from tee, for biomechanical simulations," *International Journal of Multiphysics*, vol. 15, no. 1, 2021.

[66] Comsol multiphysics software *online: https://www.comsol.com/comsol-multiphysics*.

[67] S. Khodaei, R. Sadeghi, P. Blanke, J. Leipsic, A. Emadi, and Z. Keshavarz-Motamed, "Towards a non-invasive computational diagnostic framework for personalized cardiology of transcatheter aortic valve replacement in interactions with complex valvular, ventricular and vascular disease," *International Journal of Mechanical Sciences*, vol. 202-203, p. 106506, 2021.

[68] M. Amir, A. Y. Usmani, M. Varshney, S. F. Anwer, S. A. Khan, N. Islam, and A. A. Pasha, "Analysing spatio-temporal flow hemodynamics in an artery

manifesting stenosis," *International Journal of Mechanical Sciences*, vol. 218, p. 107072, 2022.

[69] S. Sandeep and S. Shine, "Effect of stenosis and dilatation on the hemodynamic parameters associated with left coronary artery," *Computer Methods and Programs in Biomedicine*, vol. 204, p. 106052, 2021.

[70] Z. Wang, C. Wang, F. Zhao, N. Qi, D. Lockington, K. Ramaesh, P. S. Stewart, X. Luo, and H. Tang, "Simulation of fluid-structure interaction during the phaco-emulsification stage of cataract surgery," *International Journal of Mechanical Sciences*, vol. 214, p. 106931, 2022.

[71] M. S. Sadrabadi, M. Eskandari, H. P. Feigenbaum, and A. Arzani, "Local and global growth and remodeling in calcific aortic valve disease and aging," *Journal of Biomechanics*, vol. 128, p. 110773, 2021.

[72] R. Savabi, M. Nabaei, S. Farajollahi, and N. Fatouraee, "Fluid structure interaction modeling of aortic arch and carotid bifurcation as the location of baroreceptors," *International Journal of Mechanical Sciences*, vol. 165, p. 105222, 2020.

[73] W. Zhang, S. Motiwale, M.-C. Hsu, and M. S. Sacks, "Simulating the time evolving geometry, mechanical properties, and fibrous structure of bioprosthetic heart valve leaflets under cyclic loading," *Journal of the Mechanical Behavior of Biomedical Materials*, vol. 123, p. 104745, 2021.

[74] S. Jamaleddin Mousavi, R. Jayendiran, S. Farzaneh, S. Campisi, M. Viallon, P. Croisille, and S. Avril, "Coupling hemodynamics with mechanobiology in patient-specific computational models of ascending thoracic aortic aneurysms," *Computer Methods and Programs in Biomedicine*, vol. 205, p. 106107, 2021.

[75] H. Yeh, O. Barannyk, D. Grecov, and P. Oshkai, "The influence of hematocrit on the hemodynamics of artificial heart valve using fluid-structure interaction analysis," *Computers in Biology and Medicine*, vol. 110, 2019.

[76] L. Dasi, L. Ge, H. Simon, F. Sotiropoulos, and A. Yoganathan, "Vorticity dynamics of a bileaflet mechanical heart valve in an axisymmetric aorta," *Physics of fluids*, vol. 19, 2006.

[77] H. Ha, J. E. Kvitting, P. Dyverfeldt, and T. Ebbers, "4D Flow MRI quantification of blood flow patterns, turbulence and pressure drop in normal and stenotic prosthetic heart valves," *Magnetic Resonance Imaging*, vol. 55, 2019.

[78] M. D. De Tullio, G. Pedrizzetti, and R. Verzicco, "On the effect of aortic root geometry on the coronary entry-flow after a bileaflet mechanical heart valve implant: A numerical study," *Acta Mechanica*, vol. 216, no. 1-4, pp. 147–163, 2011.

[79] I. Borazjani, L. Ge, and F. Sotiropoulos, "High-resolution fluid-structure interaction simulations of flow through a bi-leaflet mechanical heart valve in an anatomic aorta," *Annals of Biomedical Engineering*, vol. 38, no. 2, pp. 326–344, 2010.

[80] Y. Bazilevs, K. Takizawa, and T. Tezduyar, *Computational Fluid-Structure Interaction*. Chichester, UK: John Wiley & Sons, Ltd, jan 2013.

[81] U. Gulbulak, O. Gecgel, and A. Ertas, "A deep learning application to approximate the geometric orifice and coaptation areas of the polymeric heart valves under time-varying transvalvular pressure," *Journal of the Mechanical Behavior of Biomedical Materials*, vol. 117, 2021.

[82] M. Said, E. Eppinga, N. Verweij, and P. der Harst, "Relationship of arterial stiffness index and pulse pressure with cardiovascular disease and mortality," *Cardiovascular Centre (CVC)*, no. 7, 2018.

[83] H. Ha, J.-P. E. Kvitting, P. Dyverfeldt, and T. Ebbers, "4d flow mri quantification of blood flow patterns, turbulence and pressure drop in normal and stenotic prosthetic heart valves," *Magnetic Resonance Imaging*, vol. 55, pp. 118–127, 2019.

[84] J. Vesey and C. Otto, "Complications of prosthetic heart valves," *Current Cardiology Reports*, no. 6, 2004.

[85] T. Tirilomis, "Acute thrombosis of mechanical bi-leaflet aortic valve prosthesis," *Journal of Cardiovascular Disease Research*, vol. 3, no. 3, pp. 228–230, 2012.

[86] A. Dahiya, J. Coucher, J. Pratap, and C. Cole, "Multiphase tavr ct identifies unexpected sticky situation (mechanical mitral valve leaflet dysfunction and bicuspid aortic valve)," *Journal of Cardiovascular Computed Tomography*, vol. 15, no. 3, 2021.

[87] J. H. Spühler, J. Jansson, N. Jansson, and J. Hoffman, "3d fluid-structure interaction simulation of aortic valves using a unified continuum ale fem model," *Frontiers in Physiology*, vol. 9, 2018.

[88] M. Cengel and Y. Cimbala, "Fluid Mechanics. Fundamentals and applications," *McGraw-Hill*, 2006.

[89] R. Mazzitelli, F. Boyle, E. Murphy, A. Renzulli, and G. Fragomeni, "Numerical prediction of the effect of aortic Left Ventricular Assist Device outflow-graft anastomosis location," *Biocybernetics and Biomedical Engineering*, vol. 36, no. 2, pp. 327–343, 2016.

[90] A. E., "Component–adaptive grid interfacing," *AIAA 19th aerospace sciences meeting*, 1981.

[91] D. F. Benek JA, Steger JL, "A flexible grid embedding technique with application to the Euler equations," *AIAA sixth CFD conference, Danvers, MA.*, 1983.

[92] S. N. Benek JA, Donegan TL, "Extended Chimera grid embedding scheme with application to viscous flows," *AIAA eighth CFD conference, Honolulu, HI. AIAA*, 1987.

[93] H. W. Chesshire G, "Composite overlapping meshes for the solution of partial differential equations," *J Comput Phys 1990;90:1–64*, 1990.

[94] H. Chen, L. Qian, Z. Ma, W. Bai, Y. Li, D. Causon, and C. Mingham, "Application of an overset mesh based numerical wave tank for modelling realistic free-surface hydrodynamic problems," *Ocean Engineering*, vol. 35, no. 176, 2019.

[95] T. J. Baker, "Mesh generation: Art or science?," *Progress in Aerospace Sciences*, vol. 41, no. 1, pp. 29–63, 2005.

[96] M. H. Yacoub and L. H. Cohn, "Novel Approaches to Cardiac Valve Repair. From Structure to Function: Part I," *Circulation*, vol. 109, no. 8, pp. 942–950, 2004.

[97] B. Launder and D. Spalding, "The numerical computation of turbulent flows," *Computer Methods in Applied Mechanics and Engineering*, no. 3, pp. 269–289, 1974.

[98] D. Wilcox, "Turbulence modeling for cfd," *DCW Industries Inc, United States*, 1998.

[99] A. Benim, A.Nahavandi, A. Assmann, D. Schubert, P. Feindt, and S. Suh, "Simulation of blood flow in human aorta with emphasis on outlet boundary conditions," *Applied Mathematical Modelling*, vol. 35, no. 7, pp. 3175–3188, 2011.

[100] N. Westerhof, J. Lankhaar, and B. Westerhof, "The arterial windkessel," *Medical & Biological Engineering*, vol. 47, no. 2, pp. 131–141, 2008.

[101] W. J. G., *Encyclopedia of Medical Devices and Instrumentation. Second Edition*. John Wiley & Sons, Inc., Hoboken, New Jersey, 2007.

[102] A. Bertram and R. Glüge, *Solid mechanics: Theory, modeling, and problems*. 2015.

[103] J. Vierendeels, K. Dumont, and P. Verdonck, "A partitioned strongly coupled fluid-structure interaction method to model heart valve dynamics," *Journal of Computational and Applied Mathematics*, vol. 215, no. 2, pp. 602–609, 2008.

[104] D. Carswell, D. McBride, T. Croft, A. Slone, M. Cross, and G. Foster, "A CFD model for the prediction of haemolysis in micro axial left ventricular assist devices," *Applied Mathematical Modelling*, vol. 37, no. 6, pp. 4199–4207, 2013.

[105] E. Gudino and A. Sequiera, "3D mathematical model for blood flow and non-Fickian mass transport by a coronary drug-eluting stent," *Applied Mathematical Modelling*, vol. 46, pp. 161–180, 2017.

[106] A. P. Y. Lakshmi P Dasi, Helene A Simon, Philippe Sucosky, "FLUID MECHANICS OF ARTIFICIAL HEART VALVES," *Clinical and Experimental Pharmacology and Physiology*, vol. 36, no. 2, pp. 225–237, 2009.

[107] A. M. Malek, S. L. Alper, and S. Izumo, "Hemodynamic shear stress and its role in atherosclerosis," *Journal of the American Medical Association*, vol. 282, no. 21, pp. 2035–2042, 1999.

[108] P. Assemat, J. Armitage, K. Siu, K. Contreras, A. Dart, J. Chin-Dusting, and K. Hourigan, "Three-dimensional numerical simulation of blood flow in mouse aortic arch around atherosclerotic plaques," *Applied Mathematical Modelling*, vol. 38, no. 17-18, pp. 4175–4185, 2014.

[109] M. D. De Tullio, J. Nam, G. Pascazio, E. Balaras, and R. Verzicco, "Computational prediction of mechanical hemolysis in aortic valved prostheses," *European Journal of Mechanics, B/Fluids*, vol. 35, pp. 47–53, 2012.

[110] "Source of the medical data from." `http://www.vascularmodel.com/`. Accessed: 2016-01-03.

[111] L. Rimmer, M. U. Ahmad, G. Chaplin, M. Joshi, and A. Harky, "Aortic Valve Repair: Where Are We Now?," *Heart Lung and Circulation*, vol. 28, no. 7, pp. 988–999, 2019.

[112] K. J. Grande, R. P. Cochran, P. G. Reinhall, and K. S. Kunzelma, "Stress variations in the human aortic root and valve: The role of anatomic asymmetry," *Annals of Biomedical Engineering*, vol. 26, no. 4, pp. 534–545, 1998.

[113] T. M, " The aortic valve," *Boca Raton, FL: CRC Press*, no. 1990, 1990.

[114] P. S. F. B. J. De Hart, G.W.M. Peters, "A three-dimensional computational analysis of fluid–structure interaction in the aortic valve," *Journal of Biomechanics*, vol. 36, no. 0, pp. 103–112, 2003.

[115] Y. G. Lai, K. B. Chandran, and J. Lemmon, "A numerical simulation of mechanical heart valve closure fluid dynamics," *Journal of Biomechanics*, vol. 35, no. 7, pp. 881–892, 2002.

[116] T. Kenner, "The measurement of blood density and its meaning," *Basic Research in Cardiology*, vol. 84, no. 2, pp. 111–124, 1989.

[117] V. W. T. F. B. P. Press Willam H., Teukolsky Saul A., *Numerical Recipes in C. The Art of Scientific Computing. Second edition*. 2002.

[118] U. Gülan and M. Holzner, "The influence of bileaflet prosthetic aortic valve orientation on the blood flow patterns in the ascending aorta," *Medical Engineering and Physics*, vol. 60, 2018.

[119] S. K. Kadhim, M. S. Nasif, H. H. Al-Kayiem, and R. Al-Waked, "Computational fluid dynamics simulation of blood flow profile and shear stresses in bileaflet mechanical heart valve by using monolithic approach," *Simulation*, vol. 94, no. 2, pp. 93–104, 2018.

[120] O. Bech-Hanssen, K. Caidahl, I. Wallentin, P. Ask, and B. Wranne, "Assessment of effective orifice area of prosthetic aortic valves with Doppler echocardiography: An in vivo and in vitro study," *Journal of Thoracic and Cardiovascular Surgery*, vol. 122, no. 2, pp. 287–295, 2001.

[121] M. L. Kala K. Fleming, Joseph G. Dugandzik, *Susceptibility of Distribution Systems to Negative Pressure Transients*. AwwaRF and American Water, 2006.

[122] K. Chandran, E. Dexter, S. Aluri, and W. Richenbacher, "Negative Pressure Transients with Mechanical Heart-Valve Closure :," *Annals of Biomedical Engineering*, vol. 26, pp. 546–556, 1998.

[123] H. Lee and Y. Taenaka, "Observation and quantification of cavitation on a mechanical heart valve with an electro-hydraulic total artificial heart," *The International Journal of Artificial Organs*, vol. 29, no. 3, pp. 303–307, 2006.

[124] A. P. Y. Krishnan B. Chandran, Stanley E. Rittgers, *Biofluid Mechanics: The Human Circulation, Second Edition*. CRC Press, 2012.

[125] H. Lee and Y. Taenaka, "Physical effects in red blood cell trauma," *J Am Inst Chem Engr*, vol. 15, no. 707, 1969.

[126] B. Melka, W. Adamczyk, M. Rojczyk, A. J. Nowak, A. Golda, and Z. Ostrowski, *Virtual Therapy Simulation for Patient with Coarctation of Aorta Using CFD Blood Flow Modelling*, pp. 153–160. Cham: Springer International Publishing, 2017.

[127] OpenCV library, "v. 4.5.1-dev," *online: https://opencv.org/releases*, 2021.

[128] Endress+Hauser, "Proline Promag H 100 PROFIBUS DP. Operating instructions,"

[129] "Vision research, inc.,"

[130] "National instruments, inc.,"

[131] D. Lemos, A. Nunes, J. Machado, C. Barros, C. Leão, F. Soares, and G. Minas, "Mechanical simulation model of the systemic circulation," *Measurement*, vol. 66, 2015.

[132] S. Rumian, G. Milewski, M. Kopacz, and S. Zamarlik, "The possibility of the hydrodynamic evaluation of bio-pumps with the use of a hybrid-digital model of the circulatory system," *Measurement*, vol. 80, 2016.

[133] M. Qasaimeh, K. Denolf, A. Khodamoradi, M. Blott, J. Lo, L. Halder, K. Vissers, J. Zambreno, and P. Jones, "Benchmarking vision kernels and neural network inference accelerators on embedded platforms," *Journal of Systems Architecture*, 2020.

[134] V. Janga, S. Kumar, and V. Kumar, "Advanced machine learning-based implementation patterns for computer vision and real-time multimedia applications," *Materials Today: Proceedings*, 2020.

[135] P. Kalli, A. Baksheev, K. Kornyakov, and V. Eruhimov, "Realtime computer vision with opencv: Mobile computer-vision technology will soon become as ubiquitous as touch interfaces.," *ACM Queue*, vol. 10, 2012.

[136] OpenCV documentation, "v. 4.5.1-dev," *online: https://docs.opencv.org/master/da/d22/tutorial_py_canny.html*, 2021.

[137] A. Ratsakou, A. Skarlatos, C. Reboud, and D. Lesselier, "Shape reconstruction of delamination defects using thermographic infrared signals based on an enhanced canny approach," *Infrared Physics Technology*, vol. 111, 2020.

[138] J. Canny, "A computational approach to edge detection," *IEEE Transactions on pattern analysis and machine intelligence*, vol. 8, 1986.

[139] O. Zienkiewicz and R. Taylor, *The finite element method. The Basis*, vol. 1. 2000.

[140] *ANSYS® v20.1, Discovery Spaceclaim. Displaying mass properties, ANSYS, Inc.*

[141] O. Neikov and N. Yefimov, "Handbook of non-ferrous metal powders (second edition)," *Technologies and Applications*, 2019.

[142] M. Nobili, U. Morbiduccib, R. Ponzinic, C. Gaudiod, A. Balduccid, M. Grigionid, F. Montevecchib, and A. Redaellia, "Numerical simulation of the dynamics of a bileaflet prosthetic heart valve using a fluid-structure interaction approach," *Journal of Biomechanics*, vol. 41, 2008.

[143] M. de Tullio, L. Afferrante, G. Demelio, G. Pascazio, and R. Verzicco *Journal of Biomechanics*.

[144] S. Annerel, S. Claessens, J. Degroote, P. Segers, and J. Vierendeels *Medical Engineering Physics*.

[145] C. Curgien, V. Deplano, and E. Bertrand *Medical Engineering Physics*.

[146] "Ingress of coolant event simulation with trace code with accuracy evaluation and coupled dakota uncertainty analysis," *Fusion Engineering and Design*, vol. 159, p. 111944, 2020.

[147] M. Nobili, U. Morbiducci, R. Ponzini, C. Del Gaudio, A. Balducci, M. Grigioni, F. Maria Montevecchi, and A. Redaelli, "Numerical simulation of the dynamics of a bileaflet prosthetic heart valve using a fluid–structure interaction approach," *Journal of Biomechanics*, vol. 41, no. 11, pp. 2539–2550, 2008.

[148] T. Schaller, M. Scharfschwerdt, K. Schubert, C. Prinz, U. Lembke, and H.-H. Sievers, "Aortic valve replacement in sheep with a novel trileaflet mechanical heart valve prosthesis without anticoagulation," *JTCVS Open*, vol. 7, pp. 76–88, 2021.

[149] A. Amindari, L. Saltik, K. Kirkkopru, M. Yacoub, and H. C. Yalcin, "Assessment of calcified aortic valve leaflet deformations and blood flow dynamics using fluid structure interaction modeling," *Informatics in Medicine Unlocked*, vol. 9, no. July, pp. 191–199, 2017.

[150] B. Su, L. Zhong, X.-K. Wang, J.-M. Zhang, R. S. Tan, J. C. Allen, S. K. Tan, S. Kim, and H. L. Leo, "Numerical simulation of patient-specific left ventricular model with both mitral and aortic valves by fsi approach," *Computer Methods and Programs in Biomedicine*, vol. 113, no. 2, pp. 474–482, 2014.

[151] B. Vogl, N. Niemi, L. Griffiths, M. Alkhouli, and H. Hatoum, "Impact of calcific aortic valve disease on valve mechanics," *Biomechanics and Modeling in Mechanobiology*, 2021.

[152] C. Fisher, J. Chen, and W. Merryman, "Calcific nodule morphogenesis by heart valve interstitial cells is strain dependent," *Biomechanics and Modeling in Mechanobiology*, 2012.

[153] S. Nobari, R. Mongrain, R. Leask, and Cartier, "The effect of aortic wall and aortic leaflet stiffening on coronary hemodynamic: a fluid–structure interaction study," *Med Biol Eng Comput*, no. 51, 2013.

[154] "Investigation on the effect of density ratio on the convergence behavior of partitioned method for fluid–structure interaction simulation," *Journal of Fluids and Structures*, vol. 96, p. 103050, 2020.

[155] P. Stradins, R. Lacis, I. Ozolanta, B. Purina, V. Ose, L. Feldmane, and V. Kasyanov, "Comparison of biomechanical and structural properties between human aortic and pulmonary valve," *European Journal of Cardio-Thoracic Surgery*, vol. 26, pp. 634–639, 09 2004.

[156] A. I. Hassaballah, M. A. Hassan, A. N. Mardi, and M. Hamdi, "An inverse finite element method for determining the tissue compressibility of human left ventricular wall during the cardiac cycle," *PLOS ONE*, vol. 8, 12 2013.

[157] Z. Fayad, V. Fuster, J. Fallon, T. Jayasundera, S. Worthley, G. Helft, J. Aguinaldo, J. Badimon, and S. Sharma, "Noninvasive in vivo human coronary artery lumen and wall imaging using black-blood magnetic resonance imaging," *Circulation*, no. 102, 2000.

[158] G. Nannini, A. Caimi, M. C. Palumbo, S. Saitta, L. N. Girardi, M. Gaudino, M. J. Roman, J. W. Weinsaft, and A. Redaelli, "Aortic hemodynamics assessment prior and after valve sparing reconstruction: A patient-specific 4d flow-based fsi model," *Computers in Biology and Medicine*, vol. 135, p. 104581, 2021.

[159] H. Suito, K. Takizawa, V. Q. H. Huynh, D. Sze, and T. Ueda, "FSI analysis of the blood flow and geometrical characteristics in the thoracic aorta," *Computational Mechanics*, vol. 54, Oct. 2014.

[160] J. G. B. et al., *Anatomy and Physiology*. Openstax, 2012.

[161] H. Hatoum and P. Lakshmi, "Spatiotemporal Complexity of the Aortic Sinus Vortex as a Function of Leaflet Calcification," *Annals of Biomedical Engineering*, vol. 47, no. 4, 2019.

[162] A. Mohamed, A. Arifi, and A. Omran, "The basics of echocardiography," *J Saudi Heart Assoc.*, no. 22, 2010.

[163] Python documentation, "v. 4.5.1-dev," *online: https://www.python.org/doc/*, 2022.

[164] M.-A. Clavel, J. Malouf, D. Messika-Zeitoun, P. A. Araoz, H. I. Michelena, and M. Enriquez-Sarano, "Aortic valve area calculation in aortic stenosis by ct and doppler echocardiography," *JACC: Cardiovascular Imaging*, vol. 8, no. 3, pp. 248–257, 2015.

[165] Y. Westermann, A. Geigenmüller, T. Elgeti, M. Wagner, S. Dushe, A. C. Borges, P. M. Dohmen, P. A. Hein, and A. Lembcke, "Planimetry of the aortic valve orifice area: Comparison of multislice spiral computed tomography and magnetic resonance imaging," *European Journal of Radiology*, vol. 77, no. 3, pp. 426–435, 2011.

[166] B. Franke, J. Brüning, P. Yevtushenko, H. Dreger, A. Brand, B. Juri, A. Unbehaun, J. Kempfert, S. Sündermann, A. Lembcke, N. Solowjowa, S. Kelle, V. Falk, T. Kuehne, L. Goubergrits, and M. Schafstedde, "Computed tomography-based assessment of transvalvular pressure gradient in aortic stenosis," *Front. Cardiovasc. Med.*, vol. 8, 2021.

[167] A. Amindari, L. Saltik, K. Kirkkopru, M. Yacoub, and H. C. Yalcin, "Assessment of calcified aortic valve leaflet deformations and blood flow dynamics using fluid structure interaction modeling," *Informatics in Medicine Unlocked*, vol. 9, no. July, pp. 191–199, 2017.

[168] M. Heil, A. L. Hazel, and J. Boyle, "Solvers for large-displacement fluid-structure interaction problems: Segregated versus monolithic approaches," *Computational Mechanics*, vol. 43, no. 1, pp. 91–101, 2008.

[169] D. D. Chandar, “On overset interpolation strategies and conservation on unstructured grids in OpenFOAM,” *Computer Physics Communications*, pp. 1–12, 2019.

Appendix A

Algorithm for the bileaflet mechanical valve data extraction

The presented Python source code allows to determine the bileatlet valve angular positions, both for the upper and the lower leaflet, from the large set of the fast camera images. User is supposed to set the proper center of rotations and the path to the folder containing images.

```
import cv2
import numpy as np
import math

def function():
    path_write = r'PATH\up' #in the code replace the "PATH"
    #with your image directory
    img = cv2.imread(path_read, 1)
    img_upper = img[50:250, 0:160]
    threshold = 50 # Here set the threshold for the upper leaflet
    imgcanny = cv2.Canny(img_upper, threshold, threshold + 50)
    kernel = np.ones((5, 5), np.uint8)
    imgdialation = cv2.dilate(imgcanny, kernel, iterations=1) #Dialation to
    #increase the boundaries of regions of foreground pixels
    path_write_1 = path_write + str(a) + ".bmp"
    cv2.imwrite(path_write_1, imgdialation)
    path_write = r'PATH\down'
    img = cv2.imread(path_read, 1)
    img_lower = img[250:440, 0:160]
    threshold = 25 # Here set the threshold for the lower leaflet
    imgcanny = cv2.Canny(img_lower, threshold, threshold + 25)
    kernel = np.ones((5, 5), np.uint8)
    imgdialation = cv2.dilate(imgcanny, kernel, iterations=1)
    path_write_1 = path_write + str(a) + ".bmp"
    cv2.imwrite(path_write_1, imgdialation)

path_beginning = r'PATH/Img'

for a in range(0,45000):#45000 images
    path_read = path_beginning + str(a).zfill(6) + ".bmp"
    function()


row=200
column=160


#empty text files
ff = open("PATH/list_upper.txt", "w+").close()
ff = open("PATH/list_lower.txt", "w+").close()


```

```
#Set here center of rotation coord.
x_sr_up=0 #row
y_sr_up=134 #column
x_sr_down=0 #row
y_sr_down=28 #column


krok = []
path_up = r'PATH\up'
path_down = r'PATH\down'
for step in range(0, 45000):
    path_up_1=path_up+str(step)+".bmp"
    img = cv2.imread(path_up_1, 1)
    g = 0
    for i in range(column - 1, 0, -1):
        for j in range(row - 1, 0, -1):
            k = img[j, i]
            if k[1] != 0:
                angle=(y_sr_up-j)/(i+130-x_sr_up) #+130 because center
                # of rotation is beyond the picture
                angle=math.degrees(math.atan(angle))
                angle = (("%.6f" % (angle)))
                ff = open("PATH/list_upper.txt", "a+")
                ff.write("file=␣%s␣" % (step))
                ff.write("column=␣%s␣" % (i))
                ff.write("row=␣%s␣" % (j))
                ff.write("angle_upper=␣%s␣" % (angle))
                ff.write("colour=␣%s\n" % (k))
                ff.close()
                g = 1
                break
        if g == 1:
            break
    path_down_1 = path_down + str(step) + ".bmp"
    img = cv2.imread(path_down_1, 1)
    g = 0
    for i in range(column - 1 - 45, 0, -1):
        for j in range(0, row - 1 - 10, 1):
            k = img[j, i]
            if k[1] != 0:
                angle = (y_sr_down - j) / (i + 90 - x_sr_down)
                angle = math.degrees(math.atan(angle))
                angle = (("%.6f" % (angle)))
                ff = open("PATH/list_lower.txt", "a+")
                ff.write("file=␣%s␣" % (step))
                ff.write("column=␣%s␣" % (i))
                ff.write("row=␣%s␣" % (j))
                ff.write("angle_lower=␣%s␣" % (angle))
                ff.write("colour=␣%s\n" % (k))
                ff.close()
                g = 1
                break
        if g == 1:
            break
```

Appendix B

Algorithm for the flexible valves data extraction

Attached Python source code allows to determine the elastic valve opening (vessel lumen), defined as the distance between the upper and lower leatlet's points that are closest to the valve centerline. User is supposed to set the proper coordinates dependent on the image resolution and set view, and to set the path to the folder containing images.

```
import cv2
import numpy as np
import os

#in the code replace the "PATH" with
#your image directory.
#set in solver the black-and-white images (edges only),
#or use the Canny and Dialation operations as
#in Appendix A.
open("PATH/results.txt", "w+").close()
open("PATH/list_of_pictures.txt", "w+").close()
rootdir = 'PATH'
for subdir, dirs, files in os.walk(rootdir):
    for file in files:
        a=os.path.join(subdir, file)
        f = open("PATH/list_of_pictures.txt", "a+")
        f.write("%s\n" % (a))
        f.close()

file1 = open(r"PATH/list_of_pictures.txt", "r")
picture = [line.strip() for line in file1.readlines()]
file1.close()
```

```
23
24 #coordinates dependent on the picture size and set view, they
25 #describe the possible position (from "start" to "stop") for which
26 #the upper (noted as 1) and lower (noted as 2) leaflet may appear
27 x1_start=385
28 x1_stop=980
29 y1_start=80
30 y1_stop=540 #1080:2
31 x2_start=x1_start
32 x2_stop=x1_stop
33 y2_start=y1_stop
34 y2_stop=1080-y1_start
35
36 results=[]
37 for z in range(1, np.size(picture), 1):
38     picture = cv2.imread(picture[z])
39     picture_part1 = picture[y1_start:y1_stop, x1_start:x1_stop]
40     coordinate_upper=0
41     coordinate_lower=0
42     height = picture_part1.shape[0]
43     length = picture_part1.shape[1]
44     for i in range(0+50, height, 1):
45         black = 0
46         for j in range(0, length, 1):
47             k = picture_part1[i, j]
48             if k[1] == 0:
49                 black = black + 1
50         if black == 0:
51             coordinate_upper = i + y1_start
52             break
53     picture_part2 = picture[y2_start:y2_stop, x2_start:x2_stop]
54     for i in range(height - 50, -1, -50):
55         black = 0
56         for j in range(0, length, 1):
57             k = picture_part2[i, j]
58             if k[1] == 0:
59                 black = black + 1
60         if black == 0:
61             coordinate_lower = i + y2_start
62             break
63     span_pix = coordinate_lower - coordinate_upper
64     span = span_pix * (17.3 / 1006) #17.3 mm corresponds
65     # to 1006 pixels
66     print("span:␣", span, "plik:␣", picture[z])
67     results.append(span)
68 np.savetxt("PATH/results.txt", results, fmt="%s")
```

Appendix C

Moving mesh

To account for mesh during the geometry update, the proper moving mesh model has to be applied. In ANSYS® Fluent, there are present: sliding mesh, dynamic mesh (smoothing, layering, remeshing) and overset mesh, each with the different applicability. In this research, the linearly-elastic solid mesh smoothing model, done only on the each leaflet vicinity (called component bodies) was coupled with the overset mesh technology, which acts after the component bodies deformed.

The overset coupling procedure consists of the subsequent operations: hole cutting, overlap minimization and donor search. During the hole cutting, the cells that are lying outside the flow region are marked as dead, so they are not included during the computations. The remained cells are identified as solve cells, where the interpolation is realized between the *donor cells* and the *receptor cells*. Then, overlap minimization is used to minimize the overlap between meshes, mainly by turning the solve cells into receptor cells and marking unnecessary receptors as dead cells. The components' bodies priority was applied here, to preserve the boundary layer in the leaflets' vicinity. When the donor search is performed, the domain connectivity is established by searching solve cells for each receptor. However, the orphan cells can be generated, which means that the receptor cells cannot find the donor cell. This may affect the computational stability and convergence, and can be caused by different reasons [95]. The most common is insufficient overlap or very different mesh resolutions. Furthermore, they can appear when the number of cells across the gap is not enough (below 4), which prevent the proper interpolation. In this research at least 8 cells were imposed

across the gap. Finally, they could be present when the motion in the single timestep significantly exceeds the cell height.

Described moving mesh coupling enabled many advantages described in the paper, however, preparing the proper meshes and moving mesh settings was very demanding. Firstly, the overset background mesh was prepared and the component meshes were tested with different refinements and splitting into blocks. Then, when the proper mesh connectivity was obtained, i.e. none of the orphan cells were present, it was necessary to check if they are also avoided during the body motion (deformation) and to check as well the dynamic mesh operation. It was possible only when the leaflets geometries were deforming.

The FSI calculations are very time-consuming. Verifying all the questions related to meshes via the coupling calculations will demand even over a dozen days for the each test. Thus, the fluent case for testing via mesh previewing was prepared, using the macro `define_grid_motion`. This macro defines the motion along the every axis, that can be prescribed to every node individually and can be also time-dependent. It is assigned to the boundary (wall) and the motion of the interior mesh is controlled by the build-in algorithm. It can be used both for 2D and 3D systems.

Using the macro before the FSI calculations allowed to:

- check, if the proper dynamic and overset mesh settings were applied
- ascertain, that the poor quality cells resulted from the dynamic mesh operation, or orphan cells from the overset mesh are not present during the leaflet motion
- observe the overall moving mesh operation
- check the quality of produced cells
- compare the moving mesh operation for the different pseudo-timestep size, i.e. for different deformation per single mesh update

More intense deformation was applied than expected valve motion, to make sure that mesh deterioration in coupling will be avoided. In ANSYS Mechanical, the fixed support condition is applied between the leaflets edges and the aortic root. Thus, the macro could not deform the nodes located in these edges. To fulfill this limitation,

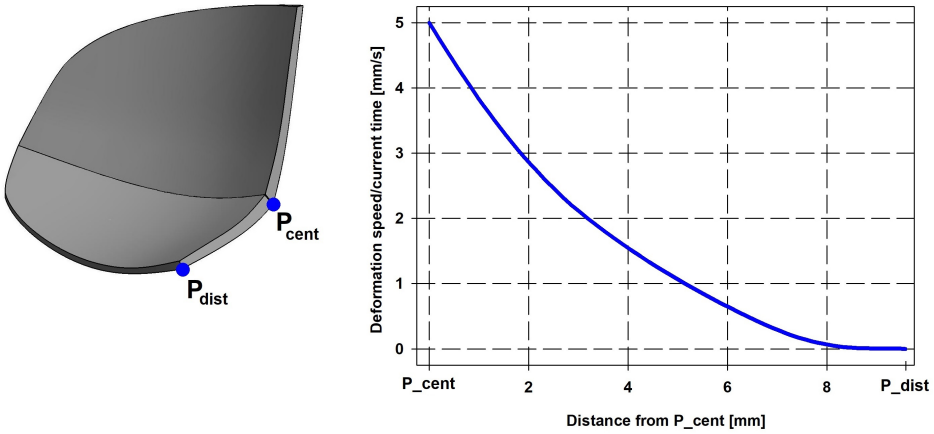

Figure C.1: Location of the points used for the macro source code (left) and deformation function prescribed to the leaflet walls (right)

the location of the central point $P_c(x_c, y_c, z_c)$ and the distal point $P_d(x_d, y_d, z_d)$ was determined -see Fig. C.1. Deforming operation was allowed only in the sphere with centre P_c and radius $R_{max} = |P_c P_d|$, which means:

$R_{max} = \sqrt{(x_c - x_d)^2 + (y_c - y_d)^2 + (z_c - z_d)^2}$.

The function noted in code as $move(dist)$ is the deformation function dependent on the mesh node distance to the central point. To create such function, the maximum speed of deformation was assumed in the central point (distance=0), equal 5 milimeters per second, and zero speed at nodes located in the maximum allowable distance. It was necessary to create the polynomial of fourth degree (Fig. C.1) to very slowly rise from the zero deformation region, in order to not deteriorate the geometry.

Below is the source code of prepared UDF for one of the leaflets. Two remaining UDFs differs only in the constants definition of the central and distal points coordinates. The created motion and mesh operation can be observed in Fig. C.2.

```
#include "udf.h"
#include "math.h"
#include "unsteady.h"

/*Define the location of the central (cent)*/
/*and distal (dist) point on the leaflet*/
/*between which deformation will take place*/
#define x_cent 0.015679
#define y_cent 0.00059509
#define z_cent -0.0003445
#define x_dist 0.01841
```

```
#define y_dist 0.0084328
#define z_dist 0.0044346

DEFINE_GRID_MOTION(grid_motion, domain, dt, time, dtime) /*Fluent UDF*/
{
face_t f;
Thread *tf = DT_THREAD(dt);
Node *v;
real x;
real y;
real z;
real dist_max;
real dist;
real move;

dist_max=sqrt(pow((x_cent-x_dist),2)+pow((y_cent-y_dist),2)+pow((z_cent-z_dist),2));

SET_DEFORMING_THREAD_FLAG(THREAD_T0(tf));
begin_f_loop(f, tf) /* loop over faces */
{
  f_node_loop(f, tf, n) /* loop over nodes */
  {
    v = F_NODE(f, tf, n);
    if (NODE_POS_NEED_UPDATE(v))
      {
      NODE_POS_UPDATED(v);
      x = NODE_X(v);
      y = NODE_Y(v);
      z = NODE_Z(v);
      dist=sqrt(pow((x-x_cent),2)+pow((y-y_cent),2)+pow((z-z_cent),2));
      if (dist<dist_max)
          {
move=CURRENT_TIME*(-1965.787*pow(dist,3)+91.963*pow(dist,2)-1.223*dist+0.005);
/*move is the deformation function */
/*dependent on the time and space */
      NODE_X(v)+=move;
          }
          }
  }
    Update_Face_Metrics(f, tf);
}
end_f_loop(f, tf);
}
```

Testing of many different meshes demanded much inconvenient work in the Fluent graphical interface. Thus, the journal file was created, which automatically: reads

newly created meshes, setup the whole overset interface, initialize case and display information about the orphan cells count:

```
; below, ov is the overset interface name
q q q def o-i delete ov q q q
; name.msh is the mesh file
; 13, 18, 23 is the overset zones IDs
file repl-me background.msh ok q q q
def bound-cond mod-zo append-mesh component1.msh q q q
def bound-con mod-zo zone-type 13 overset q q q
def bound-cond mod-zo append-mesh component2.msh q q q
def bound-con mod-zo zone-type 18 overset q q q
def bound-cond mod-zo append-mesh component3.msh q q q
def bound-con mod-zo zone-type 23 overset q q q
def o-i create ov background () component1 component2 component3 () no q q q
def o-i g-p ov 0 1 q q q
def o-i op d-p-m 1 q q q
; initialize the flow and check for the mesh connectivity
solve initialize ini-flow q q q
def o-i m-c orphan no q q q
```

Described procedure was used with different meshes, using above UDF and journal, until obtained meshes were not producing any low-quality or orphan cells – both with 1-leaflet and 3-leaflet moving configurations. During each test, it took only several minutes to set the overset case and preview the moving mesh operation.

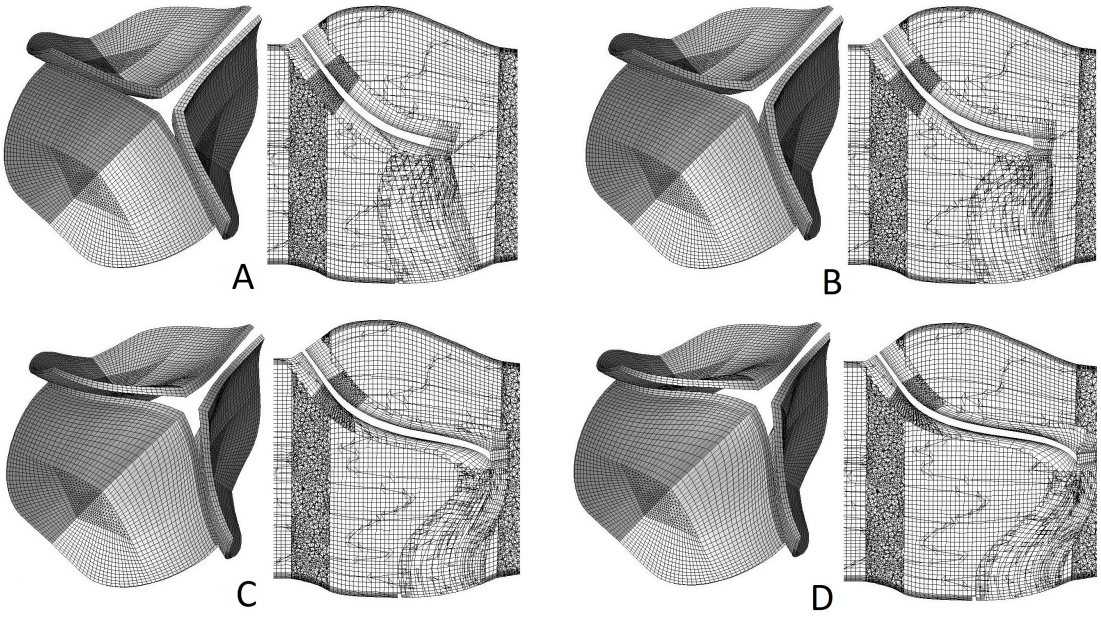

Figure C.2: Leaflet deformation and grid motion through cross-section, obtained for 3D model using applied testing procedure; **A** − starting orientation, **B**, **C** and **D** − 20., 40 and 50. pseudo-timestep, accordingly

Abstract

Development of numerical model for modeling artificial heart valves for performing virtual therapies

Keywords: aortic valve, hemodynamics, moving deforming mesh, fluid-structure interaction, CFD, coronary artery, blood flow, calcification, virtual therapy, test rig, computer vision

Aortic valve disease is one of the most common cardiovascular disease; they can be divided into congenital defects, such as biscupid aortic valve, or they appear as a disease with aging. The most common valvular disease is calcified aortic valve disease, reaching 13% in the general population over 65 years. For patients with advanced calcification stage, artificial aortic valve implantation is the only option, however this can lead to medical complications. There is a large potential in the development of a hybrid approach that combines fast echocardiography with an advanced numerical model.

In the Thesis different approaches for the modeling the movable, rigid and deformable structures, as human and artificial valves were used. Different moving mesh approaches were used and their results and validity were compared. The numerical results were compared with those obtained via measurements, performed using the inhouse test rig, also physiological data were used for such purpose. Laboratory test rig included the pulsatile blood pump, fast camera, mass flow meter, pressure transducers and valve holder designed for the measurements.

The mathematical model comprise the solving of the physics present on the fluid and the solid side, also the interaction between those two participants. The fluid equations included the partial-differential Navier-Stokes equations, turbulence model and Windkessel model for outflows, created based on the electrical analogy. Also, the non-Newtonian viscosity model had to be implemented into solution procedure. On the solid side, the structural governing equations were applied, which allowed to calculate the transient deformation fields. For the rigid bodies, the inhouse model was implemented into the fluid solver to determine their motion.

The synthetic valve operation was analyzed after its virtual implantation in the real patient vasculature geometry. The inhouse model for determining the transient angular leaflet motion was implemented. The inhouse algorithm was developed, to automatically determine the angular positions of the rigid-leaflet valves and valve opening of the elastic-leaflet valve, from the large set of the images. The two-way partitioned fluid-structure interaction model was applied for modeling of the elastic human valve. The novel, advanced moving mesh model was used. The impact of calcification process onto natural and artificial aortic valves was assessed and compared.

Abstrakt

Budowa modelu matematycznego na cel modelowania numerycznego sztucznych zastawek wykorzystywanego w wirtualnych zabiegach chirurgicznych

Słowa kluczowe: zastawka aortalna, hemodynamika, siatka ruchoma i odkształcalna, interakcja płyn-ciało stałe, numeryczna mechanika płynów, tętnica wieńcowa, przepływ krwi, zwapnienie, wirtualny zabieg chirurgiczny, walidacja modelu numerycznego, stanowisko testowe, widzenie komputerowe

Choroby zastawek są dominującą grupą wśród schorzeń układu krwionośnego. Mogą wystąpić jako choroby wrodzone lub pojawiają się wraz z wiekiem. Najczęstszą chorobą zastawki jest zwapnienie zastawki aortalnej, sięgające 13% populacji powyżej 65 roku życia. Dla pacjentów w zaawansowanym stadium, wszczepienie protezy jest jedynym rozwiązaniem, jednakże może to prowadzić do licznych komplikacji. Ogromny potencjał jest widziany w rozwoju podejścia łączącego echokardiografię z zaawansowanym modelem numerycznym. W pracy doktorskiej zastosowano różne podejścia do modelowania ruchomych, sztywnych lub odkształcalnych struktur, jak zastawka anatomiczna i sztuczna. Wykorzystano różne sposoby realizacji ruchomej siatki numerycznej. Wyniki modeli zwalidowano na stanowisku laboratoryjnym oraz przy użyciu danych fizjologicznych. Stanowisko laboratoryjne było wyposażone w pompę pulsacyjną, kamerę szybką, przepływomierz, przetworniki ciśnienia oraz specjalny stelaż zaprojektowany na cel pomiarów. Model matematyczny obejmował rozwiązanie fizyki obecnej po stronie płynu i ciała stałego, jak również wzajemną interakcję pomiędzy tymi stronami. Równania przepływowe zawierały równania różniczkowe cząstkowe Naviera-Stokesa, równania turbulencji i model Windkessela dla warunku brzegowego, stworzony na bazie analogii elektrycznej. Zaimplementowano również model cieczy nie-Newtonowskiej Carreau do procedury obliczeniowej. Po stronie ciała stałego, wykorzystano równania mechanicze, pozwalające na wyznaczenie zmiennych w czasie deformacji. Dla ciał nieodkształcalnych, zaimplementowano model własny wyznaczający ich ruch wskutek ruchu płynu. Praca sztucznej zastawki została przeanalizowana przy jej wirtualnym wszczepieniu do rzeczywistej geometrii naczyń pacjenta. Zaimplementowano model własny wyznaczający ruch sztucznej zastawki. Stworzono algorytmy do przetwarzania danych z kamery szybkiej, do wyznaczania kąta nachylenia płatów oraz stopnia otwarcia zastawki. Dwustronny model interakcji płyn-ciało stałe został wykorzystany do modelowania zastawki anatomicznej, z wykorzystaniem nowego sposobu realizacji siatki ruchomej. Zbadano wpływ procesu gromadzenia się blaszki miażdżycowej na pracę zastawki anatomicznej oraz sztucznej.